FATIGUE PERFORMANCE OF ELECTROLESS NICKEL COATINGS ON STAINLESS STEEL GAS TURBINE COMPRESSOR ROTORS

by

GARY ARTHUR NAPERT
LT, USCG

B.S., MATHEMATICAL SCIENCES
UNITED STATES COAST GUARD ACADEMY
(1978)

Submitted in Partial Fulfillment of the
Requirements for the Degree of

Master of Science
in
Aeronautics and Astronautics
at the
Massachusetts Institute of Technology
August 1989

Signature of Author_____
Department of Aeronautics and Astronautics
August 15, 1989

Certified by_____
Prof. Regis M. Pelloux
Professor, Department of Material Science and Engineering
Thesis Supervisor

Accepted by_____
Prof. Harold Y. Wachman
Chairman, Department Graduate Committee

1

Aero

FATIGUE PERFORMANCE OF ELECTROLESS NICKEL COATINGS ON STAINLESS STEEL GAS TURBINE COMPRESSOR ROTORS

by

GARY ARTHUR NAPERT
LT, USCG

Submitted to the Department of Aeronautics and Astronautics
on August 3, 1989 in partial fulfillment of the
requirements for the Degree of Master of Science in
Aeronautics and Astronautics

ABSTRACT

The excellent corrosion and wear protection afforded by electroless nickel coatings has found many applications in the aerospace industry. Conflicting reports concerning the fatigue performance of electroless nickel-phosphorus coatings have limited their development for dynamic machinery, including their use in aircraft gas turbine engines. The fatigue performance of three commercial electroless nickel-phosphorus coatings were evaluated on a high strength stainless steel substrate to determine the potential application of an electroless nickel coating on a gas turbine compressor rotor used in a U.S. Coast Guard helicopter engine. In addition, surface profile measurements were taken both before and after electroless nickel plating to determine the net change in surface roughness. A net reduction in surface roughness would show that electroless nickel coatings exhibit some leveling action (smoothening) which could improve the overall efficiency of the compressor rotor by reducing the size of the boundary layer.

The fatigue performance of the coatings was measured by comparing S-N diagrams generated through fatigue testing at room temperature. The fatigue strength of coated specimens was determined at 10^7 cycles at R=0, for coating thicknesses of 25 to 30 micrometers (1.0 mil). Cantilever flat sheet fatigue specimens were designed and processed to duplicate the manufacturing processes of the LYCOMING LTS 101-750-B2 axial compressor rotor. The mechanical properties; hardness, tensile strength and percent elongation of the patented Custom 450® stainless steel alloy were investigated. A comprehensive review of electroless nickel-phosphorus coatings is also presented.

The three electroless nickel coatings reduced the fatigue strength of the stainless steel alloy by 48 to 65 percent. The degradation in fatigue performance is caused by the low ductility (brittleness) of the coating, promoting crack initiation and accelerating the fatigue failure process. The differences in fatigue performance amongst the three coatings were attributed to differences in plating pretreatment and heat treatments. The high hardness values of electroless nickel coatings do not translate to high strength due to the presence of cracks and impurities in the coatings. Electroless nickel-phosphorus coatings can be used on dynamic machinery provided the stress levels experienced by the coating do not promote cracking. There is a trade-off: engineering design must limit coating tensile strain levels to take advantage of the excellent wear, erosion and corrosion protection provided by electroless nickel coatings. The three electroless nickel-phosphorus coatings did not reduce the surface roughness of the stainless steel substrate. Therefore, electroless nickel coatings do not provide any significant leveling action.

Thesis Supervisor: Dr. Regis M. Pelloux

Title: Professor of Materials Science and Engineering

Acknowledgement

This thesis is dedicated to the memory of:

Commander ERNEST J. WILLIAMS, United States Coast Guard

for his honesty, integrity, and sense of responsibility have left a lasting impression on my life. His friendship and fatherly advise are surely missed.

I would like to thank:

My darling wife, Deborah, for her patience, understanding and continued support.

My brother, Irving R. Napert, for his thoughtfulness and generosity.

Professor Pelloux for his recommendations and time.

2Lt Philip A. DiMascio, U.S. Army, for the detailed graphics and for the information used in section 2.4.1 presented in this paper.

Mark Buonanno for the instruction he provided in various metallurgical tests.

and last, but far from least

The **United States Coast Guard** for the opportunity to attend M.I.T.

Table of Contents

List of Figures

List of Tables

1. INTRODUCTION

1.1 Problem Statement

The objective of this research work is to determine the variability in the fatigue life and surface roughness of a compressor rotor plated with electroless nickel. The research was funded by the United States Coast Guard, in an effort to improve the efficiency and service life of the AVCO LYCOMING LTS 101-750B-2 turboshaft engine. The AVCO LYCOMING turboshaft engine is the main powerplant used on the USCG twin engine HH-65A helicopter. The USCG's interests are focused on the engine first stage axial compressor rotor, which has suffered considerable erosion and corrosion damage from operating in a saltwater environment.

Electroless nickel coatings have been proposed to minimize the damage caused by erosion and corrosion on aircraft gas turbine engines. They are chemically deposited age hardenable coatings used to protect exposed surfaces of materials. They can be applied on almost any surface with proper preparation. Electroless nickel coatings rival electrodeposited cadmium coatings for wear and corrosion resistance. The major drawback for implementation of electroless nickel coatings is the potential degradation in fatigue life of the base metal. Reductions in fatigue strength limits of up to 50% have been reported.

Research work has been published on the fatigue performance of mild steels coated with electroless nickel, but limited information is available on the fatigue performance of tough, high strength, low carbon stainless steels coated with electroless nickel. This research has explored the use of several commercially available electroless nickel plating techniques on a particular high strength stainless steel used to manufacture the LTS 101-750B-2 axial compressor rotor.

1.2 Methodology

The operating environment of the LTS 101-750B-2 axial compressor rotor is complex. The rotor is subjected to stresses due to startup, acceleration, deceleration, vibration, and compressor stalls. Additional changes in stress levels are imposed by the environment and stress concentrations due to geometry, cracks, inclusions and/or voids in the material. Thermally induced stresses are also present due to temperature gradients.

The stresses experienced by the rotor vary and cannot be modeled solely as low or high cycle fatigue problems. Service experience has indicated that operating stress levels have not resulted in catastrophic failures. Therefore to simplify the problem at hand, constant displacement fatigue tests were conducted to compare the fatigue performance of three different electroless nickel coatings against a baseline of uncoated fatigue bending specimens. A cantilever flat sheet fatigue specimen was designed. Seventy-two representative fatigue test specimens were machined from stainless steel sheet material identical in composition to the actual compressor rotor. The compressor rotor is a precipitation hardened investment casting. Again to improve the correlation of empirical data, the fatigue test specimens were annealed and aged in a similar fashion as the axial compressor rotor. Hardness tests were conducted to meet manufacturer's specifications and to insure consistency in the test specimens.

The test specimens were carefully cleaned and engraved. Fifty-seven test specimens were sent out to be commercially plated. Fifteen test specimens were mailed to Teledyne Neosho to obtain an 8-10% phosphorus electroless nickel coating with a one hour heat treatment of 274°C (525°F). The other forty-two test specimens were mailed to Enthone Incorporated to obtain three different coatings in groups of fourteen: (1) a low phosphorus 1-3% phosphorus electroless nickel coating with a four hour heat treatment at 191°C (375°F), (2) a low phosphorus 1-3% phosphorus electroless nickel coating with a four hour heat treatment at 191°C (375°F) followed by a one hour heat treatment at 366°C (690°F), and (3) a high phosphorus 10-12% phosphorus electroless nickel coating with a four hour heat treatment of 191°C (375°F).

11

Testing was conducted to specimen failure on two constant displacement fatigue bending machines using a stress ratio of R=0 at room temperature. Cycles to failure were measured by a mechanical counter attached to the motor. Stress levels were calculated as a function of beam displacement and specimen thickness. The data points obtained by varying displacement (stress level) provided traditional S-N diagrams to evaluate the performance of each coating.

A surface profilometer was used to obtain surface roughness measurements of fatigue specimens before and after plating for each type of electroless nickel-phosphorus coating. A comparison of the measurements was done to determine the leveling effect (change in surface roughness) of each of the coatings.

Tensile tests were conducted on uncoated tensile specimens at different heat treatments to measure the modulus of elasticity, ultimate tensile strength, 0.2% offset yield strength and percent elongation.

2. BACKGROUND AND LITERATURE REVIEW

2.1 LTS-101-750B-2 Axial Compressor Rotor

The U. S. Coast Guard's HH-65A helicopter is an all weather, twin engine, short range rescue helicopter (**figure 2-1** on page 13). It flies with a crew of three: pilot, copilot and hoist operator. It has a maximum gross weight of 4045 Kg (8900 lbs). It's propulsion is provided by two LYCOMING LTS-101-750B-2 engines, each providing 507 Kilowatts (680 horsepower) at standard day conditions for normal takeoff. In addition, each engine is capable of providing 548 Kilowatts (735 horsepower) for emergency single engine operation.[1]
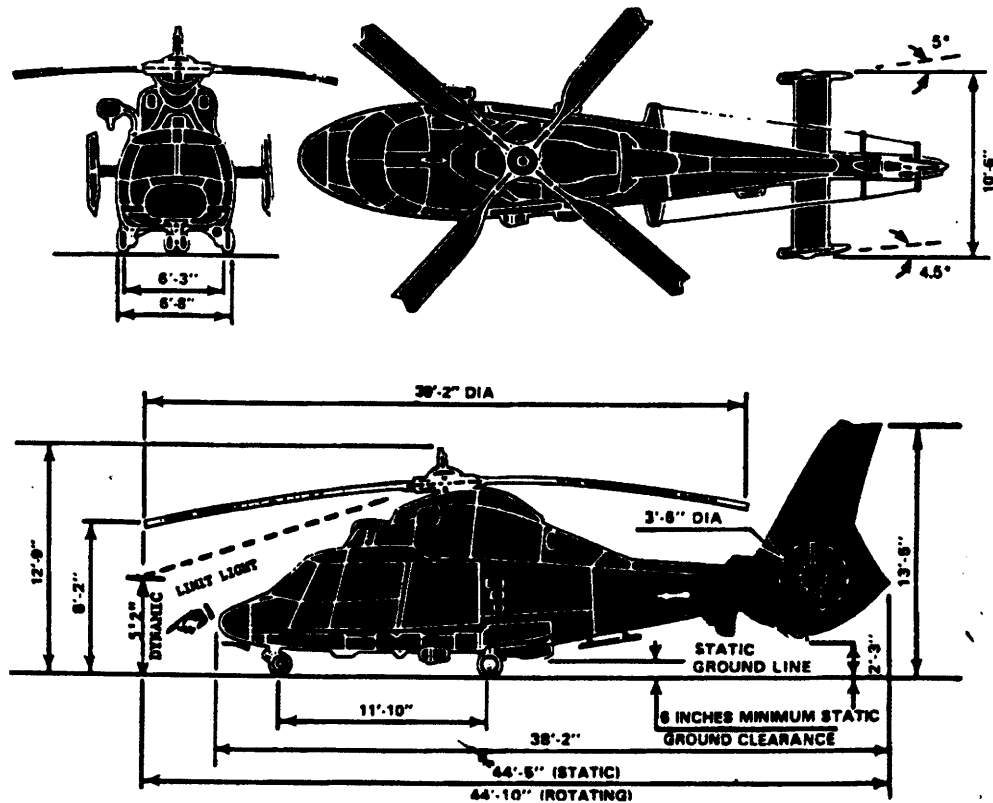
Figure 2-1. USCG HH-65A helicopter [2]

The LTS-101-750B-2 engine is comprised of the following modules: accessory/reduction gearbox, radial inlet, gas generator and combustion free power turbine.

Air Diffuser
Gas Generator Nozzle
Combustor Section
Gas Generator Rotor
Power Turbine Wheel
Radial Inlet Screen
Fuel Filter
Fuel Pump
Fuel Control
Power Turbine Nozzle
Ignitor Plug
Centrifugal Compressor Rotor
Axial Compressor Rotor
Oil Pump And Filter Assembly
Power Turbine Govenor
Anticipator
Power Outlet
Ignitor Box
Accessory Reduction Gear Box
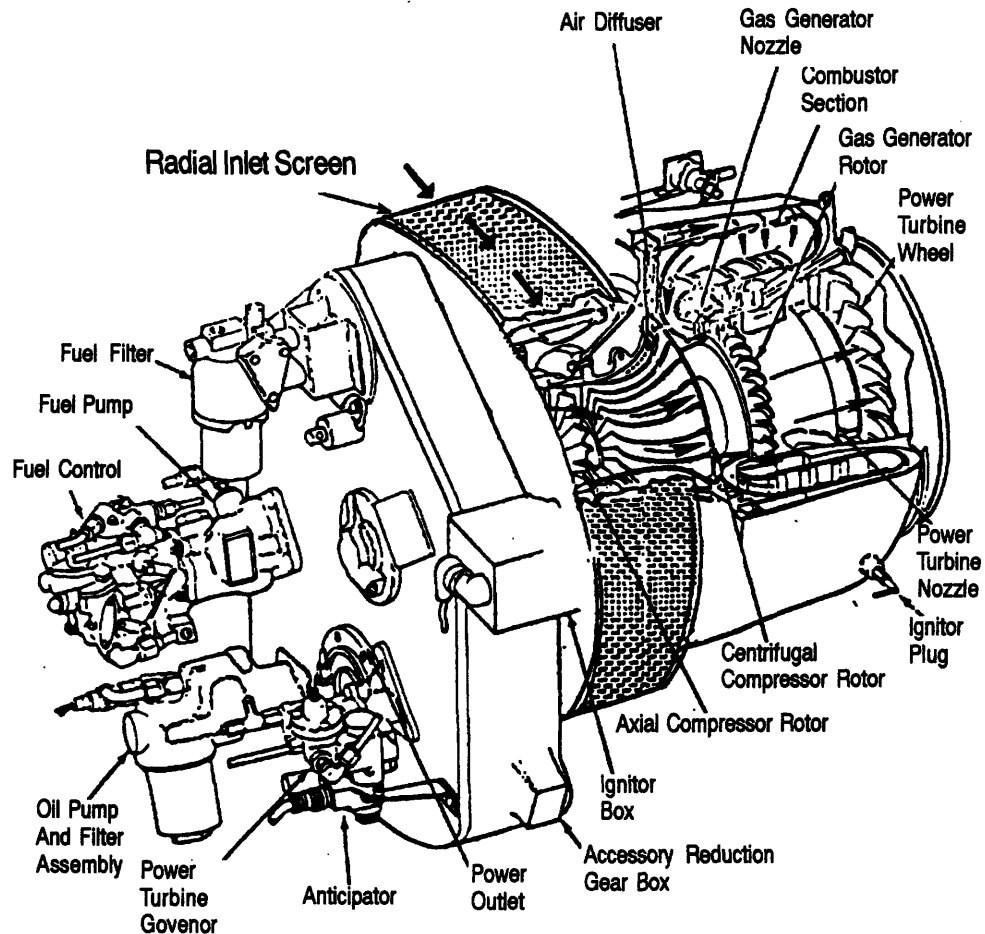
Figure 2-2. LYCOMING LTS 101-750B-2 Engine[3]

During engine operation, air passes through the air inlet ducts on the sides of the helicopter. It is directed through the radial inlet screen to the compressor inlet. The compressor, part of the gas generator, is comprised of a single stage axial compressor and a centrifugal compressor. The single stage axial compressor is the focus of this research work.

The speed of rotation of the gas generator is referred to as Ng, and is measured as a percentage of engine design operating speed (rpm). At a normal engine operating speed setting of 100% Ng, the compressor rotor is turning at the design speed of 47,870 rpm or about 800 hertz. The actual size of the axial compressor rotor is 14.0 centimeters in diameter and its shape is illustrated in **figure 2-3**.
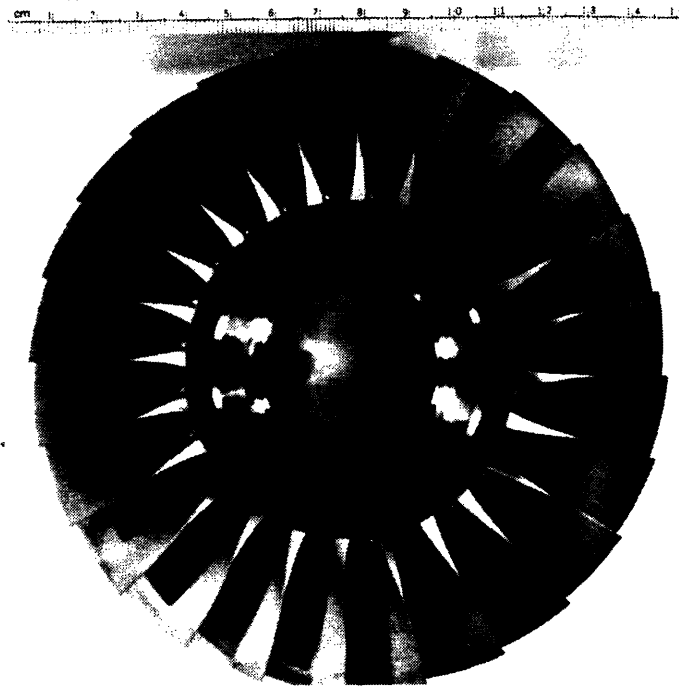
Figure 2-3. LTS 101-750B-2 Axial Compressor Rotor

The most significant stresses experienced by the rotor are those caused by the rotational forces and the gas bending loads. The high speed rotation of the rotor causes centrifugal stresses in the radial direction. The gas dynamic forces about the rotor blade cause stresses principally in the axial and tangential directions. The centrifugal stresses can be determined by rotor geometry and speed of rotation (equations 2.1-1 & 2.1-2). The stresses associated with the gas bending loads are more difficult to determine, requiring detailed design analysis. In general, the gas bending stresses are much less than the centrifugal stresses. If the

15

gas bending loads are ignored to simplify the stress analysis of the rotor, the centrifugal stresses can be used to approximate the stress levels experienced in the rotor. An approximation for the centrifugal stresses can be made by the following equations[4]:

(equation 2.1-1):

$$\sigma = \frac{\rho\,\omega^2\,r_H^2 + \left(\dfrac{B}{2\,\pi}\right)\sigma_b\left(\dfrac{A_b}{W_o\,T_o}\right)}{1 + \left(\dfrac{z_H\,r_H}{W_o\,T_o}\right)}$$

(equation 2.1-2):

$$\sigma_b = \left(\frac{\rho\omega^2 r_T^2}{2}\right)\left[1 - \left(\frac{r_H}{r_T}\right)^2\right]$$

Given the physical dimensions of the rotor to be as follows:

σ_b= Rotor blade stress at blade root, computed to be 361 MPa (52 ksi) for normal operations and 707 MPa (103 ksi) for burst speed containment (equation 2.1-2).

σ = Rotor disc stress, computed for normal operation and burst speed factor of 1.4: 88 MPa (12.8 ksi) normal oprations and 172 MPa (25 ksi) for burst speed containment (equation 2.1-1).

ω = Angular velocity, equal to $2\pi n$, where n is in cycles per second (Hz). n = 800 Hz for normal operation and 1120 Hz for burst speed containment.

ρ = Density of rotor disc and blades.(Custom 450®) specific gravity of stainless steel is equal to 7.765, density of water is 1000 kg/m3, therefore, ρ = 7765 kg/m3.

r_H = Rotor hub radius, equal to 35.0 mm or 0.035 meters.

r_T = Rotor tip radius, equal to 70.0 mm or 0.070 meters.

A_b= Blade root area (estimated to be equal to thickness of blade x rotor blade chord length at tip), equal to 24.6 x 10-6 square meters.

W_0= Rotor disc outer hub width, equal to 19.8 mm or 0.0198 meters.

T_0= Rotor disc outer hub height, equal to 5.3 mm or 0.0053 meters.

B = Number of blades, equal to 24.

z_H= Rotor disc outer hub support width, equal to 16.2 mm or 0.0162 meters.

During normal operations, the compressor rotor experiences the maximum centrifugal stress at the blade root, approximately 361 MPa (52 ksi). Generally, compressor and turbine rotating parts are designed to withstand overspeeds of between 1.3 to 1.4 times their design operating speed[3]. This overspeed is referred to as the "burst speed". The ultimate strength of the blade or disc material must be able to withstand the centrifugal stresses of these speeds to prevent disintegration of the rotor. Using a burst speed factor of 1.4, results in blade root stresses of approximately 707 MPa (103 ksi).

2.2 Base Metal - Custom 450® Stainless Steel

The axial compressor rotor of the LYCOMING LTS 101-750B-2 turboshaft engine is a precipitation hardened stainless steel investment casting. The stainless steel used for the casting is a patented alloy made by the Carpenter Technology Corporation, Carpenter Steel Division of Reading, Pennsylvania. The U.S. Patent No. is 3,574,601 and trademark or company designation is Custom 450®. The composition of Custom 450® is listed in **table 2-1** on page 18[6].

Table 2-1: Composition of Custom 450® Stainless Steel

Element	Weight percent
Carbon	0.05% maximum
Manganese	1.00% maximum
Silicon	1.00% maximum
Phosphorus	0.03% maximum
Sulphur	0.03% maximum
Chromium	14.00-16.00%
Nickel	5.00-7.00%
Molybdenum	0.50-1.00%
Copper	1.25-1.75%
Columbium	8 x carbon minimum
Iron	remainder

The manufacturer states, "Custom 450® is a martensitic age-hardenable stainless steel which exhibits very good corrosion resistance (similar to type 304 stainless steel) with moderate strength (similar to type 410 stainless steel). The alloy has a yield strength somewhat greater than 689 MPa (100 ksi) in the annealed condition, but is easily fabricated. A single-step aging treatment develops higher strength with good ductility and toughness."[5] As with all precipitation hardened stainless steels, the mechanical properties will depend on aging time and temperature. The aging procedure used to fabricate the compressor rotor was determined to be the procedure which would result in the optimum tensile and yield strengths for the alloy. This procedure is specified by Carpenter Technologies Corporation to be as follows[7]:

(1) Anneal - heat to 1024-1052°C (1875-1925°F), hold for one hour at temperature and cool rapidly. Water or oil quenching preferred for optimum aging response, but air quenching is suitable for thin sections.

(2) Aging - heat to 482-566°C (900-1050°F) for four hours followed by air cooling. The 482°C (900°F) temperature age produces the optimum combination of strength, ductility and toughness. Overaging increases the ductility and decreases strength.

The physical properties of Custom 450®, provided by the manufacturer, are listed in table 2-2[8].

Table 2-2: Physical Properties of Custom 450® Stainless Steel

property	annealed	aged 482°C (900°F)
Specific gravity	7.75	7.76
Density	7750 kg/m^3	7760 kg/m^3
Ultimate Tensile Strength	979 MPa 142 ksi	1351 MPa 196 ksi
0.2% Yield Strength	814 MPa 118 ksi	1296 MPa 188 ksi
Modulus of Elasticity (E)	193 x 10^3 MPa 28 x 10^3 ksi	200 x 10^3 MPa 29 x 10^3 ksi
Ductility, Percent Elongation	13 %	14 %
Poisson's Ratio	0.29	0.29
Mean Coefficient of Thermal Expansion (24°C to 93°C)	10.58 (10^{-6}/°K) 5.88 (10^{-6}/°F)	10.80 (10^{-6}/°K) 6.00 (10^{-6}/°F)

2.3 Electroless Nickel Coatings • Literature Review

Chemically reduced nickel, commonly known as "electroless" nickel has been used as a coating to rebuild worn machinery and improve solderability, brazability, wear resistance and corrosion resistance. Its application has spread to the aerospace industry, where it is used extensively as a protective coating for aluminum. Aircraft engine manufacturers, airlines and overhaul facilities are currently using electroless nickel coatings on compressor stator vanes and spacers, tubing connectors, fuel control cam assemblies and bearing supports for erosion,

corrosion and fretting wear protection[9]. Additional applications have included: landing gear, brake and flap control parts for the DC-9 and Boeing 727 and DC-9 brake attach bolts and anti-rotation plates[10]. The advantages of electroless nickel are its high hardness, high wear resistance, low porosity, and uniform deposition (high throwing capability). It can be used to pre-coat surfaces for subsequent electroplating, providing a pore-free undercoat which seals and protects the substrate. Electroless nickel coating thicknesses can be controlled to tolerances of 0.25 - 2.0 micrometers (0.01-1 mil)[11]. Plating can be prevented where needed with the use of a *maskant*. The maskant seals the surface of the substrate, acting as a barrier in prohibiting the chemical reactions from taking place on the surface.

The disadvantages of electroless nickel plating are: high chemical costs (3 to 5 times more expensive than electroplating), slower plating rates than electrodeposited nickel, unstable plating bath solutions, brittleness of the coating and the poor welding characteristics of the nickel-phosphorus coating. An additional limitation is the requirement to pre-coat substrates containing significant amounts of lead, tin, cadmium, or zinc. This is done by the use of a strike copper plate[12]. Thus, with proper preparation, any material can be plated.

The use of electroless nickel coatings on gas turbine compressor rotors has not met general acceptance due to the unfavorable effects it has demonstrated on fatigue life. Fatigue tests of electroless nickel on steel substrates conducted in the U.S.S.R., Japan, and the United States have provided inconclusive results. The fatigue tests focused on the influence of the following factors: phosphorus content, heat treatment, residual stresses, stress concentrations, plating bath composition and pH. The fatigue tests were conducted on several grades of steel, isolating several of the different factors in each test.

Electroless nickel coatings were discovered by A. Brenner and G. Riddell in 1944. Since this time, electroless nickel coatings have received significant commercial development due to several of its advantages over electrodeposited nickel; better corrosion and wear resistance and superior coating uniformity. Electroless nickel differs from electrodeposited nickel in that no electrical current source is required to reduce the nickel ions from solution onto the base metal.

Under the proper conditions, the chemical reactions are self-sustaining or autocatalytic. There are four different kinds of electroless nickel coatings, each produced by a particular plating bath solution. The reducing agent used in the plating bath identifies the type of electroless nickel produced. The reducing agent sodium hypophosphite is used to produce an electroless nickel-phosphorus coating. Sodium borohydride or aminoborane are reducing agents used to produce electroless nickel-boron coatings. The reducing agent hydrazine produces a 97 to 99 percent nickel coating. The hydrazine reduced electroless nickel coating is brittle, highly stressed, and provides poor corrosion resistance[13]. Typically, two nickel alloys, nickel-phosphorus and nickel-boron are produced through common plating techniques for engineering applications. Nickel-phosphorus coatings have received the most attention because the nickel-boron coatings are more expensive, porous, provide inferior corrosion protection and contain high tensile residual stresses on the surface. These surface tensile stresses are detrimental to the fatigue life of the base metal. The nickel-phosphorus coatings are the focus of this investigation.

2.3.1   Electroless Nickel-Phosphorus Plating

The electroless nickel plating process is described as a controlled chemical reduction of nickel ions from solution onto a catalytic surface. Remarkably, the plated surface continues to act as a catalyst to the chemical reduction and the reactions continue as long as the surface remains in contact with the plating solution. In contrast with electrodeposited nickel, no electric current is applied. This results in a coating of uniform thickness on all areas of an article in contact with fresh solution[14]. It is important to note the importance of solution agitation in promoting an equilibrium in both solution composition and temperature. Proper agitation ensures an adequate concentration of reactants and provides their transport to all surfaces of the article to be plated.

Electroless nickel plating solutions are composed of different chemicals, each providing an important function. The constituents of an electroless nickel solution and their function are as follows[15,16] :

(1) A nickel salt to supply the nickel, usually nickel sulfate.

(2) A hypophosphite salt to serve as the reducing agent in providing a supply of electrons for the reduction of nickel.

(3) Energy or heat to drive the reactions.

(4) Complexing agents (chelators) to control the availability of free nickel in the chemical reaction.

(5) Buffering agents to control the pH of the solution caused by the hydrogen released during deposition.

(6) Accelerators (exultants) to help increase the speed of the chemical reaction.

(7) Inhibitors (stabilizers) to help control the reduction and prevent spontaneous decomposition of the bath.

(8) Water to act as the transport medium.

(9) Reaction by-products.

(10) A catalytic surface to be plated.

The proportions and compositions of these components determine not only the electroless nickel bath but also the characteristics of the deposit.

The reducing agent used to plate out an electroless nickel-phosphorus coating is sodium hypophosphite. It is the most prevalent reducing agent used for commercial applications of electroless nickel due to the lower cost, greater ease of control and better corrosion resistance of the deposit. The mechanisms for the chemical reactions which take place in hypophosphite reduced solutions are still not completely clear. The most widely accepted mechanisms are as follows[17]:

$$\text{(equation 2.3.1-1)} \quad (H_2PO_2)^- + H_2O \xrightarrow[\text{heat}]{\text{catalyst}} H^+ + (HPO_3)^- + 2H_{abs}$$

$$\text{(equation 2.3.1-2)} \quad Ni^{++} + 2H_{abs} \xrightarrow{\quad\quad} Ni + 2H^+$$

$$\text{(equation 2.3.1-3)} \quad (H_2PO_2)^- + H_{abs} \xrightarrow{\quad\quad} H_2O + OH^- + P$$

$$\text{(equation 2.3.1-4)} \quad (H_2PO_2)^- + H_2O \xrightarrow{\quad\quad} H^+ + (HPO_3)^- + H_2$$
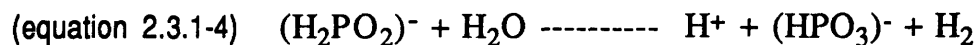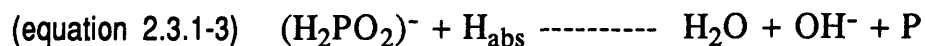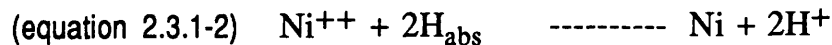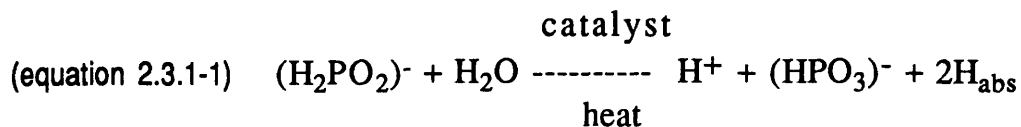
- In solution with a catalytic surface at the proper temperature (usually 95°C), hypophosphite ions are oxidized to orthophosphite (equation 2.3.1-1). Some of the hydrogen evolved is absorbed onto the catalytic surface.

The absorbed active hydrogen reduces the nickel at the surface (equation 2.3.1-2). At the same time, some of the absorbed hydrogen reduces a small portion of the hypophosphite to water, the hydroxyl ion and phosphorus (equation 2.3.1-3).

Unfortunately, most of the hypophosphite in solution is catalytically oxidized to orthophosphite and hydrogen gas (equation 2.3.1-4)[18,19]. This reaction occurs independent of the reduction of nickel and phosphorus at the surface. The hydrogen gas evolved during the plating process accounts for the inefficiency of the reducing agent. The reduction efficiency of hypophosphite is also a function of the substrate surface area to plating solution volume ratio, A/V. The efficiency of hypophosphite can vary from 20 to 40 percent. When the bath loading (A/V) is in the range of 74 to 172 square centimeters per liter (0.30 to 0.70 sq ft per gallon), about 5 kg (11 lb) of sodium hypophosphite are required to reduce 1 kg (2.2 lb) of nickel, an average efficiency of 37%[20].

Proper operation of the plating bath is a complex and delicate task. Several factors will be analyzed in order to understand the structure of the deposit and sensitivity of the bath. The reaction by-products and temperature play an important role in the plating process.

During plating, the concentration of orthophosphite $(HPO_3)^-$ increases resulting in a nominal decrease in the plating rate and a small increase in the phosphorus content of the deposit. The increased orthophosphite concentration eventually leads to the precipitation of nickel phosphite. This precipitate in the bath will cause rough deposits and eventually lead to bath decomposition. Complexing agents such as citric, glycolic or lactic acid are used to increase the orthophosphite tolerance of the bath[21].

The plating process also reduces the pH. Hydrogen ions produced by the reactions will continue to lower the pH until nickel deposition virtually stops at a pH below 4. There are two reasons to keep the pH in a narrow range: (1) to maintain plating rate and (2) to provide a uniform deposit composition, since the phosphorus content of the nickel deposit will increase with decreasing pH. Buffers such as acetate, propionate, and succinate are used to resist changes in pH. Sometimes alkaline materials are used to neutralize the acid formed during plating[22]. Early electroless nickel plating solutions operated at a high pH because they contained ammonia. After further development, acid solutions were found to have distinct advantages such as higher plating rates, better stability, greater ease of control and improved deposit corrosion resistance. As a result, most hypophosphite reduced solutions are operated between 4 and 5.5 pH[23].

Temperature is one of the most important factors affecting the deposition rate. The rate of deposition in hypophosphite reduced baths, operating in the pH range of 4 to 5, is an exponential function of temperature. Typically, deposition rates are very low at temperatures below 65°C (150°F), less than 7 micrometers per hour, but increase rapidly with increased temperature to rates of more than 25 micrometers per hour at 93°C (200°F). The preferred operating temperature range is 87-93°C (190-200°F). Plating bath design and operation must prevent local overheating at these temperatures to avoid bath decomposition[24].

There are hundreds of patented electroless nickel processes. However, the various electroless nickel plating processes function the same regardless of the substrate to be plated. The preparation of the substrate's surface may differ from one material to another, in order to provide a clean catalytic surface for good adhesion. Stainless steel preparation or pretreatment

24

consists of degreasing, acid activation, electrocleaning and a low pH nickel strike. The nickel

strike (thin electrodeposited film) is necessary to provide the catalytic surface for the initial

replacement reaction (equation 2.3.1-2) to take place. The two most common strike baths are

the nickel sulfamate and Woods nickel strikes. Proper pretreatment is as important as the

electroless plating bath in providing a defect-free coating. In essence, the pretreatment is

considered to be an important and critical step in the electroless nickel plating process.

2.3.2   Physical Properties of the Nickel-phosphorus Coatings

Electroless nickel-phosphorus coatings are described as either "very fine polycrystaline

supersaturated solid solutions or amorphorus metastable alloys"[25]. The initial "as-plated"

deposit is amorphous (glass-like) with a lamellated columnar structure. The lamellae (bands) are

parallel to the base metal. Heat treatment of the "as-plated" deposit transforms it into a

dispersion of nickel phosphite (Ni_3P) in a nickel matrix [26]. As nickel-phosphorus deposits are

heated to temperatures above 220°C (430°F), crystalline nickel phosphide particles precipitate,

increasing the hardness of the deposit. A decrease in hardness is observed when the deposit is

heated above 400°C (750°F) for an extended time due to gradual crystal growth. If a deposit

plated on steel is heated to temperatures above 537°C (1000°F) the nickel deposit and substrate

form a diffusion zone. The nickel diffuses into the steel substrate and the iron into the nickel

coating. The diffusion zone thickens slowly with time. At the same time the phosphorus migrates

to the surface and reacts with the oxygen to form P_2O_5. During crystallization the volume of

the deposit decreases. This shrinkage is responsible for the microcracks or fissures often found

in the deposit after heat treatment at 400°C (750°F)[27].

The physical properties of electroless nickel-phosphorus coatings are dependent on the

phosphorus content and heat treatment of the coating. The phosphorus content is reported as a

percentage of weight with values ranging from 2 to 14 percent. The phosphorus content of the

coating is also a function of the operating bath's pH, where phosphorus content increases as the

bath pH decreases. The lamellated columnar structure is believed to be the result of this phenomena. Continuity throughout the deposit is also dependent upon composition. Coatings with more than ten percent phosphorus and less than 5 percent impurities are generally continuous. Coatings with low phosphorus are more porous than high phosphorus content coatings. The increased porosity reduces the ductility and corrosion resistance of the low phosphorus coatings[28].

The purpose for using a coating on the compressor rotor is to provide corrosion and erosion protection. Therefore, important mechanical properties for discussion are hardness, wear resistance and corrosion resistance.

2.3.2.1   Density

The density of electroless nickel-phosphorus is inversely proportional to the phosphorus content, ranging from about 8.5 grams per cubic centimeter for low phosphorus deposits to 7.75 grams per cubic centimeter for deposits with 10 to 11 percent phosphorus [29].

2.3.2.2   Strength and Ductility

Generally, electroless nickel deposits are strong and brittle. The modulus of elasticity for a 7 to 11% phosphorus coating is about 200 GPa (29×10^6 psi), similar to steel. The ultimate tensile strength of commercial quality coatings exceeds 700 MPa (102×10^3 psi). Their strength and ductility is strongly influenced by the phosphorus content of the alloy. The relationship between phosphorus content and strength and strain at fracture is depicted in **figure 2-4** on page 27[30].
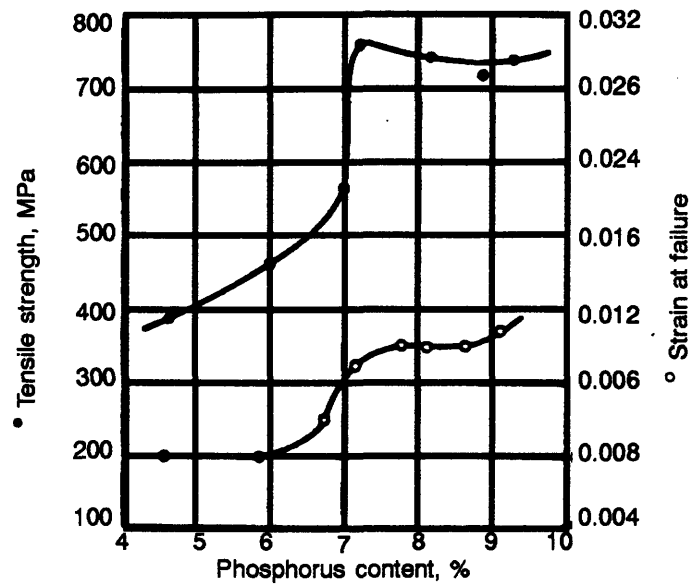
Figure 2-4. Effect of Phosphorus Content on Strength and Strain at Fracture (from Metals Handbook, Vol. 5, p. 226).

The high phosphorus, high purity coatings have a percent elongation between 1 and $1^1/_2$ percent at fracture. Low phosphorus coatings and/or those containing metallic or sulfur impurities have a significantly lower percent elongation, some approaching zero. A heat treatment used to increase the hardness of the coating can reduce both the strength and ductility of the coating[31]. The effect of different one hour heat treatments on the elongation at fracture of brass panels coated with a 6% phosphorus coating is shown in **figure 2-5** on page 28[32]. Prolonged heat treatment improves the ductility but reduces the hardness of the coating. "Maximum ductility and increased corrosion resistance can be obtained by heat treatment at 750 °C (1382 °F) or higher for 5 hours, followed by slow cooling to at least 200 °C (392°F) in an inert atmosphere. Typical coatings will withstand a 3 to 6 percent elongation without failure, provided the base metal is not stressed beyond its elastic limit"[33]. The use of such high temperature and prolonged heat treatments can alter the structure and properties of the base metal and distort machined shapes. The latter is a critical consideration for close-tolerance machined parts, such as those found in gas turbine engines.
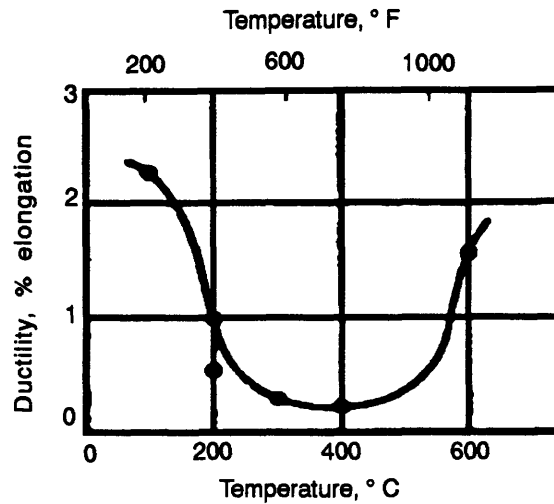
Figure 2-5. Effect of Heat Treatment on the Ductility of a 6% Phosphorus electroless nickel (from Metals Handbook, vol. 5, p. 226)

2.3.2.3   Coefficient of Thermal Expansion

The coefficient of thermal expansion for electroless nickel-phosphorus deposits is inversely proportional to the phosphorus content of the alloy. Values range from 24 x 10^{-6}/°C (13 x 10^{-6}/°F) for a 6.4% phosphorus deposit to 12 x 10^{-6}/°C (6.5 x 10^{-6}/°F) for a 11-12% phosphorus deposit. The coefficient of thermal expansion for high phosphorus coatings is approximately equal to that of Custom 450® [34].

2.3.2.4   Hardness and Wear Resistance

The high hardness and excellent wear properties of electroless nickel-phosphorus deposits are primary reasons for its many engineering applications. The as-deposited hardness of these alloys lies in the range of 500 to 600 HV_{100} or 48 to 52 Rockwell C (HRC). Heat treatment causes precipitation hardening which can produce Hardness values as high as 1100 HV_{100}, equivalent to most commercial hard chromium coatings The hardness of electroless nickel is dependent on heat treatment and independent of phosphorus content[35]. The effect of one hour

heat treatments at different temperatures on the hardness of a 10 $^1/_2$ % phosphorus coating

are shown in **Figure 2-6** [36,37].
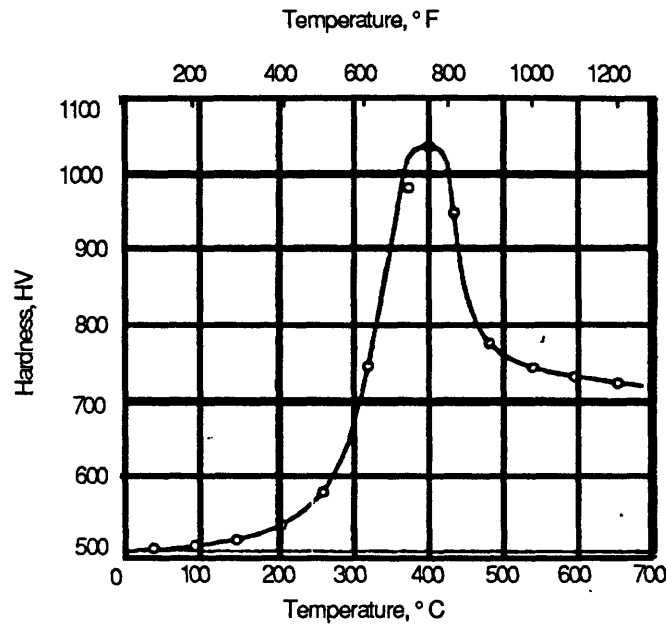
Figure 2-6. Effect of Heat Treatment at Different Temperatures
on the Hardness of 10½% Phosphorus Electroless Nickel Coating (from Metals
Handbook, vol. 5, p. 227)

High temperature heat treatments may warp and/or alter the strength of the substrate.

In order to avoid these problems, lower temperatures and prolonged exposures are used to obtain

the desired hardness. **Figure 2-7** on page 30 illustrates the time at temperature effect on the

hardness of a 10½% phosphorus coating[38].
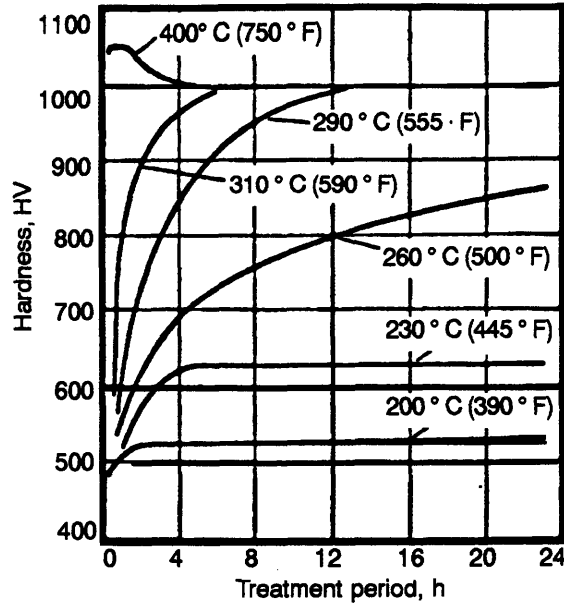
Figure 2-7. Effect of Different Heat Treatment periods on the
Hardness of a 10 1/2% Phosphorus electroless nickel
(from Metals Handbook, vol. 5, p. 227)

Electroless nickel coatings can also have excellent hardness at elevated temperatures.

The effect of elevated temperature on a 10% phosphorus coating is shown in **Figure 2-8** on page

31. In this case, the hardness of heat treated electroless nickel is equal to or better than that of

hard chromium in the range of 150°C (220°F) to 400°C (750°F). The as-deposited coatings also

retain their hardness but at a reduced level[39,40].
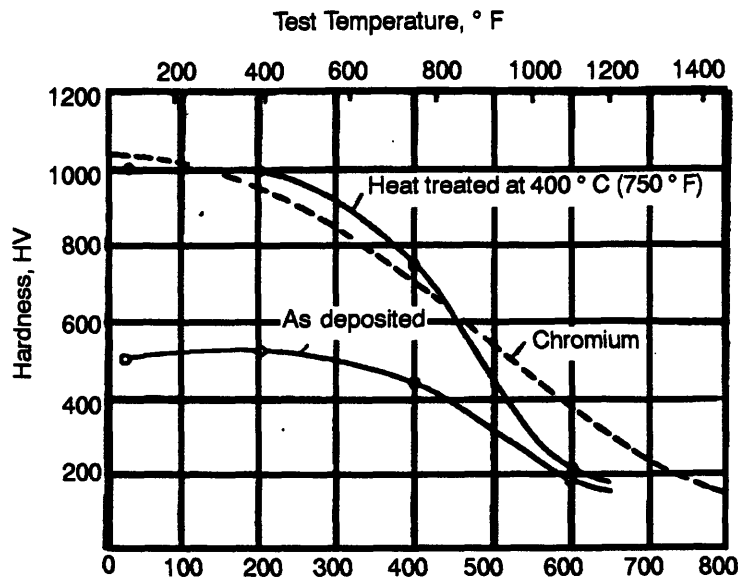
Figure 2-8. Effect of Temperature on the Elevated Temperature
Hardness of a 10% Phosphorus Electroless Nickel
(from Metals Handbook, vol. 5, p. 228)

Electroless nickel coatings also demonstrate excellent wear and abrasion resistance both
in the as-deposited and heat treated conditions. The hardness of the deposit is the most
important factor when considering wear resistance. Generally, increasing the hardness of a
deposit increases the wear resistance of the deposit. Tests conducted using a Taber Abraser
show electroless nickel-phosphorus coatings approaching the wear resistance of hard chromium
(**Table 2-3.**on page 32)[41,42,43].

Table 2-3. Comparison of the Taber Abraser Resistance of Different Engineering Coatings.

Coating	Heat treatment for one hour °C	°F	Taber wear index mg/1000 cycles(a)
Watts nickel (electrodeposited)	none	none	25
Electroless Ni-P (9% Phosphorus)	none	none	17
Electroless Ni-P (9% Phosphorus)	300	570	10
Electroless Ni-P (9% Phosphorus)	500	930	6
Electroless Ni-P (9% Phosphorus)	650	1200	4
Electroless Ni-B (5% Boron)	none	none	9
Electroless Ni-B (5% Boron)	400	750	3
Hard Chromium	none	none	2

(a) CS-10 abraser wheels, 1000 gram load, values determined as average weight loss per 1000 cycles for total test of 6000 cycles.

In wear tests using electroless nickel-phosphorus coated vee-blocks in a Falex Wear Tester, the effects of heat treatment and wear were confirmed. Under lubricated conditions, the wear resistance of electroless nickel-phosphorus deposits equalled hard chromium[44,45,46]. The effect of phosphorus content upon the wear experienced by lubricated electroless nickel coated steel balls show that high phosphorus deposits provide the best resistance to adhesive wear[47,48]. Adhesive wear is "galling". It occurs when two surfaces slide against each other with little or no lubrication. Particles from the softer material are transferred onto the harder

member by cold welding. The buildup grows and eventually breaks away from the harder material[49]. The inherent lubricity of electroless nickel coatings, provides resistance to galling. Galling of aluminum, titanium and stainless steel is effectively inhibited by coating one of the two mating surfaces with electroless nickel. The coefficient of friction for electroless nickel versus steel is about 0.13 for lubricated conditions and 0.4 for unlubricated conditions. The frictional properties of the electroless nickel-phosphorus coatings vary little with either phosphorus content or with heat treatment[50,51,52].

2.3.2.5 Corrosion Resistance

Electroless nickel is used as a barrier coating, protecting the substrate by sealing it off from the environment. The noncrystalline structure and passivity of the as-plated deposit provides corrosion resistance superior to pure nickel, electrodeposited nickel or chromium in many environments. This was particularly true for salt spray and exposure tests. The amorphorus structure has no grain or phase boundaries limiting chemical attack. Passive films develop on the surface of the coating to preclude chemical attack as well. Again, heat treatment and composition are the most important factors affecting the corrosion resistance of electroless nickel-phosphorus coatings.

In most environments, the coatings are naturally passive and very resistant to attack. Their degree of passivity and corrosion resistance, however, is strongly affected by their phosphorus content. Coatings containing more than 10% phosphorus are more resistant to attack than those with lower phosphorus contents. This is due to the increased porosity of the lower phosphorus coatings. In many instances, unwanted constituents in the deposit are more important to its corrosion resistance than its phosphorus content. Most coatings are applied from baths inhibited with lead, tin, cadmium or sulfur. The appearance of these elements in the coatings, in more than trace amounts, can cause an increase in the corrosion resistance by factors ranging from 5 to 40 times[53,54].

During heat treatment of the nickel-phosphorus coating, the precipitation of nickel phosphide reduces the phosphorus content of the remaining material and increases the porosity. The nickel phosphide particles create small active/passive corrosion cells, further contributing to the destruction of the coating. As the coating hardens, it also shrinks. This can crack the coating and expose the substrate to chemical attack. Coatings heat treated "in air have the best [corrosion] resistance due to the formation of strongly adhering oxides, which seal the pores and create a continuous passive surface..."[55].

2.4   Fatigue

Since the mid-nineteenth century, it has been observed that a metal which is subjected to repeated stress cycles is likely to fail at stresses much lower than the ultimate tensile strength and often below the yield strength. This phenomena is called "fatigue". Failures attributed to the slow growth of minute cracks due to fluctuating stresses are called fatigue fractures. The study of fatigue has become increasingly more important with the advent of sophisticated equipment (e.g. aircraft, automobiles, pressurized cylinders, turbines, etc.) which is subjected to repeated loading-unloading cycles[56].

The current ASTM definition of fatigue is as follows:

The process of *progressive localized* permanent structural change occurring in a material subjected to conditions which produce fluctuating stresses and strains at some point or points and which may culminate in cracks or complete fracture after a sufficient number of fluctuations[57].

The word "progressive " in this definition emphasizes the fact that the mechanisms involved in fatigue failures have usually been operating for a significant period of time prior to failure. The word "localized" implies the mechanisms operate at local areas of high stresses and strains rather than throughout the entire structure[58]. These local areas of high stress or strain may be caused by sharp corners or notches, points of high residual stress, or at metallurgical stress concentration sites such as voids and inclusions[59].

There are three major stages of fatigue leading to fatigue failure or fracture: (1) crack initiation, (2) crack propagation and (3) fast fracture. The first stage, crack initiation, results from damage caused by surface scratches and/or persistent slip bands. The second stage, crack propagation, is composed of two parts: Stage I and Stage II crack growth. Stage I crack growth occurs along the persistent slip planes and Stage II crack growth occurs along planes of high tensile stress, in a direction normal to the maximum tensile stress. The second stage of fatigue continues until the crack has grown to its critical size. This critical size is reached when the remaining cross section of the structure can no longer withstand the applied load. Then the third and final stage, fast fracture occurs. This is the rapid fracture of the remaining cross section into two or more parts.

2.4.1   Crack Initiation and Propagation

Various models have been proposed to describe the initiation of fatigue cracks due to localized regions of plastic deformation (persistent slip bands). Wood's model, is presented in **figure 2-9** on page 36[60]. During the increasing portion of the load cycle (a), slip occurs on favorably oriented slip planes. These new surfaces undergo oxidation and strain hardening. Therefore, during the decreasing portion of the load cycle (b) slip occurs on different (parallel) slip planes, in the reverse direction. This first cycle leads to **figure 2-9** (c), which schematically illustrates an extrusion and an intrusion. After many cycles, continuing plastic flow can cause the intrusion to become a stage I crack (d). This process, as seen on the surface of a fatigue specimen, is shown in **figure 2-10** on page 36.
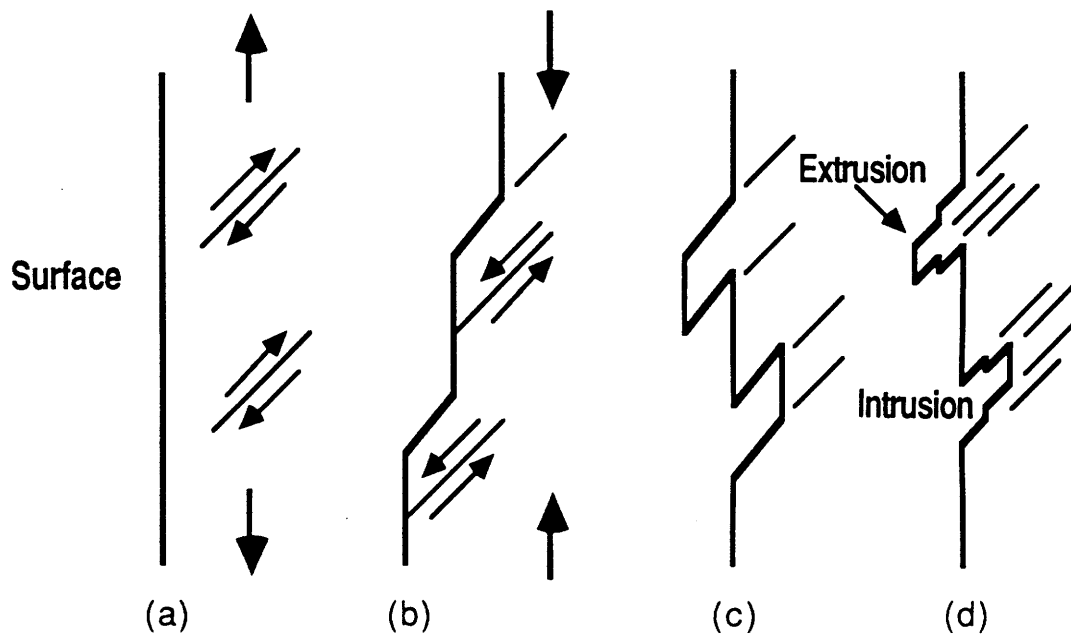
Figure 2-9. Schematic of Wood's Model for Fatigue Crack Initiation
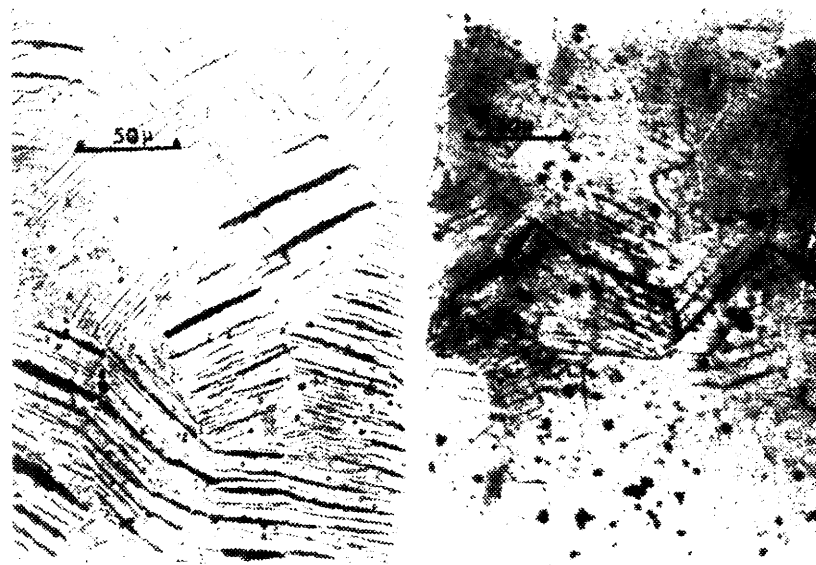
a. Intrusions and extrusions; b. Slip band crack

Figure 2-10. SEM Micrograph of Crack Initiation on an Al-Alloy Sample[61]

The deepening of this initial crack along planes of high shear stress is called a persistent slip band. It precedes the Stage I crack, which will propagate for only a few grain diameters before becoming a Stage II crack. The stage II crack is well defined and grows on planes normal to the maximum tensile stress. There is a good deal of ambiguity, however, in defining when a deepened slip band, or intrusion, is large enough to be a crack[62,63]. Stages I and II fatigue crack growth are shown schematically as a microscopic edge view in **figure 2-11**. Most fatigue cracks grow in a transgranular manner (as shown in the figure); essentially perpendicular to the stress and without regard to the grain boundaries. Cracks may also grow in an intergranular manner; along the grain boundaries. This will usually occur only when there are many impurities at the grain boundaries, in cases involving corrosion, hydrogen embrittlement, or at high temperatures.
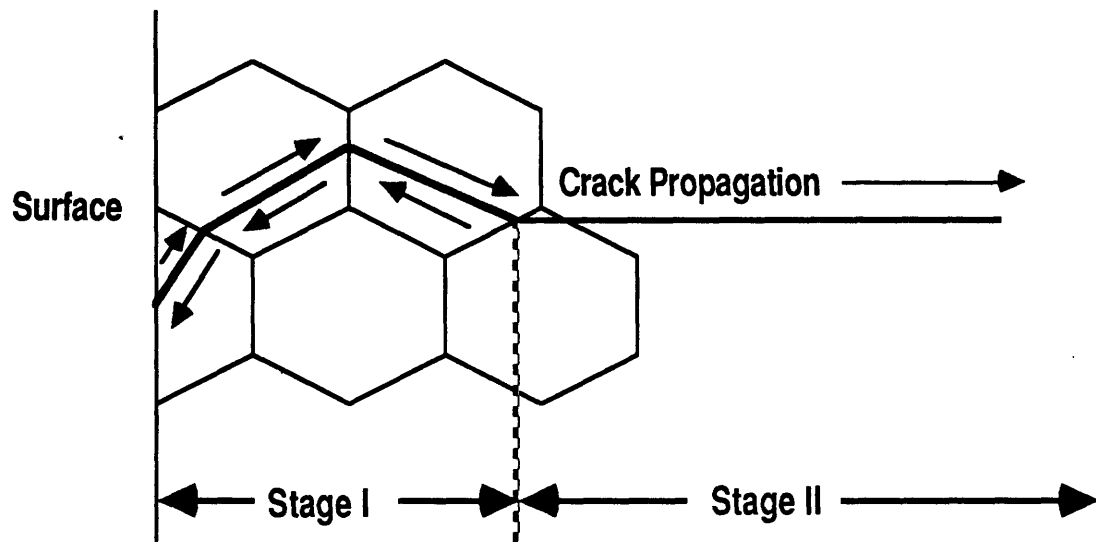
Figure 2-11. Schematic of Stage I and Stage II Crack Growth

It has been suggested that stage II crack propagation may occur by plastic blunting or by alternating shear[64,65]. Wood's model for the platic blunting hypothesis is illustrated in **figure 2-12** on page 39[66]. As explained by Broek[67], the sharp crack in tension in part (a) of the figure can slip along a favorable slip plane, (b), because of the large stress concentration at

the tip. The crack has now opened and extended in length, such that slip may now occur on a different plane, (c). Increasing stress and work hardening will activate other, parallel, slip planes, eventually leading to a blunt crack tip (d). The crack length, a, has now increased by an amount Δa during the increasing load portion of the cycle. The crack has propagated by plastic shearing. At the crack tip there exists a plastic zone which is surrounded by material which is elastic. The elastic region will contract during the decreasing load portion of the cycle and exert compressive stresses on the plastic region. At the crack tip, these stresses are above the yield stress and the slip direction is now reversed. This causes reverse plastic deformation which compresses the crack faces together, forcing the blunt crack surfaces which were created in tension into the plane of the crack. Here, it partially folds by buckling to resharpen the crack tip (e)[68]. The cyclic opening and closing of the crack tip in **figure 2-9** (a-e) and (f-g), will therefore cause ripples in the fracture surface; each cycle forming a new ripple. These ripples, called fatigue striations, can be seen in the scanning electron microscope (SEM). An example of fatigue striations in an Al-Cu-Mg alloy is presented in **figure 2-13** on page 40.
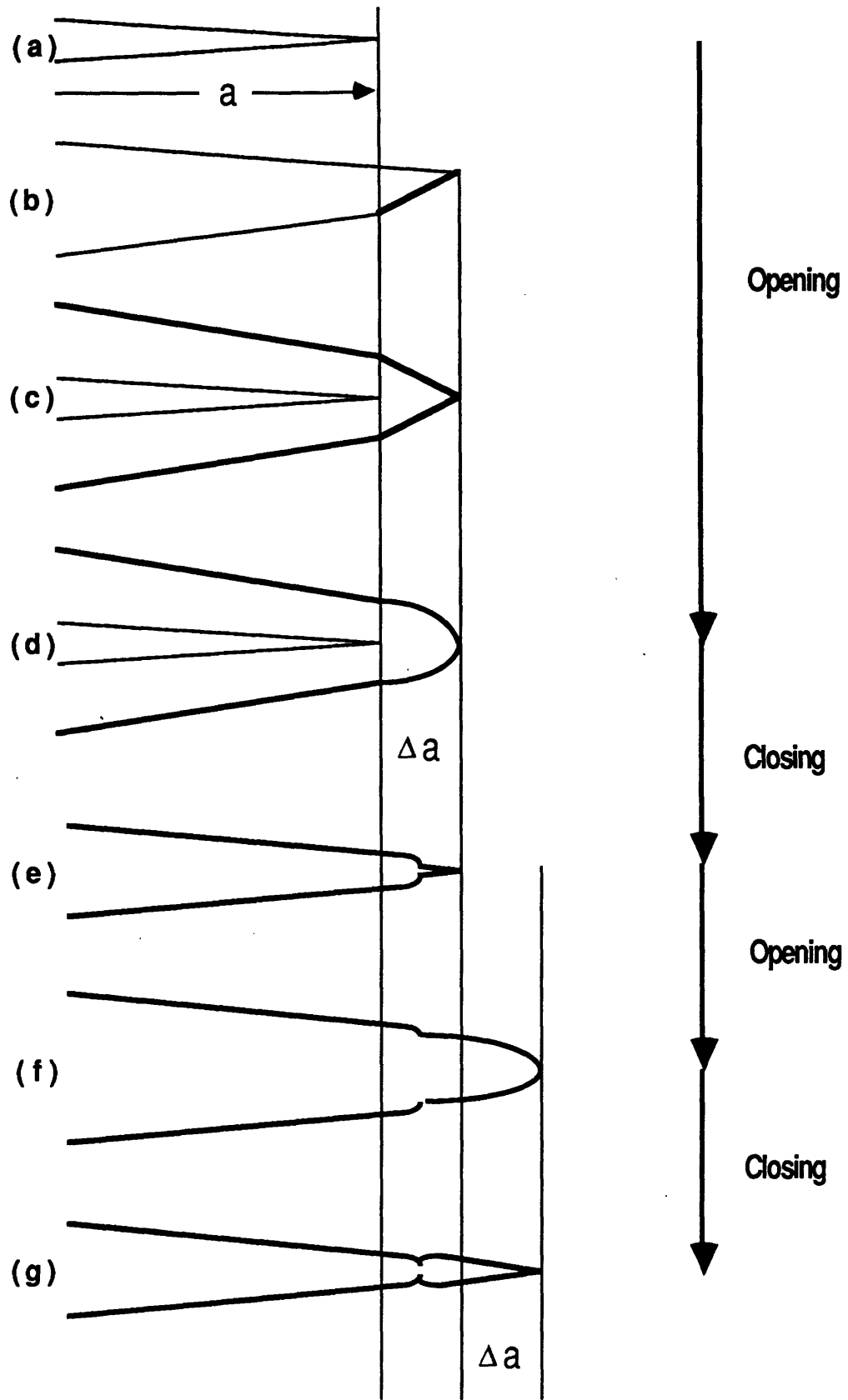
Figure 2-12. Wood's Model of Crack Extension by Plastic Blunting
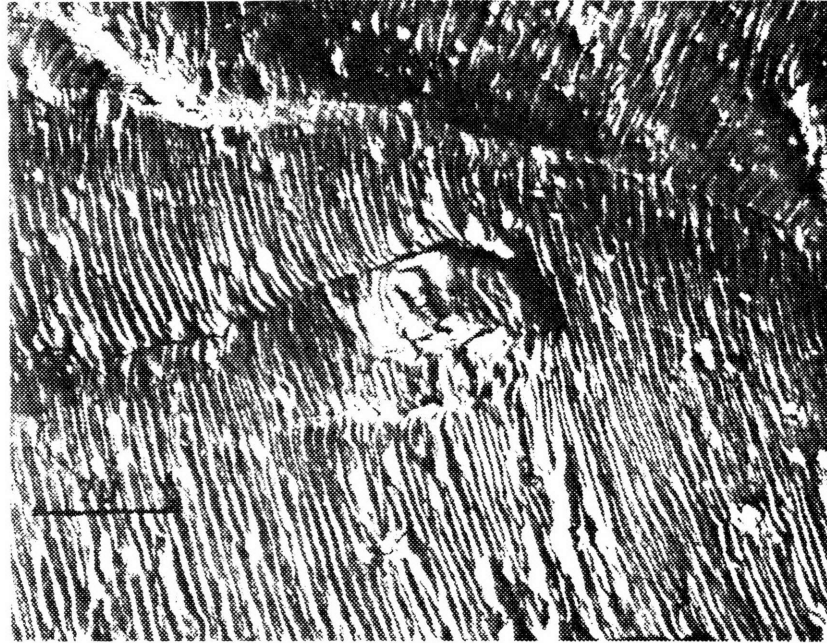
Figure 2-13. Fatigue Striations in Al-Cu-Mg[69]

The major evidence against this theory was first presented by Meyn[70] when he showed that fatigue striations do not form when fatigue tests are performed in a vacuum. He explained his results by attributing the striations to environmentally assisted cracking. This explains the absence of striations on samples tested in a vacuum, where oxidation of freshly exposed surfaces does not occur. Meyn's tests were limited to crack growth rates below 0.5 microns/cycle.

Pelloux presented a model for the mechanism of the formation of ductile fatigue striations[71]. To describe the model, consider the single edge notch, plane strain tensile bar in **figure 2-14**(a) on page 41. McClintock demonstrated that deformation can only occur on planes parallel to AB and AC and that it may occur either alternately on each plane or simultaneously[72]. It is clear that if shear starts on a plane, say AC in **figure 2-14**(b), then strain hardening on plane AC will cause shear to be easier on a plane parallel to plane AB, for example A'B'. In this manner, shear will tend to be alternating, **figure 2-14**(c). Pelloux further explained that this sliding leads to the formation of a 90° notch tip which always remains sharp.
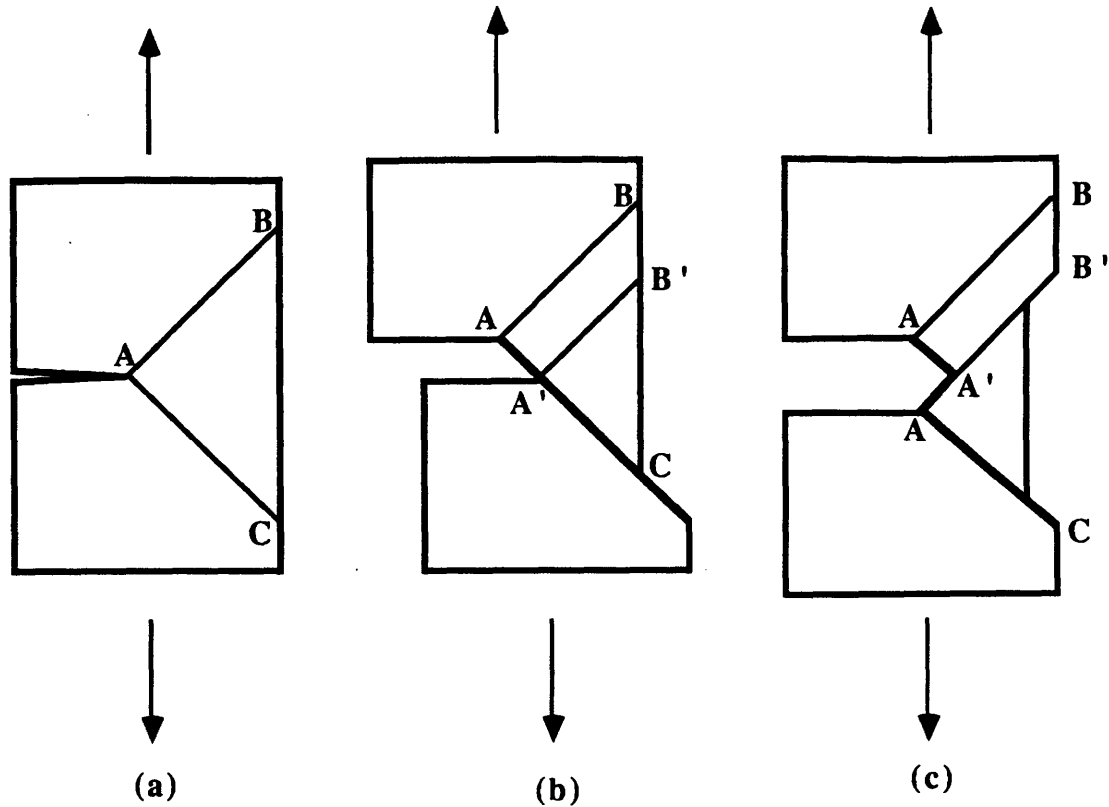
Figure 2-14. Pelloux's Model of Crack Extension by Alternating Shear in a Singly Notched Tensile Specimen[73]

Under ideal conditions, this process would be completely reversible (i.e. slip on a plane AB could occur opposite to its original direction, placing the atoms back to their original positions). In air, however, the new surfaces will be oxidized, limiting the amount of reversed slip. Pelloux's model for fatigue crack propagation is presented in **figure 2-15** on page 42. **Figure 2-15(a)** accounts for the fatigue striations which occur when samples are tested in air, when no reversed slip occurs. **Figure 2-15(b)** accounts for the case when samples are tested in a vacuum, where reversed slip occurs and no striations form.

(a) No Reversed Slip
(Oxidation)

(b) Reversed Slip
(Vacuum)
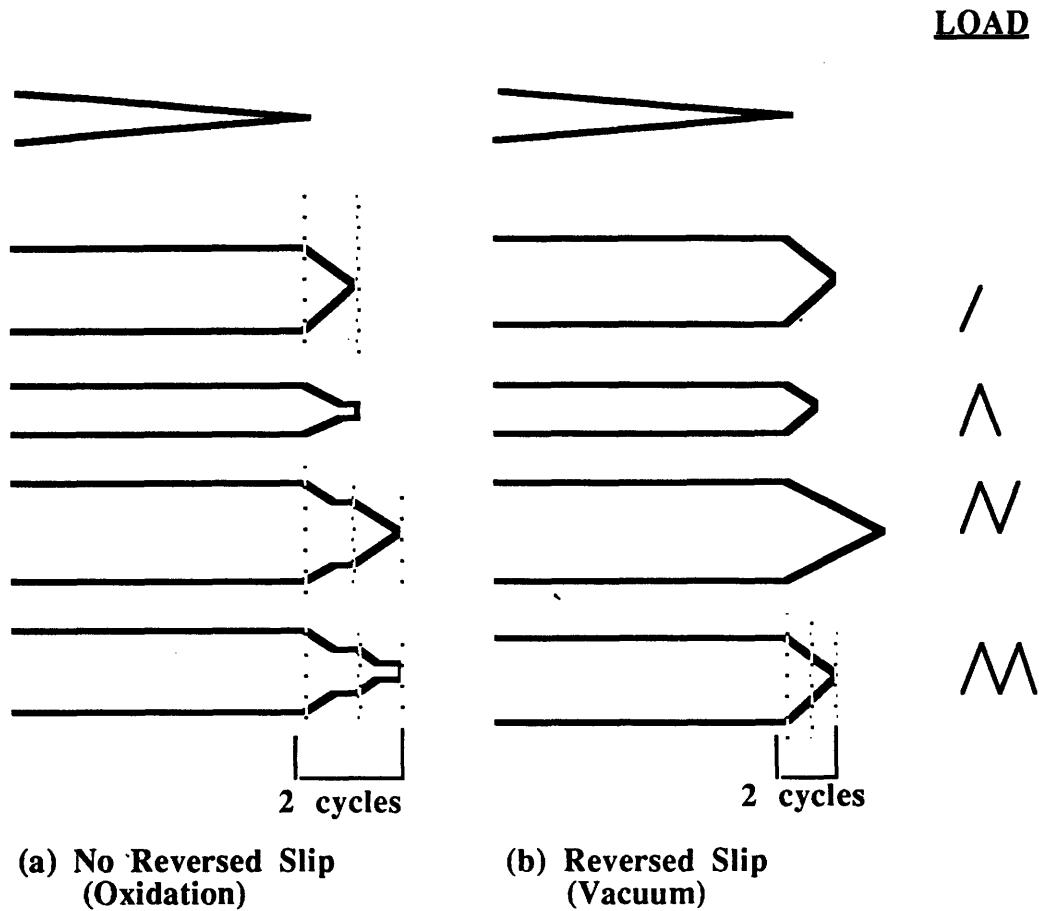
Figure 2-15. Pelloux's Model of Crack Propagation After Two Load Cycles[74]

Pelloux concluded that fatigue striations result from an environmental factor at crack growth rates below 5 microns/cycle, not by plastic blunting. Wood's model, however, may be accurate at growth rates above 10 microns/cycle.

The third stage of fatigue failure is the final, sudden fracture of the remaining material. This region of the fracture surface exhibits characteristics of ductile fracture and it may often contain deformation markings which point to the source of the initial fracture location[75].

Fatigue is usually divided into high cycle and low cycle fatigue. Low cycle fatigue is associated with high stresses and cracks which form very early. High cycle fatigue, when the number of cycles to failure ($N_f \geq 5 \times 10^4$ for example) is associated with very low stresses. A

large portion of the fatigue life is therefore spent initiating a crack. Although there is not a clear separation between high cycle and low cycle fatigue, fatigue is usually called low cycle when stresses are often high enough to develop significant bulk plastic strains[76].

2.4.2 Constant Displacement Amplitude Fatigue Testing

Fatigue failures are caused by a sufficient variation or fluctuation in applied stress and a large enough number of cycles of the applied stress. The fluctuating stress cycle is simplified and considered to be made of two components, a mean stress σ_m and an alternating stress σ_a. The range of stress, σ_r, is defined to be the algebraic difference between the maximum and minimum stress in a cycle, and the alternating stress is one-half the range of stress. Therefore we have the following equations[77]:

$$\sigma_r = \sigma_{max} - \sigma_{min} \qquad \text{(equation 2.4.2-1)}$$

$$\sigma_a = \sigma_r/2 \qquad \text{(equation 2.4.2-2)}$$

$$\sigma_m = (\sigma_{max} + \sigma_{min})/2 \qquad \text{(equation 2.4.2-3)}$$

Two other quantities are used in presenting fatigue data in terms of stress ratios:

$$R = \sigma_{min}/\sigma_{max} \qquad \text{(equation 2.4.2-4)}$$

$$A = \sigma_a/\sigma_m \qquad \text{(equation 2.4.2-5)}$$

The basic method of representing fatigue data is by means of an S-N curve. The S-N curve is a plot of the stress amplitude (S) versus the number of cycles to failure (N_f). During the S-N test, the stress range, stress amplitude, cyclic frequency and wave form are controlled. The log of the stress amplitude is plotted on the ordinate axis. The number of cycles to failure is plotted on the abscissa on a log scale. **Figure 2-16** on page 44 is a typical S-N curve. The

horizontal portion of the curve at high stress is usually obtained at a σ_{max} near the static tensile strength of the material. Below this stress, the number of cycles to failure steadily increases with decreasing stress. The low-stress regime on the horizontal portion of the S-N curve in **figure 2-16** is called the *fatigue endurance limit*. Below this stress, the material can withstand an infinite number of cycles without failure. The fatigue endurance limit is a characteristic of steels and titanium, but not of most nonferrous materials. Most nonferrous metals have S-N curves with slopes which gradually decrease with increasing number of cycles beyond 10^6 cycles, represented by the unbolded line in **figure 2-16**. These materials do not have fatigue endurance limits and the *fatigue strength* is usually characterized by the stress amplitude at which the material will withstand a given number of cycles, for example 10^7 cycles.
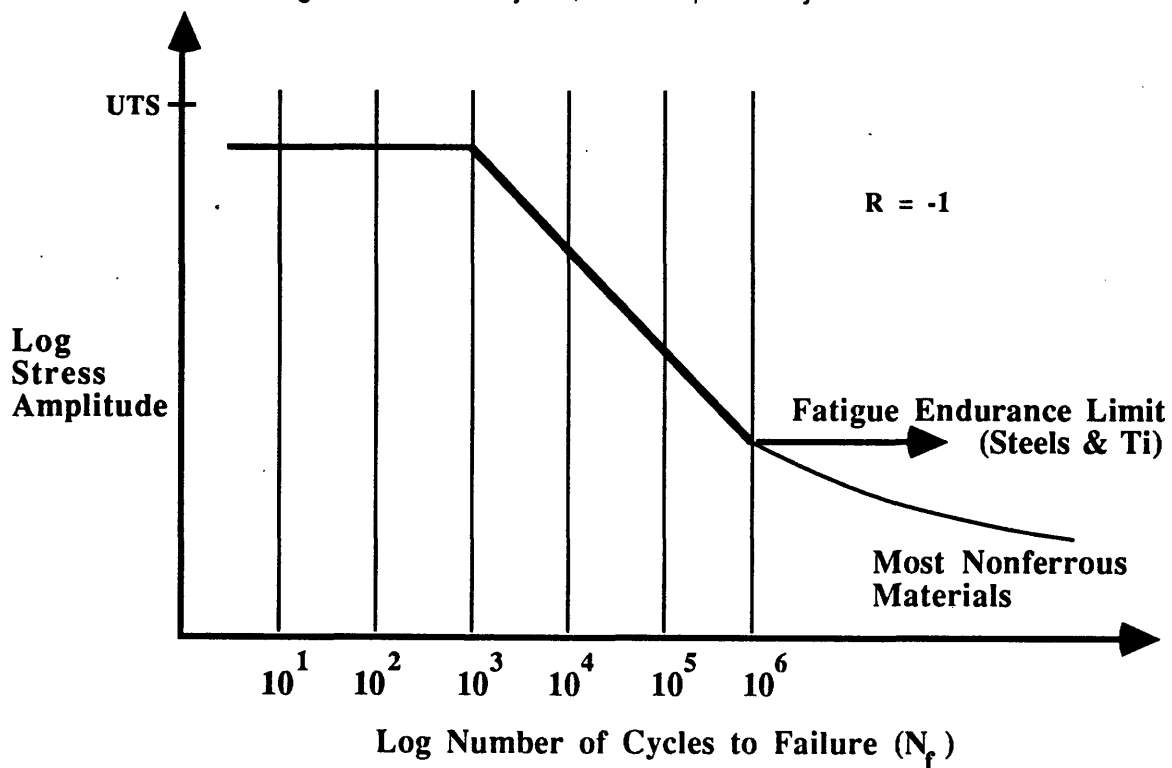
Figure 2-16. Typical S-N Curve

In the high cycle fatigue regime (HCF, $Nf \geq 5 \times 10^4$), the stress, on a macroscopic scale, is elastic, but on a microscopic scale the state of stress causes highly localized plastic

44

deformations. At higher stresses the fatigue life is decreased, but the large amount of plastic deformation makes stress analysis very difficult. Generally, tests done in the low cycle fatigue (LCF) region are conducted with controlled elastic plus plastic strain instead of controlled load or stress cycles[78].

A constant displacement cantilever bending test machine was used in this research work. With this type of machine, a rotating cam produces a constant beam deflection amplitude, at a specific frequency. The load produced by the machine interacting with the test specimen changes with specimen cyclic hardening or softening and decreases as cracks develop and propagate through the specimen. As a result, for a given initial stress amplitude the constant displacement test machines give longer fatigue lives than the constant load amplitude machines for the same calculated stress. However, the constant displacement machines provide the flexibility to vary the mean deflection (initial mean stress). This cannot be achieved with rotating constant load amplitude machines[79].

The range in the number of cycles to failure among identical test specimens for a specific displacement or stress level is called *scatter*. The scatter in fatigue testing is a very important consideration in interpreting and using fatigue data. Scatter can be attributed to testing techniques, specimen preparation, variations in material, and variability of the fatigue mechanisms. The greater scatter at low stress levels in smooth specimens can be attributed to the greater percentage of life needed to initiate small microcracks. At higher stress levels a greater percentage of the fatigue life involves propagation of macrocracks. Tests involving only fatigue crack growth under constant amplitude conditions usually show scatter factors of 2 or 3 or less for identical tests. Thus the greatest scatter in fatigue involves the initiation of microcracks. In notched specimens and components, cracks form quicker, and subsequently a greater proportion of the total fatigue life involves crack propagation with less scatter[80]. Fatigue studies conducted by Sinclair and Dolan[81] showed that the data points obtained from fatigue testing unnotched 7075-T6 aluminum specimens at R = -1 followed a log-normal distribution. This statistical method is good at determining mean values, but is inaccurate at the

45

extremes of the distribution (probabilities of 1 percent or less). In engineering applications, it is often important to predict upper and lower bound values with a measure of confidence (statistical probability). The Weibull distribution is used for these predictions.

2.4.3   Residual Stresses in Nickel-Phosphorus Coatings

It is well recognized that fatigue failures start at the surface. It appears logical for bending and torsion loading, where the maximum stress is at the surface. However, in axial loading as well, fatigue failures nearly always begins at the surface. Fatigue properties are very sensitive to surface condition. Factors which can effect the fatigue properties are divided into three categories: (1) surface roughness which is a measure of the stress concentration at the surface, (2) changes in the fatigue strength of the metal, and (3) changes in the residual stress condition of the surface[82]. Siebel and Gaier[83] demonstrated how the fatigue life of cantilever-beam specimens vary with the type of surface preparation. Smoothly polished specimens, which had fine scratches oriented parallel to the direction of principal tensile stress, gave the highest values in fatigue life. Surface finish plays an important role in determining fatigue life.

Altering the surface fatigue strength of materials can be done by plating or by heat treatment. The fatigue strength of aluminum alloy sheet is reduced when a soft aluminum coating is applied to the stronger age-hardenable aluminum alloy sheet. Generally, placing a softer or brittle material coating over a stronger more ductile substrate is detrimental to fatigue life. Likewise, placing a stronger and more ductile coating over a softer more brittle coating, will increase fatigue life. Plating conditions used to produce electroplated and electroless coatings can have significant effects on the fatigue properties, since large variations in residual stress, adhesion, porosity and hardness of the coating can be produced. The phenomena known as decarburization is particularly detrimental to the fatigue performance of heat-treated steel[84].

Residual stress, also known as self-equilibrating stress or self-stress, is stress which remains in an article after a processing operation. The operation can be a material processing

technique, a service overload, and/or the result of environmental conditions. Residual stresses exist in most manufactured parts[84].

Residual stress can be visualized as *locked-in stress* present in an article which is not subjected to an external force. It is well recognized that fatigue failures are associated with tensile stresses. Reducing the tensile mean stress improves the fatigue life. Tensile mean applied stresses can be reduced by the presence of compressive residual stresses locked in the material. Therefore compressive residual stress present in an article will tend to diminish the effect of any imposed tensile stress, thereby improving the fatigue properties of the article. Mechanical and thermal treatments are used to produce compressive surface residual stresses in materials subjected to cyclic loading. These include but are not limited to: shot-peening, surface rolling, overloading, carburizing, nitriding, induction hardening and severe quenching of carbon steel. Residual stresses persist as long as the sum of the residual stresses and applied load stresses do not exceed the yield strength of the material. In other words, they begin to *fade* as soon as plastic deformation is introduced.

Residual stresses are present in electroless nickel coatings. They are the result of two factors, (1) a thermally induced state of stress and (2) an intrinsic state of stress. The thermal stress is caused by the differences in thermal expansion between the coating and the substrate. The electroless nickel plating process occurs at temperatures between 87 to 93°C (190-200°F). The amount of thermal stress present in the coating is dependent on the differences in coefficient of thermal expansion between coating and substrate and the temperature change from processing temperature to the end use environment. The intrinsic stress is a residual stress generated by a structural change during heat treatment. Heat treatments above 220°C (430°F) cause a volumetric shrinkage of between 4 to 6 percent. This shrinkage increases the tensile stresses[85,86].

Residual stresses are measured in thin strips by one of three different methods: (1) spiral contractometer, (2) x-ray diffraction and (3) by measuring the deformation (curvature) of thin metal strips after plating. The spiral contractometer is a measurement devise which

47

consists of a helical strip and an indicating system. The helix is plated in an identical manner as a test article, the residual stress generated by the plating process causes the helix to wind more tightly or unwind. A gear train network is connected to this movement and results in a needle deflection. The residual stress is calculated based on the needle deflection and calibration data[87]. The x-ray diffraction method measures the lattice spacing of atoms by the diffraction of x-rays. The change in lattice spacing is translated to a residual stress. The third method involves the calculation of residual stress based on the curvature resulting from the plating of straight thin metal strips.

Walker and Goldsmith[88] conducted X-ray diffraction studies of electroless nickel-phosphorus coatings on a 25 um molybdenum film. They concluded that the thermally induced stress due to heat treatments from 400 to 680°C (750-1256°F) caused wide spread cracking in the coating. Their observations showed that the reductions in stress were proportional to the degree of cracking in the coatings. Cracking is a stress relief mechanism.

Parker and Shan[89] measured the residual stress in electroless nickel coatings by observing the deformation of thin metal strips and concluded that the residual stress was dependent on the phosphorus content of the coating. Increasing deposit thickness also reduced the stress in the coating. The residual stress found in nickel-phosphorus coatings used on steel containing more than 10% phosphorus was zero or compressive. Lower phosphorus deposits demonstrated tensile stresses in the range of 15 to 45 MPa (2.2 to 6.5 ksi). They also attributed the residual stress to differences in thermal expansion between the deposit and the substrate. The coefficient of thermal expansion for high phosphorus coatings ($10^1/2$% phosphorus) is 12 x 10^{-6} m/m°C (6.5 x 10^{-6} in/in°F), equal to that of most steels and close to the value reported for Custom 450® (10.8 x 10^{-6} m/m°C).

The codeposition of orthophophites, heavy metals, and /or the presence of excess complexing agents in the plating solution can increase the residual stress levels in the deposit. Small quantities (5 mg/L or 20 mg/gal) of bismuth or antimony added to most baths can cause

tensile residual stresses to increase to as much as 350 MPa (50 ksi). Tensile residual stresses reduce the ductility of the coating and increase cracking and porosity[90,91,92].

2.4.4 Fatigue Performance of Nickel-Phosphorus Coatings

Electroless nickel-phosphorus coatings tend to crack under cyclic loading. As a result, the fatigue strength and endurance limit of the steel substrate is reduced. The magnitude of the reduction in fatigue strength is dependent on the coating composition, heat treatment, thickness of the coating and the fatigue strength of the substrate[93]. The fatigue performance of electroless nickel on high strength stainless steel has not been extensively evaluated. As will be shown, the results of previous fatigue studies have been difficult to interpret without additional details, such as the phosphorus content of the evaluated coating.

In the Soviet Union, L. N. Gazez'yan and E. N. Romanova[94] conducted cantilever bending tests of 30 KhGSA and E-1415 steels coated with 20 microns (.8 mils) of electroless nickel-phosphorus. The nickel phosphorus coatings were from acid bath solutions, but no exact phosphorus content was reported. The fatigue limit set for the tests was 10^7 cycles. The results of these tests are presented in **Table 2-4**.

Table 2-4. Fatigue test Results of a 20 micron Electroless Nickel-Phosphorus Deposit on 30 KhGSA and El-415 Steels[95]

Steel	Surface of the Specimen	Fatigue Strength Limit kg/mm^2	
		without notch	with notch
30 KhGSA	not coated	52	26
30 KhGSA	nickel plated	50	16
El-415	not coated	60	35
El-415	nickel plated	50	24

For Specimens coated with electroless nickel without a notch, **Table 2-4** shows a 3.8% decrease in fatigue strength for 30 KhGSA steel and a 17% decrease in fatigue strength for El-

415 steel. Notched specimens with coatings reduced fatigue strength by 40% and 30% respectively.

V. A. Antskaitis[96] conducted cantilever bending fatigue tests on 30 KhGSA steel with several different coatings at various thicknesses. **Table 2-5** provides the results.

Table 2-5. The Influence of Various Coatings on the
Fatigue Strength of 30 KhGSA Steel[97]

Nature of the Sample	Thickness of the coating (microns)	Fatigue Strength Limit kg/mm^2	
		without notch	with notch
Steel (no coating)	0	50	26
Electroless nickel (acid)	8-10	52	22
Electroless nickel (acid)	18-20	44	20
Electroplated nickel	8-10	24	16
Chromium-plated steel	8-10	42	18
Zinc-plated steel	7-10	52	26

Table 2-5 shows a 4% improvement in fatigue strength for un-notched specimens coated with 8-10 microns of electroless nickel-phosphorus and a 12% decrease in fatigue strength for un-notched specimens coated to a thickness of 18-20 microns. As plating thickness increased, the fatigue strength decreased for both notched and un-notched specimens. In these tests, electroless nickel coatings out performed the chromium and electrodeposited nickel coatings.

V. S. Borisov and S. A. Vishenkov[98] studied the fatigue strength of several steels plated with electroless nickel-phosphorus coatings under different conditions. These fatigue tests were done using a fatigue bending machine to a fatigue limit of 10^7 cycles. The results for tests conducted on 40 KhNMA steel are located in **table 2-6** and the results for 30 KhGSA and 30 KhGSNA steels are in **table 2-7**.

Table 2-6. Fatigue Strength Tests on 40 KhNMA Steel
with 30 Microns (1.2 mils) Electroless Nickel-Phosphorus(acid bath)[99].

Nature of Samples	kg/mm^2	Fatigue Strength Limit Compared with steel,%
Steel without heat treatment	61	100
Steel after heat treatment (1 hour 400°C)	61	100
Electroless Nickel coated steel without heat treatment	60	98.5
Electroless nickel coated steel after heat treatment (1 hour 400°C)	33	54

Table 2-7. Fatigue Strength Tests on 30 KhGSA and 30 KhGSNA Steels
Coated with 20 Microns (0.8 mils) of Electroless Nickel-Phosphorus.
All Specimens Heat Treated for One Hour at 400°C[100].

Nature of Samples	kg/mm^2	Fatigue Strength Limit compared with steel, %
30 KhGSA Steel	64	100
Same, Electroless nickel coated	38	59
30 KhGSNA Steel	76	100
Same, Electroless nickel coated	44	58

As can be seen in **table 2-6**, when a 30 micron thick deposit of nickel-phosphorus is placed on 40 KhNMA steel and followed by heat treatment, the fatigue strength is reduced by 46%. The 20 micron thick electroless nickel-phosphorus coatings applied to 30 KhGSA and 30 KhGSNA steels reduced the fatigue strength by 41% and 42% respectively. The heat treatments are known to cause cracking in these coatings, thus reducing fatigue life.

Recent fatigue tests have shown high phosphorus deposits tend to resist cracking more effectively than low phosphorus deposits. As-deposited coatings containing 10$\frac{1}{2}$ percent or more phosphorus have compressive residual stresses which reduce the effects of tensile stresses resulting from heat treatments. Heat treating a high phosphorus coating can cause tensile residual stress to develop[101]. Slaigle[102] at the University of Miami conducted fatigue testing on 4130 steel heat treated to ultimate tensile strength levels of 1100 to 1240 MPa (160,000 to 180,000 psi). The steel specimens were plated with a 12 percent phosphorus electroless nickel

coating and evaluated against a control group of unplated specimens. The fatigue testing results demonstrated only a slight degradation (less than one percent) in fatigue strength for the electroless nickel coating. However, there is some skepticism concerning the results because of the presence of a decarburized zone on the surface of the unplated specimens. Microhardness tests (25g Knoop) indicated the surface of the 4130 steel was the equivalent hardness of about 20 HRC or a strength level of about 760 MPa (110,000 psi). Thus, these results reconfirm fatigue performance studies of electroless nickel coatings on lower strength steels[103].

In Japan, H. Izumi, H. Sunada and Y. Kondo[104] conducted rotary bending fatigue tests of S20C (comparable to 1020 steel) and S55C (comparable to 1055 steel) carbon steels. Their results showed a 17% increase in fatigue strength for specimens plated with electroless nickel-phosphorous. The pH of the bath solution was not controlled, nor was the phosphorus content of the coatings reported. Their results also demonstrated that the increase in fatigue strength was independent of plating thickness and independent of heat treatment (one hour) temperature between the range of 100 to 400°C. They attributed the improvement in fatigue strength to: (1) the excellent throwing power of electroless nickel making an irregular surface more smooth, (2) the high hardness and relative strength of the coating and (3) the electroless nickel coated steel behaves like a clad steel. Subsequent research work by Kondo, Sunada and Izumi[105] has also shown that electroless nickel-phosphorus coatings can improve the fatigue strength of carbon steels when the stress concentration factor is less than 2. These results were obtained by using rotary bending machines and evaluating notched and un-notched specimens with and without electroless nickel-phosphorus coatings. The un-notched coated specimens demonstrated a 10% improvement in fatigue strength for S20C carbon steel and a 16% improvement in fatigue strength for S55C carbon steel. When the stress concentration factor was greater than 2, the fatigue strength of coated specimens was approximately 15 to 20% lower than the uncoated specimens.

Hydrogen embrittlement is another factor which must be taken into account when processing stainless steel substrates for subsequent electroless nickel plating. The intrusion of

hydrogen at the grain boundaries of steels causes surface defects (crack initiation sites), thereby reducing the fatigue life of the steel. Hydrogen embrittlement relief is recommended for high-strength steel, especially if cathodic pickling or a Woods nickel strike is used in the pretreatment. This can be accomplished by baking the material at 200°C for several hours as soon as practical after electroless nickel plating[106]. The manufacturer of Custom 450® stainless steel specifies a 1 to 3 hour bake at 149-177°C (300-350°F) to remove hydrogen[107].

3. EXPERIMENTAL PROCEDURES

3.1 Overview

This section describes the procedures followed to evaluate the fatigue performance of three commercial electroless nickel coatings on a substrate of custom 450® stainless steel. A coating thickness of 25 microns (1.0 mils) was chosen for the evaluation. Actual thicknesses for each group of coatings varied from 24 to 30 microns (0.99 to 1.2 mils). The heat treatments chosen were recommended by the coating manufacturers based on their knowledge and experience with the coating. The proprietary coatings evaluated were:

(1) Lea-Ronal NICKELMERSE SPL coating plated by Teledyne Neosho, Neosho, Missouri. LeaRonal NICKELMERSE SPL is an 8 to 10 percent phosphorus electroless nickel coating. Teledyne Neosho heat treated the specimens for one hour at 274°C (525°F). Their pretreatment process incorporated glass bead blasting at 30 psi.

(2) Enthone NI-422 coating plated by Enthone Incorporated, New Haven, Connecticut. Enthone NI-422 is a 10 to 12 percent phosphorus electroless nickel coating. Enthone Inc. heat treated the specimens for four hours at 191°C (375°F) to provide hydrogen embrittlement relief.

(3) Enthone NI-426 coating plated by Enthone Incorporated, New Haven, Connecticut. Enthone NI-426 is a 1 to 3 percent phosphorus electroless nickel coating. Enthone Inc. heat treated two groups of fourteen specimens for four hours at 191°C (375°F) to provide hydrogen embrittlement relief. One group of these specimens received an additional one hour heat treatment of 366°C (690°F) at M.I.T. to maximize the hardness and wear resistance of the coating.

In order to evaluate the coatings objectively, all specimens were prepared in an identical manner before plating. The remainder of this section is devoted to specimen processing.

Two pieces of custom 450® stainless steel sheet, 91.4 cm x 25.4 cm (36 in x 10 in), with a thickness of 1.6 mm (0.063 in) were received from the manufacturer. The stainless steel sheets were delivered in the cold rolled, unannealed condition. The cold rolling caused a 15 cm (6 in) "bow" over a length of 91 cm (36 in). The term "bow" is used to describe the curvature of the sheets resulting from the cold rolling of steel. The two pieces of sheet were cut into 72 rectangular specimen blanks, 9.5 cm x 6 cm (3.75 in x 2.375 in), with the major axis of the rectangle aligned in the rolling direction. After cutting, there were 18 small pieces of sheet stainless steel remaining. These small narrow pieces, 9.5 cm x 1.9 cm (3.75 in x 0.75 in), were kept for metallography and tensile tests. A metallographic specimen was cut from a specimen blank for analysis.

The seventy-two specimen blanks and eighteen small pieces were annealed in accordance with manufacturer's procedures. They were annealed in air in a furnace at a temperature of 1040°C (1905°F) for one hour followed by air quenching. An effort to remove the "bow" from the specimens was attempted by placing a 10 kg (22 lb) weight on top of the specimens inside the furnace. The deformation from cold rolling remained. A metallographic sample was taken from a specimen blank in the annealed condition.

The specimens were aged to meet AVCO LYCOMING material specifications for hardness. Proprietary information concerning the age hardening procedure was obtained through the U.S. Coast Guard[108]. The age hardening procedure specified by AVCO LYCOMING did

54

not produce the necessary hardness values. A time at temperature versus hardness analysis was conducted to determine the proper temperature and time necessary to achieve a particular hardness.

A fixture was constructed to remove the "bow" from the specimens by "squeezing" them flat during the age hardening process. The fixture consisted of two rectangular flat plates held together by four nuts and bolts. The plates were made of 304 stainless steel 9.5 mm (0.375) thick. The specimens were placed in-between the two plates and then the four sets of nuts and bolts were tightened as much as possible to force the specimen blanks flat against the plates. The size of the fixture allowed only 10 specimens to be aged at one time. The specimens were aged in air in 7 groups of 10 specimens at a temperature of 570°C (1058°F) for $7^1/_2$ hours. The use of the fixture was successful in removing the "bow" from the specimen blanks. The specimen blanks were numbered by their sequential order in the fixture during ageing. Metallographic samples were taken during the age hardening analysis. Rockwell C hardness measurements were also taken on each specimen blank after ageing.

A hard scale had developed on the surfaces of all of the specimen blanks during the annealing and ageing processes. The scale was partially removed by silica grit blasting. Microhardness measurements (100 gm Vickers) were taken to check for decarburization. No change in hardness was detected through the cross section of the samples.

The specimen blanks were machined into cantilever flat sheet fatigue specimens. The specimen geometry is illustrated in **figure 3-2.** on page 62. The machined fatigue specimens were not uniform in thickness and their top and bottom surfaces still had residual scale. The thickness of the fatigue specimen is critical in calculating the stress as a function of beam displacement. Also, the surfaces of each specimen must be clean for plating and identical to one another to reduce the scatter in the fatigue data. Several machining processes were evaluated; surface grinding, hand polishing, belt sanding, and lapping. Belt sanding and hand polishing were time consuming and did not improve thickness uniformity. Surface grinding the fatigue specimens was attempted, but proved to be too costly and too risky. The alternative to surface grinding was to

lap the fatigue specimens. The lapping process was successful in removing the residual scale and providing a uniform specimen thickness. As a result of lapping, the thickness measurements were within a tolerance of $\pm$ 5 microns ($\pm$ 0.0002 in).

Prior to plating, fatigue specimens were cleaned in acetone and engraved, once again. A plating maskant was applied to the displacement end (end with the screw holes) of each fatigue specimen to be plated. The purpose for the maskant was to prevent plating in the screw holes of the specimen and to provide more accurate displacement measurement during testing. Two coats of the maskant, Enplate® Stop-Off #1, were necessary to provide complete coverage.

After the maskant was applied, one sample was taken from each group to be plated for surface profile measurements. The surface profile measurements were done on a TENCOR INSTRUMENTS Alpha-Step 200 surface profilometer. Once the surface roughness measurements were taken, the fatigue bending specimens were packaged and shipped to the two Plating facilities.

Tensile tests and strain gauge tests were conducted using seven of the eighteen small narrow specimen blanks. These tests were conducted to determine the modulus of elasticity, 0.2% offset yield strength, ultimate tensile strength and percent elongation.

3.2   Metallography

Metallographic specimens of Custom 450® stainless steel were taken in several conditions as follows:

(1) Custom 450® stainless steel as received, unannealed cold rolled condition.

(2) Custom 450® stainless steel annealed at 1040°C (1905°F) for one hour followed by air quenching.

(3) Custom 450® stainless steel precipitation hardened at 525°C (977°F) for 4 hours.

(4) Custom 450® stainless steel precipitation hardened at 570°C (1058°F) for $7^1/_2$.hours

(5) Custom 450® stainless steel precipitation hardened at 525°C for 4 hours followed by an additional 4 hours at 570°C.

The metallographic specimens were taken from specimen blanks and mounted to view the crystallographic structures along the rolled direction (longitudinal axis of specimen blank). They were mounted in bakelite, ground and polished. Three different etchants were used to define the grain boundaries: (1) Vilella's reagent, (2) glyceregia, and (3) an etchant composed of the following:

10 ml nitric acid (HNO_3)

10 ml acetic acid

15 ml hydrochloric acid (HCL)

5-6 drops glycerol (wetting agent).

Custom 450® stainless steel proved to be very resistant to Vilella's reagent and glyceregia. The third etchant was very effective in providing grain boundary definition, requiring only 30 to 40 seconds of time to react with the stainless steel. As a result, all metallographic etching was done using the third etchant.

After etching, the metallographic specimens were viewed and photographed using an optical microscope. The grain sizes of Custom 450® stainless steel in conditions (2) through (5) are reported in accordance with ASTM Specification E112-85. The grain size of the material in the as-received condition was not reported do to the deformation caused by cold rolling.

Metallographic specimens were taken from the base of plated fatigue specimens after fracture to obtain plating composition and microhardness values. A TRACOR NORTHERN 5400 Energy Dispersive X-Ray Analyzer was used to determine the weight percent phosphorus of the electroless nickel-phosphorus coatings.

3.3 Hardness Tests

Rockwell C hardness measurements (HRC) were made on Custom 450® stainless steel in the as-received condition and at several time and temperature ageing treatments used for the age hardening analysis. In addition, Rockwell C measurements were taken on all specimen blanks after age hardening. All measurements were taken on the flat sides of the specimen blanks after removal of the scale, using a WILSON model 4JR Hardness Tester in accordance with ASTM Specification E18-84.

Rockwell D hardness measurements (HRD) were made on Custom 450® in the annealed condition. Rockwell B and C measurements were off scale due to material softening

Vickers microhardness tests were conducted on specimen blanks using a LECO DM-400 Microhardness Tester set at a 100 gm load (HV_{100}). These measurements were taken in the transverse plane of each specimen in accordance with ASTM Specification E92-82.. Specimen blank microhardness measurements were taken for the following age hardening profiles:

(1) aged 4 hours at 525°C (977°F)

(2) aged $7^{1}/_{2}$ hours at 570°C (1058°F)

(3) aged 4 hours at 525°C and 4 hours at 570°C

(4) aged 7 hours at 570°C.

Knoop Hardness tests were conducted on the electroless nickel coatings using a LECO DM-400 Microhardness Tester set at a 25 gm load (HK_{25}). Measurements were taken in both the longitudinal and transverse planes to maintain edge and thickness requirements specified in ASTM Specification E92-82.

3.4 Tensile Tests

Tensile tests were performed on five Custom 450® specimens in accordance with ASTM Specification E8-83. The five specimens received the following age hardening treatments:

Specimen #1	4 hours at 550°C (1022°F)
Specimen #2	4 hours at 550°C (1022°F)
Specimen #3	6 hours at 570°C (1058°F)
Specimen #4	4 hours at 570°C (1058°F)
Specimen #5	4 hours at 500°C (932°F)

The tests were conducted in air at room temperature using the Instron 4206 tensile testing machine. The crosshead velocity for these tests was 0.635mm/min (0.025 in/min). The strain rate for these 2.54 cm (one inch) gauge length specimens was therefore 4.17×10^{-4} seconds^{-1}. A 12.7 mm (0.5 in) clip-on extensometer was used in conjunction with the crosshead displacement to obtain accurate strain values. The geometry of the tensile specimens is presented in **figure 3-1** on page 60. The tensile specimens were surface ground to remove scale and provide uniform thickness. The thickness was uniform over the gage length to ±0.6% and ranged from 1.18 mm to 1.46 mm (0.0463 in to 0.0576 in). Prior to placing the tensile specimens in the machine grips, two scribe marks were placed 19.05 mm (0.75 in) apart along the gauge length to measure the percent elongation.

Only the longitudinal mechanical properties were investigated. Young's modulus, 0.2% offset yield strength, ultimate tensile strength, and percent elongation (over a gauge length of 19.05 mm or 0.75 in) are reported.
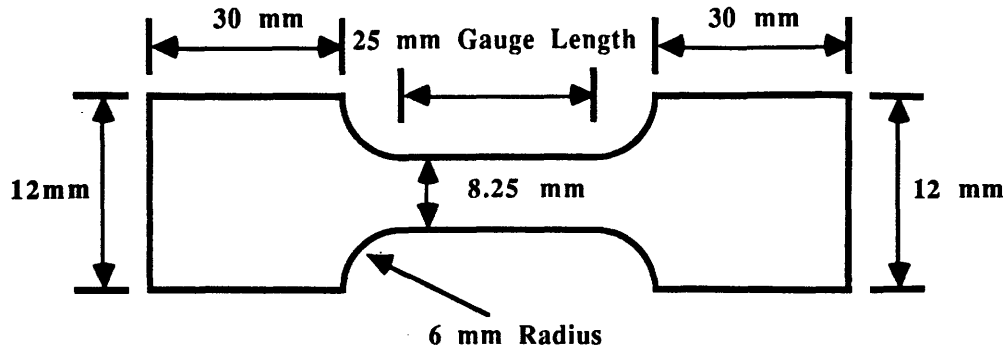
Figure 3-1. Tensile Test Specimen Geometry

3.5   Strain Gage Tests

Two strain gage tests were performed in air at room temperature using the Instron 4026

tensile test machine and a Measurements Group 2100 Strain Gauge Conditioner and Amplifier

System. A Micro-Measurements type EA-06-125AD-120 constantan strain gage was mounted in

the center of two tensile specimens using the Micro-Measurements M-Bond 200 adhesive system.

The tensile specimen design is illustrated in **figure 3-1**. Micro-Measurements surface preparation

and strain gage mounting procedures for stainless steel were carefully followed[109,110]. The

strain gages were operated within the range of 0 to 2500 microstrain, within the 3% strain limit

of the gages. The strain gage factor was 2.055 + 0.5% with a resistance of 120.0 + 0.15% ohms.

Both tests were conducted using the same shunt calibration, resulting in a simulated strain

($\mu\varepsilon_{cal}$) of 970 microstrain. An excitation voltage of 2.0 volts and a gain adjustment provided a

full scale reading of 10,000 microstrain (970 microstrain = 0.97 volts). Tensile specimen #6 was

wired in the internal dummy, quarter bridge configuration. Tensile specimen #7 was wired using

both specimens in the half bridge configuration. Each gage was mounted with three leads of the

same length.

The load on the tensile specimen was displayed on the Instron 4026 control panel in

millivolts, 1 volt equal to 6.895 MPa (1000 psi). A digital voltmeter provided direct strain

measurements in terms of millivolts, 1000 $\mu\varepsilon$/volt. The hydraulic ram was raised and lowered

manually. Movement was interrupted to record corresponding strain and load measurements. Young's modulus and stress versus strain plots are reported.

3.6   S-N   Fatigue   Tests

Low and high cycle fatigue S-N tests were conducted on electroless nickel coated custom 450® stainless steel. These tests were performed in air at room temperature using two Automation Industries Model CSS-40 constant displacement amplitude fatigue bending machines. The samples were tested at an R ratio of 0 (R=0) at a frequency of 1725 rpm or 28.75 Hz. A fatigue limit of 10^7 cycles was set for the testing of fatigue specimens. The fatigue specimens were designed in accordance with the machine manufacturer's specifications[111]. The derivation of stress in the fatigue specimen as a function of beam displacement is in **appendix A**. The fatigue specimens were tested as per ASTM Specification E739-80 and the procedures outlined in **appendix B**. The specimen geometry is presented in **figure 3-2** on page 62. Uniform specimen thickness was achieved by lapping the flat surfaces with 400 grit silicon carbide. Thickness uniformity was ±0.5% with specimen thicknesses ranging from 1.45 mm (0.057 in) to 1.56 mm (0.061 in).
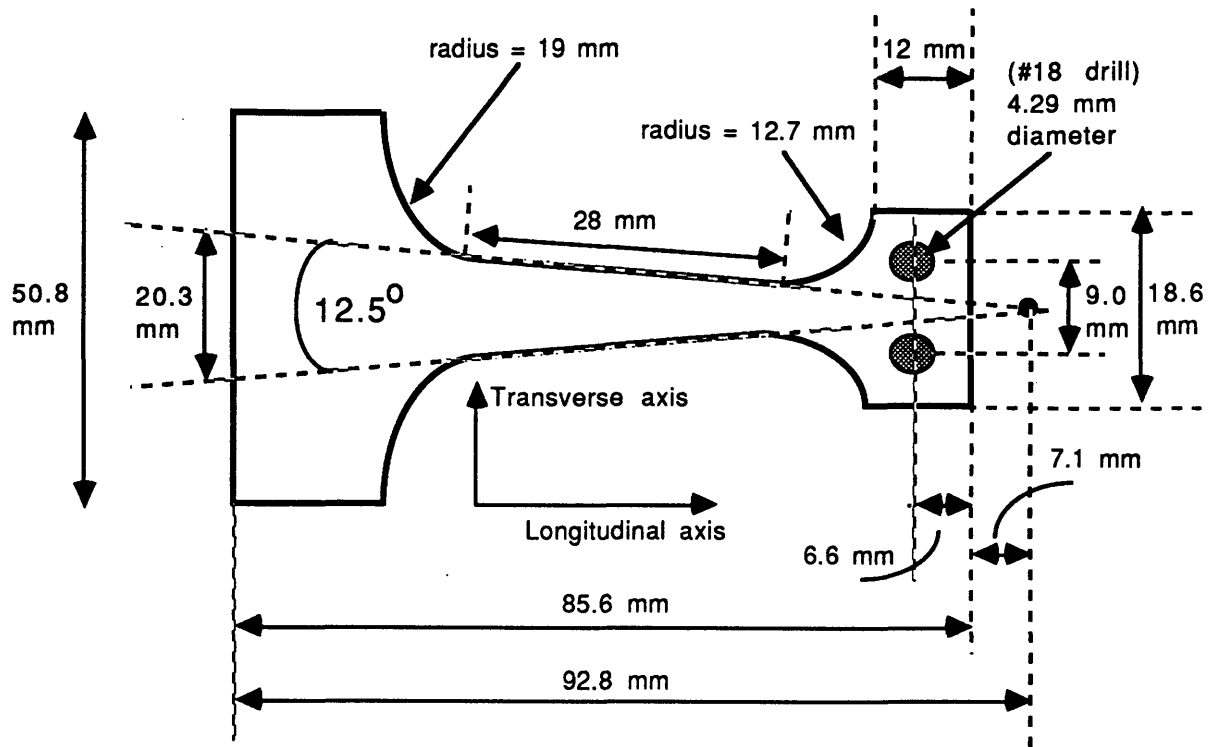
Figure 3-2. S-N Test Specimen Geometry

In order to evaluate the fatigue performance of the three different electroless nickel-phosphorus coatings, a control group of fourteen specimens without coatings was tested. All stress and displacement measurements ignore the coating thickness. Fatigue performance is simplified to a plot of the stress computed from the substrate (Custom 450® stainless steel) thickness and beam displacement to the number of cycles to failure.

Initially the coating does carry a load. However, the assumption that the coating carries little or no load is made, since it's thickness is less than two percent of the substrate's thickness. The brittleness of the coating resulting in surface cracking also helps to substantiate this assumption. Note: Young's modulus for the coating is approximately equal to that of the substrate (200 GPa).

The S-N test matrix used to determine the effect of several different electroless nickel-phosphorus coatings on the fatigue performance of Custom 450® stainless steel is shown in **Table 3-1**. The stress versus number of cycles to failure is reported.

Table 3-1. S-N Test Matrix

Order of Testing	Electroless nickel-phosphorus coatings	1 or 4 hr Heat Treatments hrs,°C (°F)	Number of specimens tested
#1	Baseline (uncoated)	none	11
#2	Lea-Ronal NICKELMERSE SPL (8 to 10% phosphorus)	1 hr,274 (525)	12
#3	Enthone Ni-422 (10 to 12% phosphorus)	4 hrs,191 (375)	10
#4	Enthone Ni-426 (1 to 3% phosphorus)	4 hrs,191 (375)	8
#5	Enthone Ni-426 (1 to 3% phosphorus)	4 hrs,191 (375) and 1 hr,366 (690)	11

The pretreatment, plating and post-treatment processes for each of the electroless nickel coatings is presented in **appendix C**.

3.7   Surface Roughness Tests

Surface roughness measurements were conducted to determine the surface roughness resulting from the electroless nickel coatings. One fatigue specimen was chosen from each group of coatings for surface measurements before and after plating. Each specimen chosen was cleaned prior to testing to remove surface debris. Surface profile measurements were conducted on a TENCOR INSTRUMENTS Alpha-Step 200 surface profilometer. Surface measurements were taken on one side of each specimen at three locations along the longitudinal axis as shown in

figure 3-3. The scan length was set at 2000 micrometers (0.079 in) with a horizontal range of 2000 micrometers. A 12.5 micrometer radius stylus traced the surface providing vertical height measurements (samples) every micrometer of travel for a total of 2000 samples in 40 seconds. The vertical scale was set to the kiloÅngstrom scale providing a resolution of 5 Ångstroms (5×10^{-10} meters). A thermal printer provided the reported output listing the following: (1) average profile height (Avg), (2) the arithmetic average roughness (RA) and (3) a graph of surface height (Y axis, KiloÅngstroms) versus surface distance (X axis, micrometers).
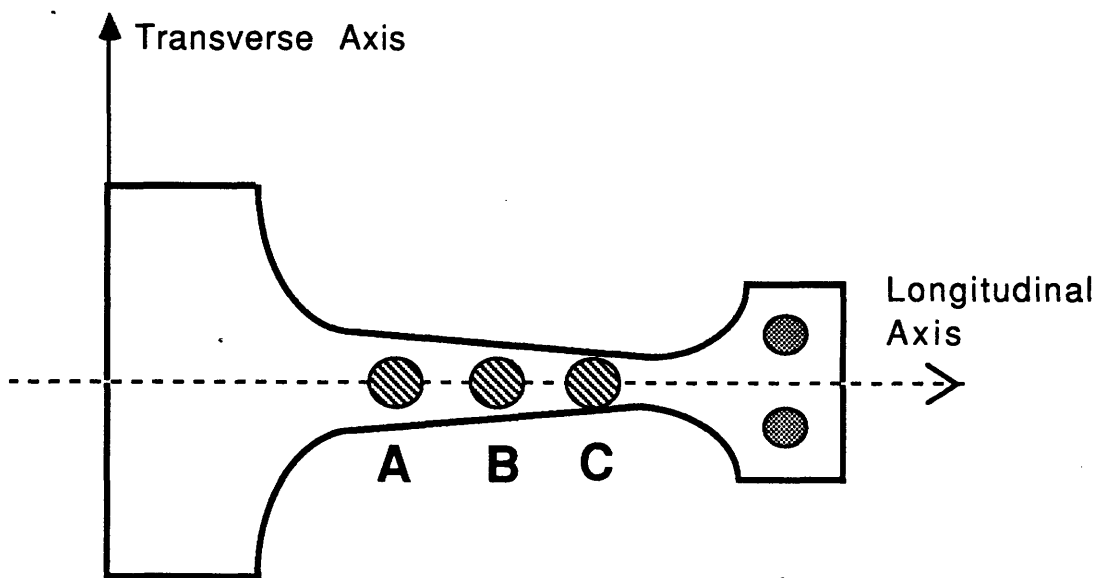
Figure 3-3. Surface Roughness Measurement Locations

4. RESULTS AND DISCUSSION

4.1   Metallography

The results of the metallographic investigation are presented to describe the structure of Custom 450® stainless steel in several conditions. The structure of Custom 450® stainless steel in the as-received condition is pictured in **figure 4-1** on page 65. The effects of cold rolling

can be seen by the compressed grain structure. The compressed grain structure (deformed grains) prohibited grain size measurements on the longitudinal plane. **Figure 4-1** also shows an inclusion in the center of the micrograph. Inclusions similar to these are dispersed throughout the Custom 450® stainless steel.
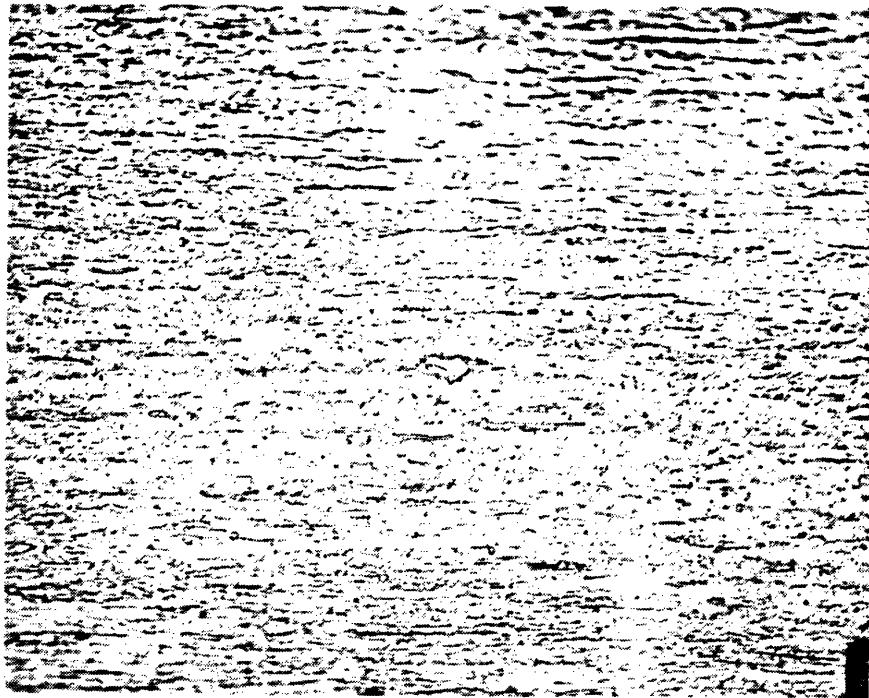
Figure 4-1. Custom 450® Stainless Steel in the
As-Received Condition. Longitudinal Cross-Section (500x).

The results of the grain size measurements for Custom 450® stainless steel after recrystallization are presented in **table 4-1** on page 66. Grain size measurements were made using the line intercept method in accordance to ASTM Specification E112-85. The circular grain area (A) was calculated using the average intercept width (L) in the expression[112]:

$$4L^2/\pi = A, \quad (L, mm) \qquad \text{(equation 4.1-1)}$$

Once annealed Custom 450® stainless steel did not experience any significant grain growth. The relatively low temperature and the precipitates which formed during the ageing heat treatments restricted grain growth.

Table 4-1. Custom 450® Stainless Steel Grain Sizes

Custom 450® Stainless Steel Condition	L (mm x10^{-3})	ASTM Grain Size	Grain Area(A) (mm^2 x 10^{-6})
Annealed at 1040°C (1905°F) one hour	14.6	8.90 (±0.08)	272
Aged at 525°C (977°F) for 4 hours	15.6	8.71 (±0.16)	311
Aged at 570°C (1058°F) for 7^1/$_2$ hours	16.7	8.50 (±0.43)	358
Aged at 525°C for 4 hours & 570°C for 4 hours	15.5	8.73 (±0.19)	306

The plating composition results obtained with the TRACOR NORTHERN 5400 Energy Dispersive X-Ray Analyzer are contained in **table 4-2**. Three measurements were taken through the cross-section of the plating to obtain an average value. Trace amounts of chromium and iron (less than 1%) were recorded on all interface and several center measurements. The trace amounts of iron and chromium are caused by the diffusion of the Custom 450® stainless steel into the plating.

Table 4-2. Electroless Nickel Coating Composition

Coating	Cross-section Location	Weight Percent (%) Nickel	Phosphorus
NICKELMERSE SPL	interface	91.92	8.08
	center	91.75	8.25
	surface	92.35	7.65
	AVERAGE	92	8
Enthone Ni-422	interface	90.24	9.76
	center	91.29	8.71
	surface	89.04	10.96
	AVERAGE	90.2	9.8
Enthone Ni-426	interface	98.30	1.70
	center	98.62	1.38
	surface	98.92	1.08
	AVERAGE	98.6	1.4

4.2 Hardness Test Data

Rockwell Hardness, Vickers microhardness and Knoop microhardness tests were conducted on Custom 450® stainless steel and/or the electroless nickel coatings as described in **Section 3.3**. The results of the Rockwell hardness tests are presented in **table 4-3**. **Table 4-3** shows the dramatic changes in hardness as a result of cold rolling, annealing and ageing. The values are realistic, predictable and similar to those reported by Carpenter Technologies.

Table 4-3 Custom 450® Stainless Steel Rockwell Hardness Results

Custom 450® Stainless Steel Condition	Rockwell Scale	Average Value (standard deviation)
As-Received (cold rolled, unannealed)	C	35.8 ($\pm$2.7)
Annealed at 1040°C (1905°F) one hour	D B (invalid) C (invalid)	45.0 ($\pm$1.0) 100 15
Aged at 525°C (977°F) for 4 hours	C	40.3 ($\pm$1.0)
Aged at 570°C (1058°F) for 71/2 hours	C	36.6 ($\pm$0.7)
Aged at 525°C for 4 hours & 570°C for 4 hours	C	37.4 ($\pm$0.5)
Aged at 560°C (1040°F) for 4 hours & 570°C for 4 hours	C	37.1 ($\pm$0.9)

The results of the Custom 450® stainless steel age hardening analysis are presented in **figure 4-2** on page 68. All Rockwell C data points represent average values. The difference in hardness values for the narrow tensile specimen blanks and the fatigue specimen blanks may be attributed to the slower cooling and heating rates of the fatigue specimen blanks bolted together by the fixture. When removed from the furnace, the narrow tensile specimen blanks experienced more rapid cooling to room temperature (2 minutes or less) than the fatigue specimen blanks (1.5 -

2 hours). These differences affect the nucleation rates of the Custom 450® stainless steel. In **figure 4-2,** observe the flatness of the narrow tensile specimen curve (4 hour) in the temperature range of 550°C to 570°C. The data points representing increased time (more than 4 hours) at a 570°C temperature indicate little change in hardness. The hardness of the fatigue specimen blanks was brought within AVCO LYCOMING specifications using a temperature of 570°C for $7^1/_2$ hours.
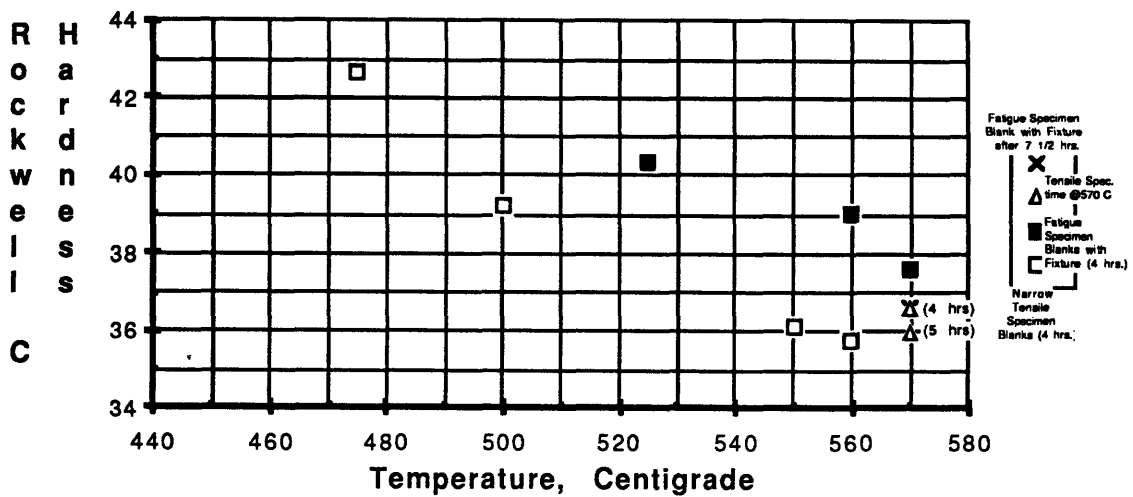

Figure 4-2. Custom 450® Stainless Steel Age Hardening Analysis
Rockwell C Hardness (HRC) versus Time at Temperature

The microhardness test results for Custom 450® stainless steel specimen blanks are provided in **Table 4-4.** The converted Vickers hardness values are similar to the measured Rockwell C hardness values.

Table 4-4. Custom 450® Stainless Steel Vickers (HV_{100}) Microhardness Values

Custom 450® Stainless Steel Condition	Vickers Hardness HV_{100}	Converted Rockwell C	Rockwell C Measured
Aged 4 hours at 525°C (977°F)	411.1 ($\pm$35)	41.9	40.3 ($\pm$1.0)
Aged 71/2 hours at 570°C (1058°F)	375.3 ($\pm$12)	38.2	36.6 ($\pm$0.7)
Aged 4 hours at 525°C & 4 hours at 570°C.	389.6 ($\pm$15)	39.7	37.4 ($\pm$0.5)
Aged 7 hours at 570°C (narrow tensile specimen blank)	386.2 ($\pm$10)	39.3	36.4 ($\pm$0.3)

The Knoop microhardness test results of the electroless nickel-phosphorus coatings are presented in **table 4-5**. The measured values are similar to values reported by the vendors of these coatings for the respective heat treatments. The converted Rockwell C approximation is based on an assumption of test load independence and the extrapolation of reported values for hard steels.

Table 4-5. Knoop Hardness (HK_{25}) of Electroless Nickel-Phosphorus Coatings

Electroless Nickel-Phosphorus Coating (Phosphorus Content %)	1 hr or 4 hrs Heat treatment Temperature	Knoop Hardness HK_{25}	Converted Rockwell C (approximate)
Lea-Ronal NICKELMERSE SPL (8 to 10%)	1 hr, 274°C (525°F)	942 ($\pm$28)	69
Enthone Ni-422 (10 to 12%)	4 hrs, 191°C (375°F)	928 ($\pm$53)	68
Enthone Ni-426 (1 to 3%)	4 hrs, 191°C (375°F)	865 ($\pm$76)	66
Enthone Ni-426 (1 to 3%)	4 hrs, 191°C & 1 hr, 366°C (690°F)	1021 ($\pm$45)	72

4.3   Tensile Test Data

The tensile tests were conducted as described in **section 3.4**. The results of the tensile tests are shown in **Table 4-6**. The first two values in **Table 4-6** are average values supplied by Carpenter Technologies[113]. The ultimate tensile strengths of Custom 450® stainless steel based on the Rockwell C hardness values for the various aging treatments are included. The ultimate tensile strengths converted from Rockwell C hardness values are approximate values. The two values agree within a six percent margin of error. The Stress versus Strain graphs and Young's Modulus (slope) values for the five test specimens are presented in **Appendix D**. The variation in Young's modulus for the five tests is attributed to specimen grip misalignment and sampling error.

Table 4-6. Tensile Test Results

Specimen Number	Custom 450® Condition (°C(°F), time)	0.2% Yield Strength MPa (ksi)	Ultimate Tensile Strength	Percent Elongation (%)	Young's Modulus GPa (ksi)	Rockwell C (Uts MPa) ((ksi))
Vendor Supplied	566 (1050), 4 hrs	1048 (152)	1103 (160)	20	200 (29x10³)	37 1145 (166)
Vendor Supplied	538 (1000), 4 hrs	1165 (169)	1193 (173)	17	200 (29x10³)	39 1220 (177)
#1	550 (1022), 4 hrs	1110 (161)	1158 (168)	17.3	221 (32x10³)	35.8 1103 (160)
#2	550 (1022), 4 hrs	1089 (158)	1161 (168)	21.3	159 (23x10³)	36.5 1127 (164)
#3	570 (1058), 6 hrs	997 (145)	1092 (158)	18.8	216 (31x10³)	37 1145 (166)
#4	570 (1058), 4 hrs	1014 (147)	1090 (158)	17.7	184 (27x10³)	36.6 1131 (164)
#5	500 (932), 4 hrs	1069 (155)	1154 (167)	14.1	167 (24x10³)	39 1220 (177)

4.4 Strain Gage Data

Two tensile test specimens were strain gaged to obtain more consistent values for the modulus of elasticity (E). The strain gage tests were conducted as described in **section 3.5**. The results of the two strain gage tests are shown in **Table 4-7**. Since the modulus of elasticity or Young' is related to the strength of the material's atomic bonds, the value of the modulus should not vary significantly with aging treatment The value of 200 GPa (29 x 10^3 ksi) was used to calculate the stress in the fatigue specimens. The stress versus strain graphs for the two strain gage tests are contained in **Appendix E..**

Table 4-7. Strain Gage Results

Specimen Number	Custom 450® Stainless Steel Condition	Modulus of Elasticity (E) · GPa	ksi
#6	Aged 4 hours at 500°C (932°F)	208.5	30.24x10^3
#7	Aged 5 hours at 570°C (1058°F)	193.4	28.05x10^3
average:		200.1	29.15x10^3
Vendor reported value:		200	29 x 10^3

4.5 Fatigue Test Data

Fatigue tests were conducted as described in **section 3.6**. The control group of fourteen uncoated specimens was tested first. S-N diagrams provided by Carpenter Technologies were used to select stress levels for testing. Specimen design provided constant stress (magnitude) along the tapered portion of the fatigue specimen. The magnitude of the stress was calculated as a function of beam displacement and specimen thickness using **equation 4.5-1**.

71

$$\sigma = \delta E t / L^2 \qquad \text{(equation 4.5-1)}$$

Where the parameters are:

σ surface stress along tapered portion of specimen
δ beam displacement
E Young's modulus for Custom 450® ss (200 GPa)
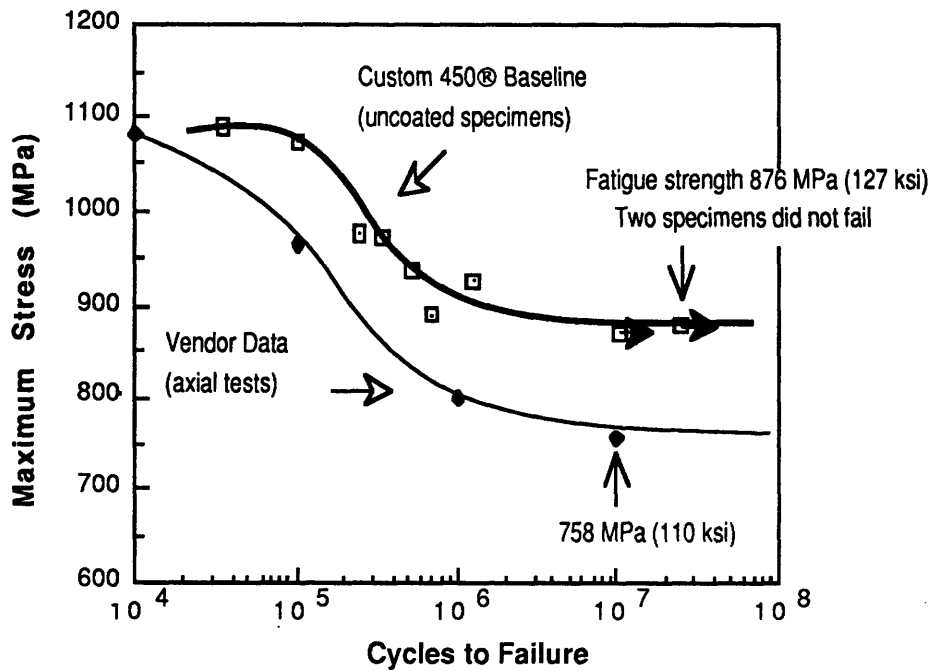t specimen thickness
L cantilever length of specimen

The beam displacement required to provide the selected stress was calculated based on the specimen thickness using **equation 4.5-1**. The resulting beam displacement was set in the fatigue testing machine and verified using a dial indicator as described in **Appendix B**. The fatigue machines were operated until specimen failure, at which time an electro-mechanical shut-off switch stopped the machine. A mechanical counter connected to the motor recorded the number of cycles to failure. The two fatigue testing machines recorded an additional 100 to 200 cycles from specimen failure to complete stop. This error is insignificant when the data is presented on the traditional log plot of the S-N curve.

The beam displacement set on the fatigue machine was accurate to ±25 micrometers (±0.001 in). Specimen dimensions were measured to an accuracy of ±12.5 micrometers (±0.0005 in). These measurements provide stress values with an error of less than ±1.28 percent within the elastic stress range of 345 MPa (50 ksi) to 1034 MPa (150 ksi).

The result of the fatigue tests for the baseline (control) group of fatigue specimens is presented in an S-N diagram and shown in **Figure 4-3** on page 73. The S-N diagrams in this section present the fatigue data to show the relationship between the maximum stress (σ_{max}) and cycles to failure. The arrows extending to the right of some of the data points indicates that the specimen *did not fail* at the specific stress to the tested number of cycles The maximum stress in the fatigue specimens was calculated using **equation 4.5-1**. The calculated stress was not allowed to exceed the the ultimate tensile strength of Custom 450® stainless steel (1090

MPa or 158 ksi) determined from the tensile tests. For comparison, constant life fatigue data for Custom 450® stainless steel bar heat treated for four hours at 566°C (1050°F) is shown[114]. The constant life data provided by Carpenter Technologies was obtained using longitudinal specimens with axial loading. Despite the differences in fatigue testing (bending versus axial testing), **figure 4-3** shows only a 13 percent difference between the two fatigue strengths at 10^7 cycles.

Fatigue 4-3. S-N Diagram for Custom 450® Stainless Steel at R=0.

Fatigue tests were conducted on the electroless nickel coatings using the specimen thickness prior to plating as the value for the stress calculation in **equation 4.5-1**. The results of the fatigue tests for the 30 micrometer thick (1.2 mil) LeaRoncel NICKELMERSE SPL coating are presented in **figure 4-4** on page 74 along with the baseline data.
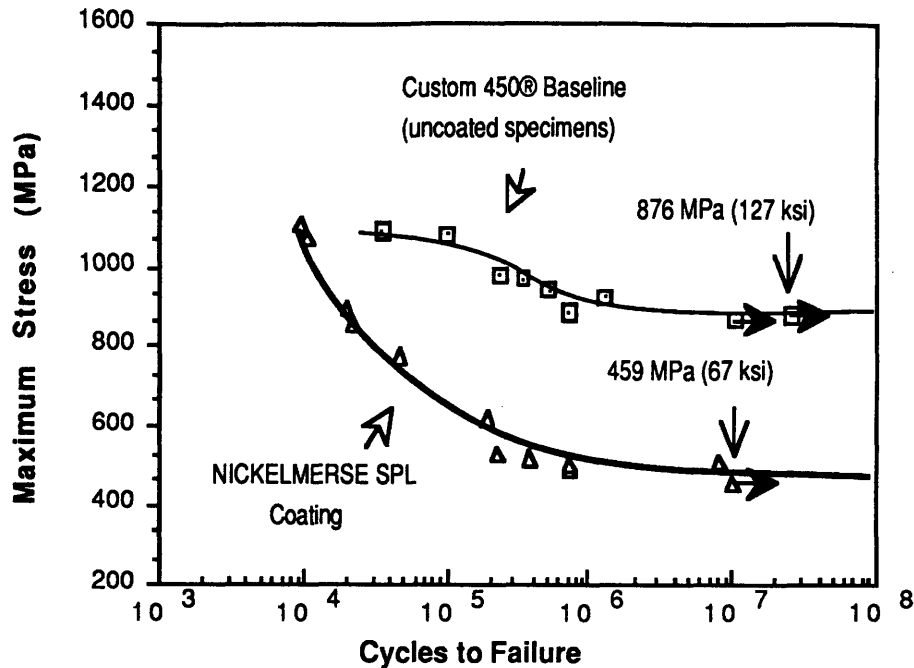
Figure 4-4. S-N Diagram for the 30 Micron (1.2 mil) Thick NICKELMERSE SPL Electroless Nickel Coating Tested at R=0.

The S-N data in **figure 4-4** shows a 42 percent reduction in fatigue strength for the NICKELMERSE SPL coating in the HCF region. In the LCF region of the NICKELMERSE SPL coating curve, the cycles to failure for a given stress (1090 MPa (158 ksi)) were reduced by more than a factor of 10.

The results from the fatigue tests conducted on the 25 micrometer thick Enthone Ni-422 coating are presented in **figure 4-5** on page 75. The baseline fatigue data is also presented for comparison.
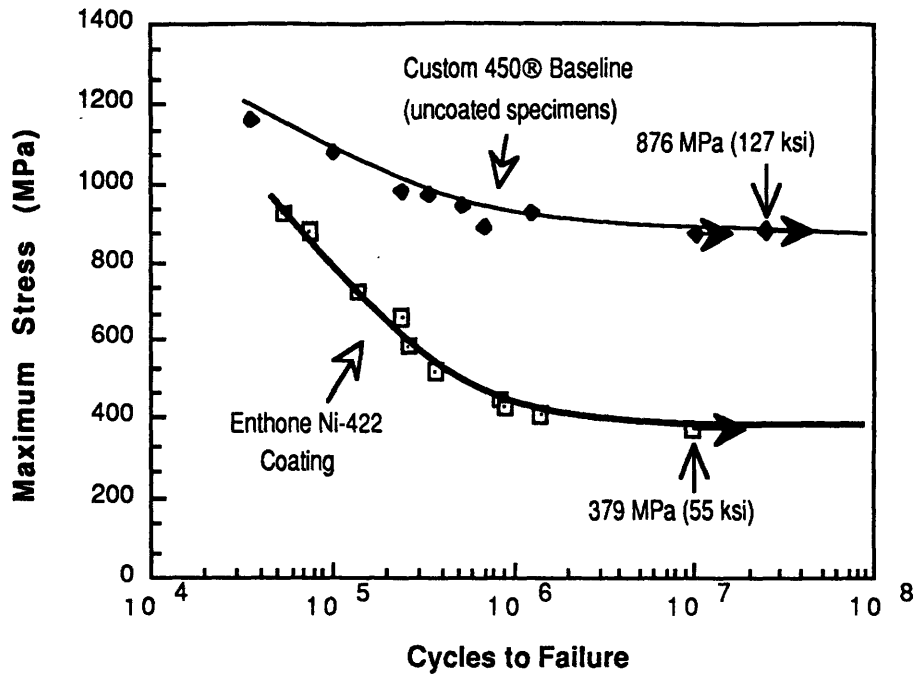
Figure 4-5. S-N Diagram for the 25 Micron (1.0 mil) Thick Enthone Ni-422 Electroless Nickel Coating Tested at R=0

The S-N data in **figure 4-5** shows a 57 percent reduction in fatigue strength for the Enthone Ni-422 coating in the HCF region. In the LCF region of the Enthone Ni-422 coating curve, the cycles to failure for a given stress were reduced by more than a factor 10, similar to the NICKELMERSE SPL coating.

The results of the fatigue tests for the 25 micrometer (1.0 mil) thick Enthone Ni-426 electroless nickel coating are presented in **figure 4-6** on page 76. The data for both heat treatments is provided along with the baseline data.
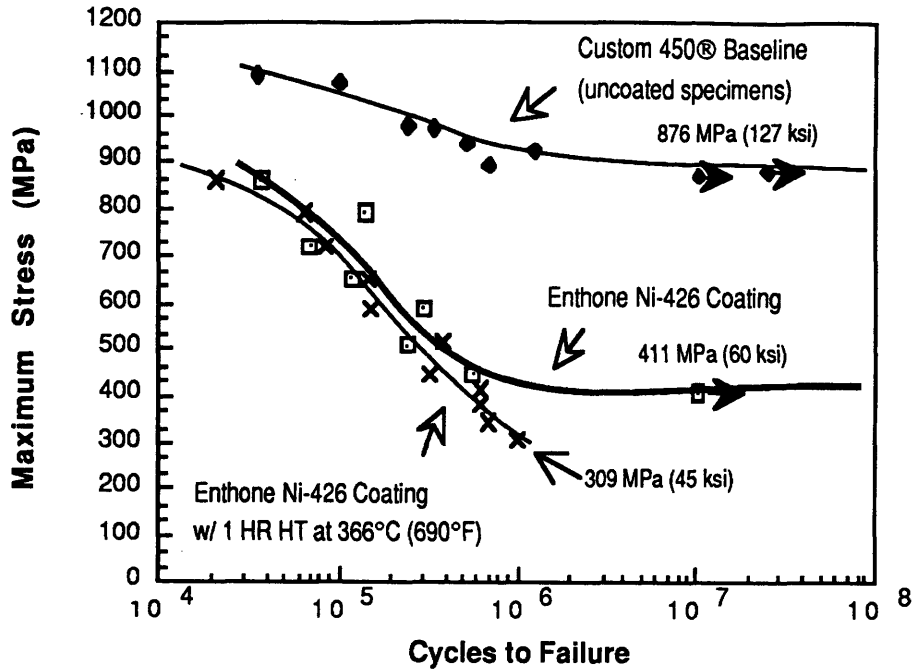
Figure 4-6. S-N Diagram for the 25 Micron (1.0 mil) Thick
Enthone Ni-426 Coatings Tested at R=0

The S-N diagram in **figure 4-6** shows a reduction of 53 percent in fatigue strength for the
Enthone Ni-426 coating and an additional 12 percent reduction in fatigue strength for the same
coating subjected to an additional heat treatment of one hour at 366°C (690°F). . The Enthone
Ni-426 coatings reduce the fatigue performance of Custom 450® stainless steel, in a similar
manner as the other electroless nickel coatings tested.

A comparison of the fatigue performance of the four electroless nickel coating can be
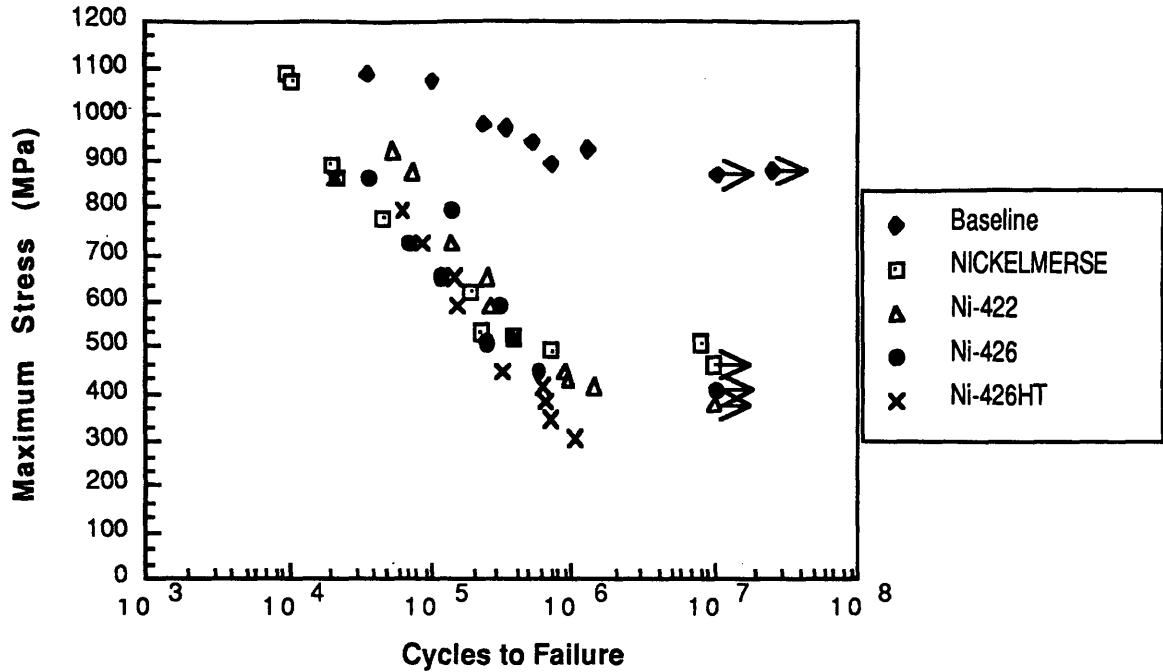made by observing the overlay of S-N data in **figure 4-7** on page 77.

Figure 4-7. S-N Diagram of Electroless Nickel Coatings Tested at R=0

The S-N data in **figure 4-7** shows the reduction of fatigue performance resulting from electroless nickel coatings. The fatigue performance of the low phosphorus Enthone Ni-426 coating is reduced even further by heat treatment. The fatigue strengths of the NICKELMERSE SPL (459 MPa), Ni-422 (379 MPa) and Ni-426 (411 MPa without additional heat treatment) coatings are within a range of 80 MPa (12 ksi). If the data is extrapolated in the LCF region, the electroless nickel coating curves would intersect the baseline curve in the 10^3 cycles to failure region. The NICKELMERSE SPL coating with an 8 to 10 percent phosphorus content provided the highest fatigue strength (459 MPa or 67 ksi), however the heat treatment of one hour at 274°C (525°F) for this coating was different from the other coatings. The glass bead blasting of the NICKELMERSE SPL coated specimens during pretreatment may have lead to the overall improvement of the coating.

4.6   Fractographic Analysis

The fracture surfaces of the fatigue specimens were investigated using optical microscopes and the scanning electron microscope (SEM). All fracture surfaces occurred in the tapered portion of the fatigue specimen as designed. Two representative drawings of typical fracture surfaces are provided in **figure 4-8** on page 79. All fractures were initiated on the lower tension surfaces for both coated.and uncoated fatigue specimens. The lower left and right corners of the fracture surfaces were very smooth, typical of early crack propagation. Observing these areas with the SEM, provided little information since the fatigue striations were so small or obscured by fretting. The lower cross-section of the plating (in tension) was also very smooth. Crack initiation occurred in the lower corners in all but two specimens. The crack initiation sites for those two specimens occurred along the lower tension surfaces.

In most cases, crack initiation occurred in both lower corners and crack propagation proceeded up and toward the center until fast fracture (**figure 4-8 A**). The upper surface (including the upper plating cross-section) contained rough jagged features corresponding to shear lips associated with fast fracture. The later stages of crack propagation towards the center of the cross-section showed out-of-plane crack propagation features called *rivers*. The rivers have a rougher texture than the early crack propagation regions. They are the tell-tale features formed by out-of-plane crack propagation, aligned perpendicularly to the crack front as shown in **figure 4-8 (A) & (B)**.

The lower coating surface, in tension, shows widespread cracking in all the coatings. The cracking is due to the brittleness of the coating. The upper surfaces in compression show no cracking except immediately adjacent to the fracture. These upper surface cracks are parallel to the fracture and are the result of reverse yielding in the plating due to plastic deformation. In many instances, as the neutral axis was shifted upwards, secondary cracks would propagate down from the upper surface until fast fracture. These secondary crack regions were
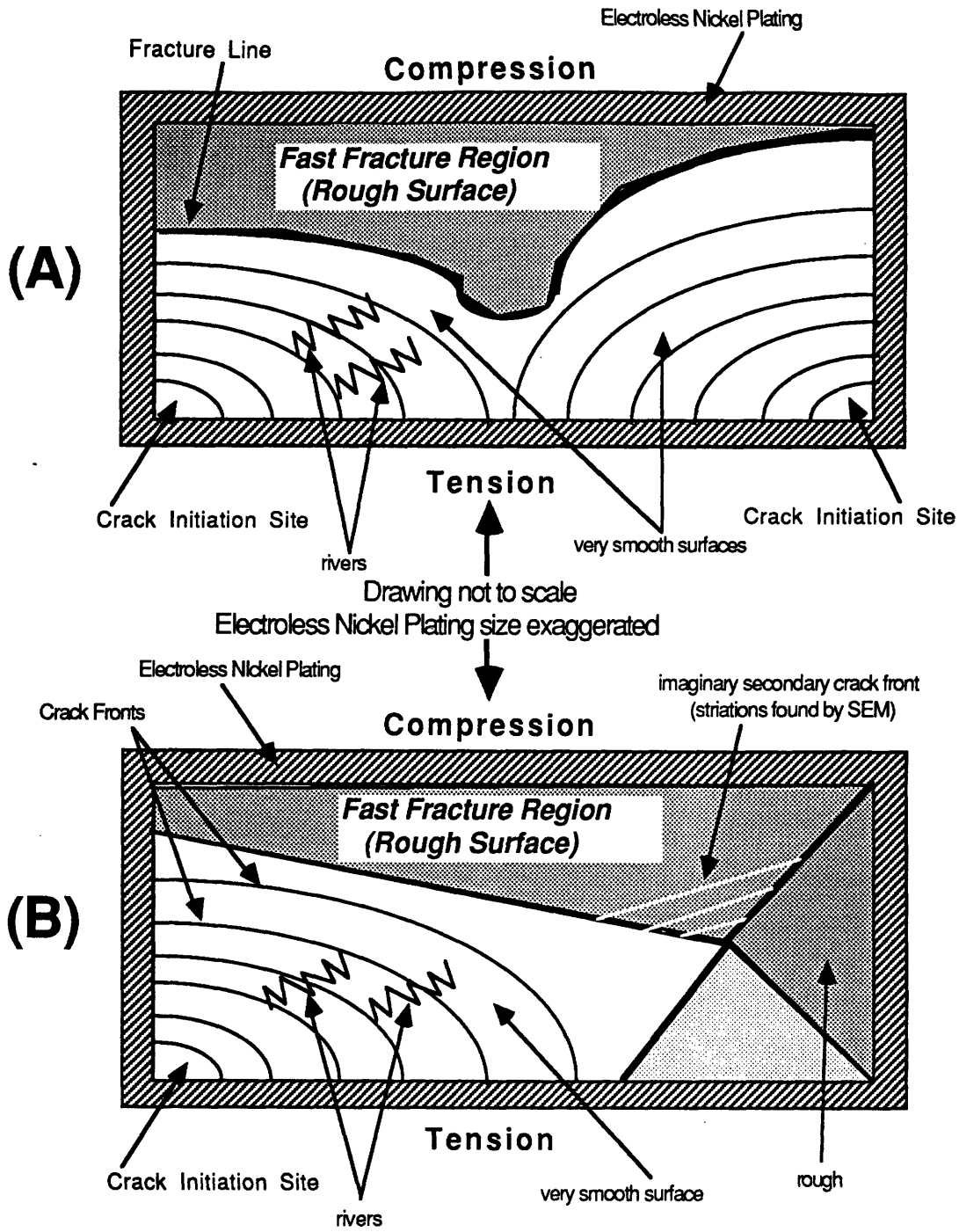
Figure 4-8. Typical Fracture Surface

investigated under the SEM and fatigue striations were observed. Representative photographs of the fracture surface features described in this section are provided in **Appendix F**.

4.7   Surface Roughness Data

Surface roughness measurements were taken on several Custom 450® stainless steel fatigue specimens both before and after plating as described in **section 3.7**. The results of these measurements are presented in **table 4-8** on page 81. The measurements were taken with reference to the locations described in **figure 3-3** on page 65. The two parameters, Total Indicator Runout (TIR) and Surface Roughness (RA), are defined as follows:

Total Indicator Runout is the difference between the maximum and the minimum profile heights. It is computed for each 2000 micrometer scan and reported in kiloAngstroms.

Surface Roughness is determined using the graphical centerline method according to the ANSI Standard B46.1-1978, Appendix C.3.2.1. Each profile height measurement is relative to the first point of the scan.

The value computed for the surface roughness (RA) can be used directly, without further computation[115]. In **table 4-8**, the surface roughness measurements are reported in micrometers. The graphical outputs obtained from each of the surface profilometer scans is presented in **Appendix G** for comparison.

Table 4-8. Surface Profile Measurements

Specimen Number	Location	Condition (coating)	Surface Roughness (RA) (micrometers)	Total Indicator Runout (TIR) (micrometers)
2	A	C450® uncoated	0.235	2.175
2	A	30 microns NICKELMERSE SPL	1.025	6.732
2	B	C450® uncoated	0.214	1.730
2	B	30 microns NICKELMERSE SPL	0.713	4.383
2	C	C450® uncoated	0.221	2.493
2	C	30 microns NICKELMERSE SPL	0.950	6.419
5	A	C450® uncoated	0.254	1.866
5	A	25 microns Enthone Ni-426	.241	1.864
5	B	C450® uncoated	0.267	2.337
5	B	25 microns Enthone Ni-426	0.304	2.227
5	C	C450® uncoated	0.282	2.433
5	C	25 microns Enthone Ni-426	0.220	1.627
7	A	C450® uncoated	0.237	1.757
7	A	25 microns Enthone Ni-426	0.303	2.349
7	B	C450® uncoated	0.218	1.836
7	B	25 microns Enthone Ni-426	0.283	2.391
7	C	C450® uncoated	0.224	3.018
7	C	25 microns Enthone Ni-426	0.351	2.805
8	A	C450® uncoated	0.304	2.875
8	A	25 microns Enthone Ni-422	0.227	2.772
8	B	C450® uncoated	0.299	2.161
8	B	25 microns Enthone Ni-422	0.299	2.578
8	C	C450® uncoated	0.439	3.218
8	C	25 microns Enthone Ni-422	0.362	2.634

The surface roughness analysis must consider the errors associated with the difficulty in duplicating the surface scan. No marks were made on the surface of the specimen to re-trace the original scan. The surface roughness measurements reported represent approximate values

obtained after 3 scans in the areas described in **figure 3-3**. Scans were not accepted if surface scratches or debris were encountered during the scan. Therefore, for these reasons, only a qualitative comparison of the surface roughnesses can be made.

The NICKELMERSE SPL coating increased the surface roughness by a factor of from 3 to 5. The values for both TIR and RA are at least three times larger. The NICKELMERSE SPL coating had a bright nickel appearance. The change in surface roughness is a result of both the pretreatment and plating processes, which included glass bead blasting at 30 psi.

The Enthone Ni-422 coating did not significantly change the surface roughness of the specimens tested. The RA and TIR values were very close at all three locations. The Enthone Ni-422 coating produced a nickel-colored mat finish similar in appearance to the texture of the uncoated specimens. Abrasion marks, originating from specimen thickness measurements taken before plating, were reproduced on the coatings. No definite leveling action was observed.

The Enthone Ni-426 coatings did not change the surface roughness of the specimens tested. The RA and TIIR values for coated and uncoated specimens were also too close and inconsistent. The Enthone Ni-426 coatings produced a nickel-colored matfinish similar to the uncoated specimens, but slightly brighter in appearance than the Enthone Ni-422 coating.

5. CONCLUSIONS

1. The mechanical properties of a wrought Custom 450® stainless steel alloy were investigated at room temperature. The fatigue performance was measured in reverse bending (R=0) for a fatigue life of up to 10^7 cycles at a frequency of 29 Hz.

2. Three different electroless nickel-phosphorus coatings with different heat treatments were reviewed as a means to improve the wear and erosion resistance of the stainless steel alloy. The electroless nickel coatings evaluated were:

(a) 30 micron (1.2 mil) thick Lea-Ronal NICKELMERSE SPL electroless nickel heat treated for one hour at 274°C (525°F). The coating phosphorus content was measured to be 8 weight percent.

(b) 25 micron (1.0 mil) thick Enthone Ni-422 electroless nickel heat treated for four hours at 191°C (375°F). The coating phosphorus content was measured to be 9.8 weight percent.

(c) 25 micron (1.0 mil) thick Enthone Ni-426 electroless nickel heat treated for four hours at 191°C (375°F). The coating phosphorus content was measured to be 1.4 weight percent.

(d) 25 micron (1.0 mil) thick Enthone Ni-426 electroless nickel heat treated for four hours at 191°C (375°F) followed by an additional one hour heat treatment at 366°C (690°F).

3. Fatigue tests were performed on electroless nickel coated specimens in the same manner as those performed for the wrought stainless steel alloy. Fatigue data was analyzed using traditional S-N diagrams to determine fatigue strengths at 10^7 cycles.

4. The electroless nickel coatings reduced the fatigue strength of Custom 450® stainless steel by 48 to 65 percent. The fatigue strengths of the four coatings are given in **table 6-1**.

Table 6-1. Fatigue Strengths (10^7 cycles) of Electroless Nickel Coatings

Nature of Samples	Fatigue Strength Limit	
	MPa (ksi)	compared with C450®ss, %
C450® stainless steel	876 (127)	100
LeaRonal NICKELMERSE SPL	459 (67)	52
Enthone Ni-422	379 (55)	43
Enthone Ni-426	411 (60)	47
Enthone Ni-426 w/HT	309 (45)	35

5. The detrimental effects of electroless nickel-phosphorus coatings upon the fatigue performance of Custom 450® stainless steel are related to the onset of crack initiation. The electroless nickel coatings act as *crack starters*, shifting the S-N curves down and to the left of the baseline curve. Widespread surface cracking was observed along the tension surface of the fatigue specimens. Cracking of the coating was caused by the brittleness of the coating. The cracking may also be due to the volumetric shrinkage of the coating during heat treatment. The presence of cracks (defects) in the coatings act as stress concentration sites accelerating the fatigue crack initiation stage of the fatigue failure process. The cracking reduces the coatings ability to carry a load in tension. The high hardness of the coating does not translate into high strength due to the presence of cracks and impurities in the coating.

6. The hardness of the low phosphorus Enthone Ni-426 coating was increased from 865 to 1021 HK_{25} by heat treatment for one hour at 366°C. The heat treatment resulted in an additional 12 percent reduction in fatigue strength. The reduction in fatigue strength as a result of heat treatment is caused by the increased brittleness of the coating

7. The beneficial effects of the compressive residual stresses reported in the Enthone Ni-422 and Ni-426 coatings <u>do not improve</u> the fatigue performance of the Custom 450® stainless steel alloy. However, the beneficial effects of the compressive residual stresses resulting from glass bead blasting may have improved the fatigue performance of the NICKELMERSE SPL coated specimens.

8. The electroless nickel coatings do not improve the surface roughness of the substrate. The effects of pretreatment (including glass bead blasting) and plating on the Lea-Ronal NICKELMERSE SPL coating increased the surface roughness by a factor of 3. However, the NICKELMERSE SPL coating did demonstrate a higher fatigue strength than the other coatings tested. Therefore, the coatings surface roughness did not have any significant effect on the fatigue performance of the coating. The surface roughness of the Enthone Ni-426 and Ni-422

coatings were comparable to the surface roughnesses of the Custom 450® stainless steel alloy. No significant leveling action was observed to reduce the thickness of the boundary layer of air flow through the compressor.

9. Electroless nickel-phosphorus coatings will reduce the fatigue performance of the LYCOMING LTS 101-750-B2 compressor rotor.

6. RECOMMENDATIONS

1. Electroless nickel-phosphorus coatings can significantly improve the wear and corrosion resistance of many materials. However their unfavorable effect on the fatigue strength of high strength stainless steels, like Custom 450®, must seriously be considered during the design process. The mean stress calculated for the blade root of the LTS-750-B2 compressor rotor, during normal operations, is 361 MPa (52 ksi). This mean stress places a coated compressor rotor in the HCF region (10^7 cycles) of the S-N diagram. An uncoated compressor rotor operates at a stress level 58% below the fatigue strength of Custom 450® stainless steel. An electroless nickel coated compressor would operate at the same stress level but near the lower fatigue strength level of the coated stainless steel. The stress levels resulting from engine overspeed are approximately 707 MPa (103 ksi), definitely placing a coated compressor rotor in the LCF region of the S-N diagram. An uncoated rotor always operates well below the fatigue strength of Custom 450® stainless steel! The overspeed stresses experienced by an electroless nickel coated compressor rotor may be sufficient to cause surface cracking, thereby initiating a fatigue failure and also aggravating the corrosion problem.

· The S-N diagrams can not be used to predict failure or fatigue life without a more accurate model of the engine load history. However, S-N diagrams can be used to show whether an overall improvement in fatigue performance can or can not be expected. The use of electroless nickel-phosphorus coatings will reduce the fatigue performance of the Custom 450® stainless steel alloy. The extent of the degradation is not known without more extensive testing. The use

of electroless nickel coatings on dynamic machinery must be closely investigated, including full scale testing before implementation.

2. The Lea-Ronal NICKELMERSE SPL coating with a fatigue strength of 459 MPa (67 ksi) does provide a 21% margin of safety for normal operations. Continued research is recommended for this coating based on the coatings superior fatigue performance (relative to coatings tested) and it's corrosion and wear resistance. Testing should also be done with the high phosphorus coatings (12% phosphorus) due to their superior corrosion resistance and reported high strength. The Enthone Ni-422 coating tested contained only 9.8 percent phosphorus. Testing of these coatings should be done using the same pretreatment processes and coating thicknesses to eliminate the difficulty of separating cause factors. This was particularly true with the NICKELMERSE SPL coating, which was 20% thicker than the other coatings, incorporated a glass bead blasting sequence during the pretreatment process.and was subjected to a different heat treatment. The compressive residual stresses resulting from glass bead blasting may have contributed to the higher fatigue strength of the NICKELMERSE SPL coating. The amount of cracking observed on the tension side of this coating was less than that observed for the other coatings.

2. The corrosion resistance of the low phosphorus Enthone Ni-426 coating is poor in a saltwater environment. This fact, coupled with it's low fatigue strength precludes it's use as a satisfactory coating.

3. The Electroless nickel-phosphorus coatings tested in this investigation did not improve the surface roughness of the test articles. However, the Enthone Ni-422 and Ni-426 coatings did replicate the surface profiles of the substrate. The erosion and corrosion resistance of electroless nickel coatings can be used to prolong engine life and maintain peak engine efficiency, however the stress levels of the coated machinery must be low enough to prevent cracking of the coating.

Appendix A

The Derivation of the Surface Stress
In a Cantilever Flat Sheet Fatigue Specimen
as a Function of Specimen Thickness and Beam Displacement

The calculation of the stress on the surface of the cantilever flat sheet fatigue specimen is as follows:

$$\sigma_x = \frac{6\,P\,L}{A\,t^2} \quad \text{(equation A-1)}$$

$$\sigma_x = \frac{E\,t\,\delta}{L^2} \quad \text{(equation A-2)}$$
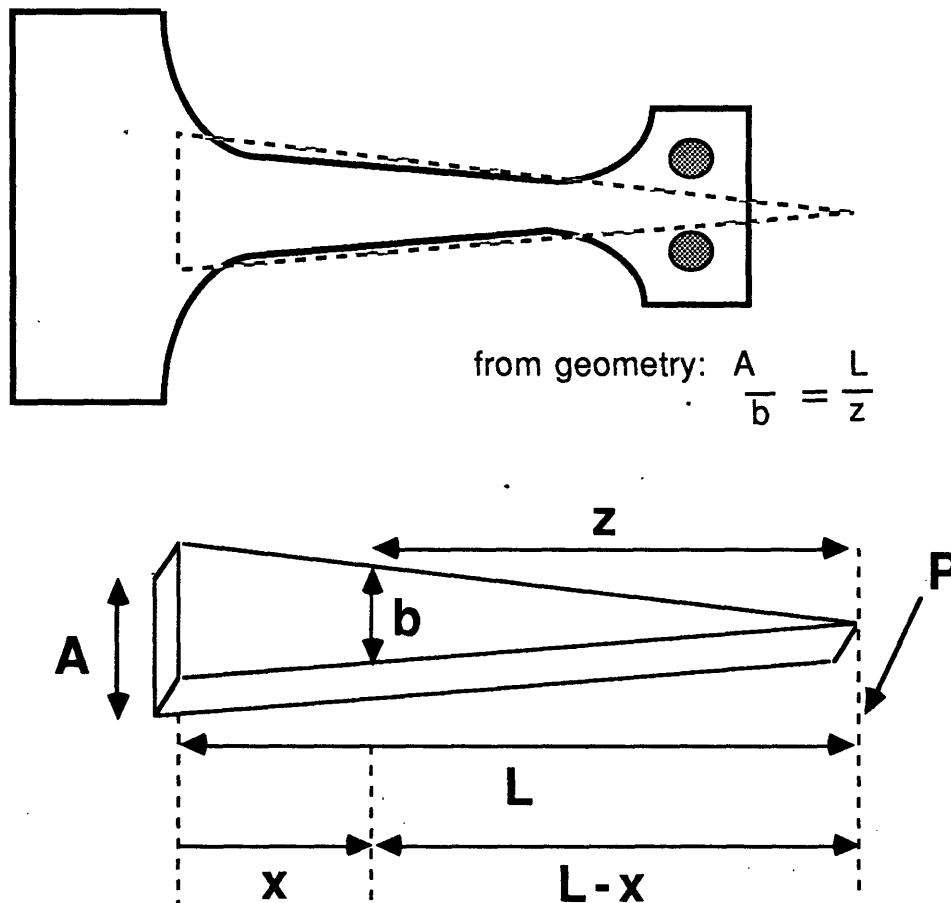
The derivation of **equation A-1** will refer to **figure A-1**.

from geometry: $\dfrac{A}{b} = \dfrac{L}{z}$

Figure A-1. Fatigue Specimen Design

We know from geometry (similar triangles):

$$\frac{A}{b} = \frac{L}{z}$$

Simplifying to solve for **b** yields:

$$b = \frac{A\,z}{L}$$

Using a right hand cartesian coordinate system in **figure A-1**, we see:

$$z = L - x$$

so that:

$$b = \frac{A\ (L-x)}{L} \qquad \text{(equation A-3)}$$

From beam theory, the moment of inertia for a rectangular cross-section is:

$$I = \frac{b\ t^3}{12}$$

Substituting for **b** using **equation A-3** yields:

$$I = \frac{A\ (L-x)\ t^3}{12\ L} \qquad \text{(equation A-4)}$$

Also from beam theory, for a point load **P**:

$$M = P(L-x) \qquad \text{(equation A-5)}$$

and

$$\sigma_x = \frac{M\ t/2}{I} \qquad \text{(equation A-6)}$$

Substituting **equation A-5** and **equation A-4** into **equation A-6** results in **equation A-1**.

$$\sigma_x = \frac{6\ P\ L}{A\ t^2} \qquad \text{(equation A-1)}$$

The **L/A** term in **equation A-1** is a constant in the specimen design. This shows that the stress (σ_x) at thé surface of the fatigue specimen has a constant magnitude along the tapered portion of the specimen (dashed triangle of specimen in **figure A-1**).

In order to derive fundamental **equation A-2**, review of basic geometry will be shown in **figure A-2** on page 90.
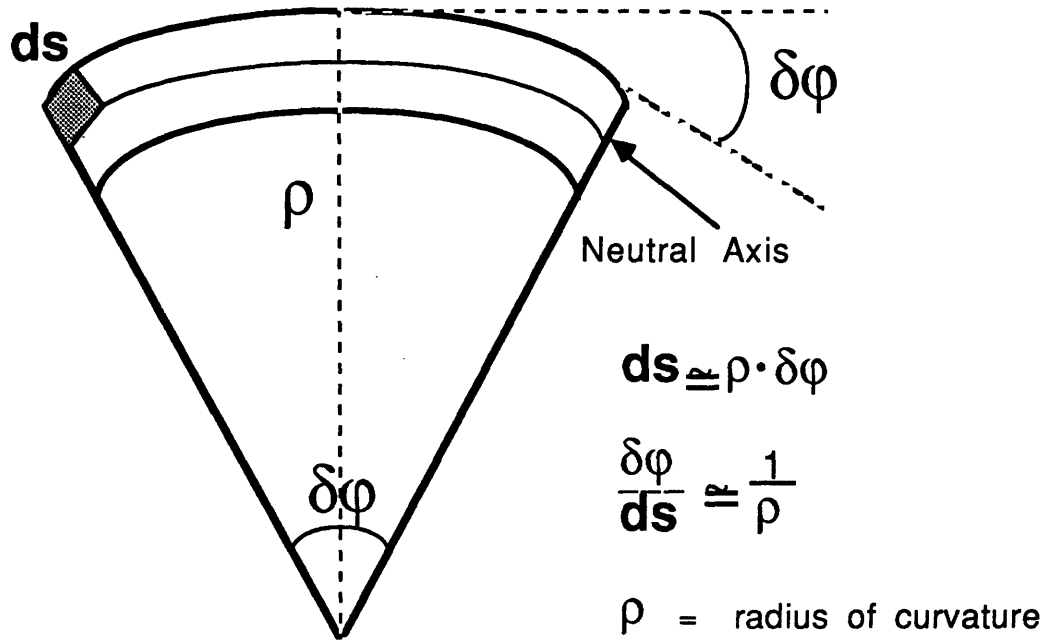
Figure A-2. Beam Curvature

If the cantilever beam behaves in an elastic manner, the elastic strain in the beam is :

$$\varepsilon_x = \frac{\sigma_x}{E} = \frac{M\,t/2}{EI} \qquad \text{(equation A-7)}$$

From beam theory, we also have:

$$\frac{1}{\rho} = \frac{d\phi}{ds} = \frac{M}{EI} \qquad \text{(equation A-8)}$$

where:

$$\frac{d\phi}{ds} = \frac{dv^2}{dx^2} \qquad \text{(equation A-9)}$$
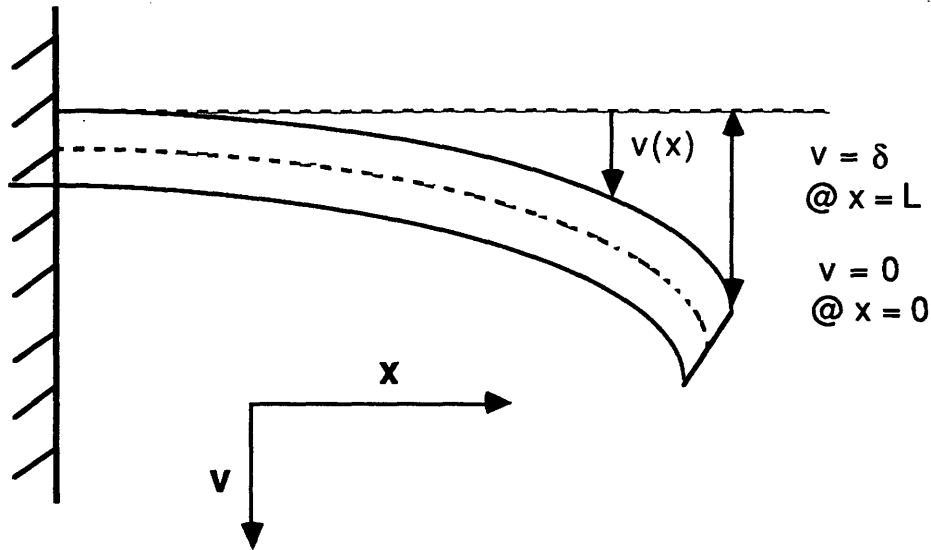
Figure A-3. Beam Displacement

Referring to to **figure A-3**, and substituting **equation A-4** and **equation A-5** into **equation A-8** and **equation A-9**, we get:

$$\frac{dv^2}{dx^2} = \frac{d\phi}{ds} = \frac{M}{EI} = \frac{P(L\text{-}x)}{E\,t^3\,A\,\frac{(L\text{-}x)}{12\,L}} = \frac{12\,PL}{E\,t^3\,A}$$

We must integrate *twice* to obtain v(x), the vertical displacement.

$$\frac{dv}{dx} = \int \frac{12\,P\,L}{E\,t^3}\,dx$$

which becomes:

$$\frac{dv}{dx} = \frac{12\,P\,L}{E\,t^3\,A}\,x + C_1$$

The **boundary conditions** at x=0 are: $x = 0$, $\frac{dv}{dx} = 0$

Using these boundary conditions, $C_1 = 0$.

Now, we must integrate once more:

$$v(x) = \int dv = \int \frac{12\,P\,L}{E\,t^3\,A}\,x\,dx$$

which yields:

$$v(x) = \frac{12\,P\,L}{2\,E\,t^3\,A}\,x^2 + C_2$$

The **boundary conditions** at x=0 are: $x = 0$, $v(0) = 0$

Using these boundary conditions $C_2 = 0$.

Therefore at $x = L$, $v(L) = \delta$, so that:

$$\delta = \frac{6\,P\,L^3}{E\,t^3\,A} \qquad \text{(equation A-10)}$$

Now, if we compare the equation for the stress in the beam, **equation A-1**, we see some similarities!

$$\sigma_x = \frac{6\,P\,L}{A\,t^2} \qquad \text{(equation A-1)}$$

If we take the ratio of the two quantities then we get:

$$\frac{\delta}{\sigma_x} = \frac{L^2}{E\,t} \qquad \text{(equation A-11)}$$

Equation·A-11 can be written to solve for the stress.

$$\sigma_x = \frac{\delta\,E\,t}{L^2} \qquad \text{(equation A-2)}$$

Again, observe that the stress is independent of the constant **L/A**. During this investigation, specimen design allowed the term $\frac{E}{L^2}$ to remain constant, simplifying **equation A-1** to:

$$\sigma_x = \delta\,t\,(K)$$

$$\text{where: } K = \frac{E}{L^2}$$

The value used for Young's modulus was: **E = 200 GPa (29×10^6 psi).**

The value used for L^2 was: **$L^2 = 54.9 \times 10^{-4}$ m^2 or 54.9 cm^2 (8.51 in^2).**

Appendix B

Setup Procedure for the Automation Industries Fatigue Testing Machine

The Automation Industries Fatigue Testing Machine is used to conduct fatigue tests on cantilever flat sheet fatigue specimens. The machine is designed to work with specimens which have a total length of 3.375 inches (85.7 mm). Specimen design is described in Appendix A. The following equipment is required to setup the machine:

1) 3/16 inch Allen wrench
2) 9/64 inch Allen wrench
3) 1/16 inch Allen wrench
4) 80-90W machine oil
5) 1.0 or 2.0 inch dial indicator with mounting supports
6) Crescent wrench
7) rags to clean excess oil

NOTE** The roller bearings for the swivel pin support and the rotating arm should be checked periodically for corrosion and excess play. The bearings are removed and installed with the use of an arbor press, since they are machined for a press fit. The part numbers and quantities are as follows:

1) Swivel pin support bearing -   Torrington B-57   Quantity 2
2) Rotating arm support bearing: New Departure 88500 Quantity 1

The fatigue bending machine is a *simple* device to operate. A line drawing of the fatigue machine is given in **figure B-1** on page 95. The fatigue specimen is mounted on a swivel mechanism and then pinned to the rotating arm, which is connected to the motor. The base of the fatigue specimen is clamped to a vise and remains stationary during operation. The mean stress is set by adjusting the vertical height of the vise and the alternating stress is set by adjusting the eccentric cam mounted on the motor axle. The beam displacement is a combination of the two adjustments and determines the stress on the surface of the fatigue specimen.

The procedures will describe the setup for fatigue tests run at R=0 (stress ratio). The instructions will refer to nomenclature provided in **figure B-1**:
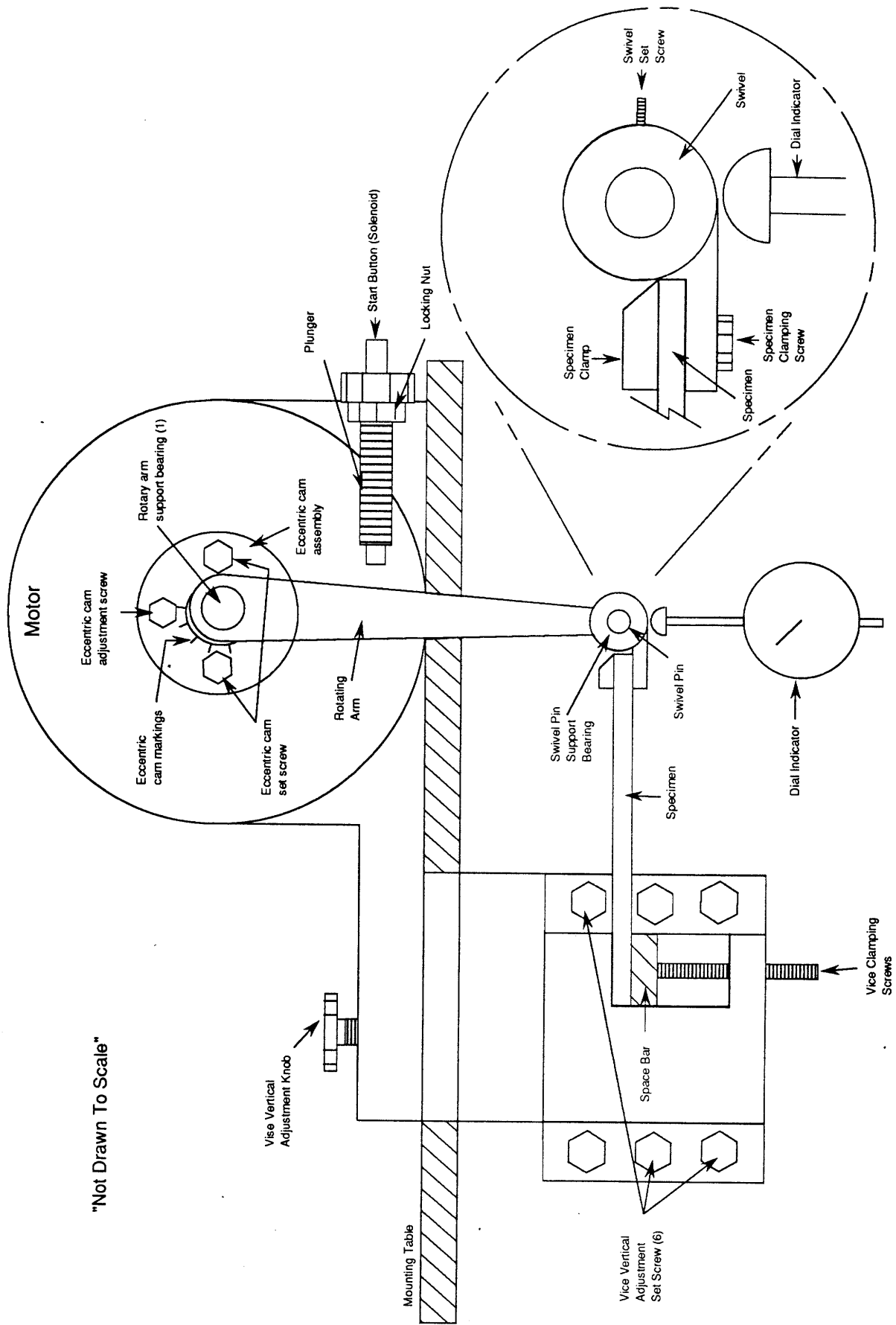
Figure B.1. Automation Industries Fatique Bending Machine

"Not Drawn To Scale"

Motor

Eccentric cam adjustment screw

Rotary arm support bearing (1)

Eccentric cam assembly

Eccentric cam markings

Eccentric cam set screw

Rotating Arm

Plunger

Start Button (Solenoid)

Locking Nut

Swivel Set Screw

Swivel

Dial Indicator

Specimen Clamp

Specimen

Specimen Clamping Screw

Swivel Pin Support Bearing

Swivel Pin

Specimen

Dial Indicator

Vise Vertical Adjustment Knob

Mounting Table

Space Bar

Vice Clamping Screws

Vice Vertical Adjustment Set Screw (6)

1) Unplug the machine from the 110 volt wall outlet.

2) Loosen the six (6) vise vertical adjustment set screws using the 3/16 inch Allen wrench. Tighten the set screws very lightly to remove the excess play in the mechanism.

3) Loosen the two clamping screws under the vise using the 3/16 inch Allen wrench. Continue turning the screws until the opening from the top of the metal spacer and the top of the vise permits the insertion of fatigue specimen. Do not install fatigue specimen.

4) Attach the fatigue specimen to the swivel as shown in **figure B-1**. Tighten the two screws lightly (finger tight).

5) Loosen the two set screws on the eccentric cam using the 3/16 inch Allen wrench. Place the 3/16 inch Allen wrench in the eccentric cam adjustment screw (top center) and turn it to center the eccentric cam to the 0 position (markings go from 0 to 50 units). Tighten the two set screws lightly to reduce the play in the mechanism.

6) Place the base of the fatigue specimen inside the vise with the swivel right-side up. While applying pressure to force the specimen to the back of the vise, tighten the two vise clamping screws using the 3/16 inch Allen wrench. Insure that the rotating arm swivel pin support is allowed to slide along the sides of the swivel without any force. It is important to be able to pin the swivel to the rotating arm pin support without using force! Several attempts may be necessary to insure proper alignment.

7) Adjust the vertical height of the vise with the installed fatigue specimen so that the swivel pin can slide easily through the swivel and the rotating arm pin support. Insure that the swivel pin set screw is backed out far enough to allow the swivel pin to go through the swivel. Leave the pin installed, but do not tighten swivel pin set screw.

8) Tighten the two fatigue specimen clamping screws on the swivel using the 9/64 inch Allen wrench.

9) Setup the dial indicator: place the dial indicator probe under the bottom of the swivel so that movement of the swivel pin in a vertical direction is registered on the dial indicator. Downward movement of the swivel pin should correspond to a positive dial indicator reading.

The dial indicator should be positioned on a firm platform or anchored using the magnetic clamps. The dial indicator is a delicate instrument, requiring care and attention to detail. The dial indicator probe must rest in the center of the swivel directly below the center of the swivel pin.

10) This step will zero the beam displacement. Once the dial indicator is installed, turn the eccentric cam assembly with your hand and observe the total travel of the swivel pin on the dial indicator. Adjust the eccentric cam using the 3/16 inch Allen wrench until the total travel registered on the dial indicator is less than ±2.0 mils. Adjust the dial on the dial indicator so that the 0 mils mark is at the center of the needle travel. This may require several iterations before you can continue! Remove the swivel pin from the swivel. The fatigue specimen will shift up or down slightly, adjust the vertical height of the vise to zero the dial indicator. If properly done, the swivel pin will slide back in without effort. Readjust the eccentric cam to obtain a total travel of ±1.0 mil on the dial indicator. At this vise vertical height setting there is fully reversed bending.

11) Calculate the desired displacement using the following formula:

$$\sigma = \frac{E \, t \, \delta}{L^2} \qquad \text{(equation B-1)}$$

The derivation of this formula is contained in **Appendix A**. To set an R ratio equal to 0 requires the vise vertical height to be lowered a distance $y = \delta/2$.

12) Remove the swivel pin and lower the vise a distance equal to y, the distance will be measured in a positive clockwise direction on the dial indicator. Once the vise vertical is at the proper position, carefully tighten the six (6) vise vertical adjustment set screws to fix the position. Technique: tighten one screw on one side of the vise a little then tighten the corresponding screw on the other side of the vise the same amount. Continue this procedure until all six (6) screws are completely tightened, evenly. This technique should allow setting the vise vertical position to $y \pm 0.5$ mil (0.0005 inches).

13) Eccentric cam adjustment. Before continuing this step calculate the value of x to set on the eccentric cam. The following formula is derived in **figure B-2** by geometry:

$$x = \frac{100}{\pi} \sin^{-1} (\delta) \qquad \text{(equation B-2)}$$

Using the 3/16 inch Allen wrench, set the x value in the eccentric cam. Do Not Tighten Eccentric Cam Set Screws. Carefully turn the eccentric cam with your hand aligning the swivel pin support with the swivel. Insert the swivel pin. Adjust the eccentric cam to provide the same value y read on the dial indicator. This sets $y = \delta/2$ (for R=0) as closely as possible and eliminates the errors in the x markings on the eccentric cam. Again, carefully tighten the eccentric cam set screws using the 3/16 inch Allen wrench. During the tightening sequence, check the displacement on the dial indicator. This is an iterative procedure to **fix** the displacement (δ) exactly!

14) Once the eccentric cam is properly set and tightened, remove the dial indicator. Then,remove the swivel pin. Oil the bearings using the 80-90w machine oil and wipe off the excess oil with a rag. Insert the swivel pin through the swivel pin support and swivel, aligning the flat portion of the swivel pin with the position of the swivel pin set screw. Tighten the swivel pin set screw with the 1/16 inch Allen wrench. Wipe up excess oil once more.

15) Zero the mechanical counter attached to the rear of the motor.

16) Adjust the electro-mechanical shutoff switch, so that the rotating arm will strike the plunger when specimen failure occurs. Tighten both the adjustment screw and locking nut securely. Pull or push the shutoff switch to the off position.

17) Plug the power cord into the 110 volt wall outlet. Push the small start button on the shutoff switch. The machine will turn at 1725 rpm (28.75 Hz) and the mechanical counter will record every 100 cycles. The counter has 5 digits, so it will go through 00000 after 10,000,000 cycles (4 days of continuous operation). The machine should be checked daily and occasionally stopped for lubrication.
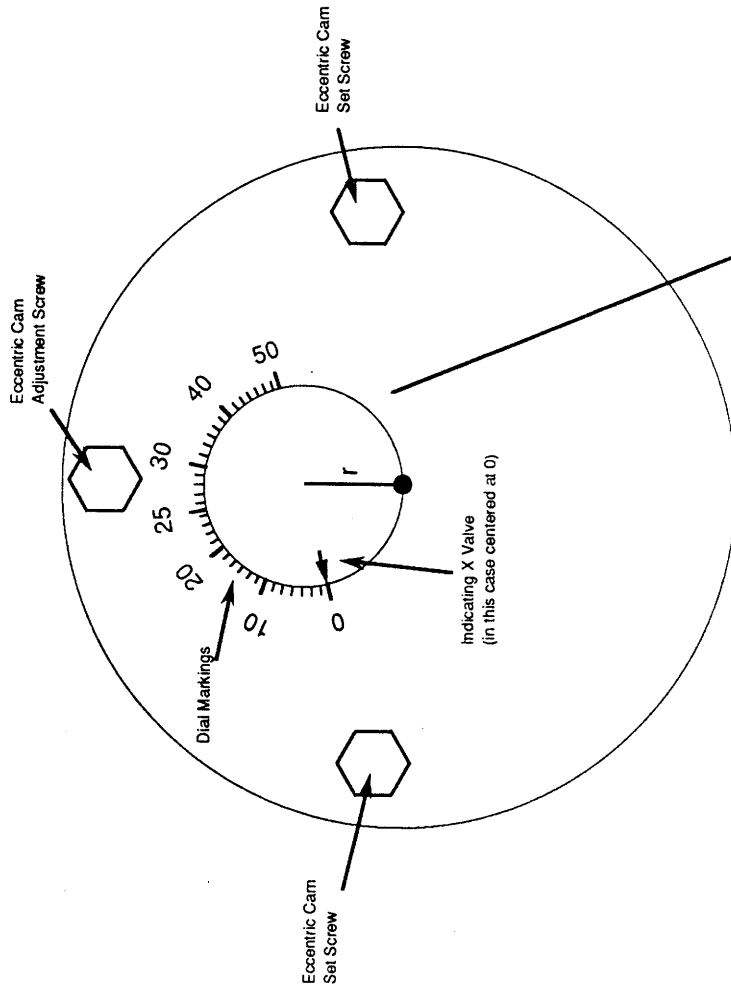
R = Distance from center of rotation of the drum to the center of the bearing.

$\delta = 2R$ = Total vertical displacement

r = radius of small cam = 0.25 in (measured)
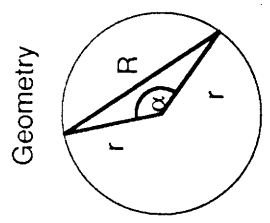
$\frac{1}{2}R = r \sin \alpha/2$

$\alpha = \frac{x}{50} \pi$ radians

$\delta = 2R = 4r \sin \left(\frac{x}{100} \pi \right)$ when r=0.25 in

$\delta = \sin \left(\frac{x}{100} \pi \right)$ or $x = \frac{100}{\pi} \sin^{-1}(\delta)$

Eccentric Cam Set Screw

Eccentric Cam Adjustment Screw

Eccentric Cam Set Screw

Dial Markings

Indicating X Valve (in this case centered at 0)

50 40 30 25 20 10 0

r

Geometry

R r r α

Figure B.2. Eccentric Cam Mechanism

Appendix C

Pretreatments and Post-Treatments Used for Electroless Nickel Coatings

The Custom 450® Stainless Steel specimens were coated as follows:

Teledyne Neosho, Lea-Ronal NICKELMERSE SPL Coating

1. Degrease
2. Water rinse then Glass Bead Blasting @ 30 psi
3. Water rinse
4. Electrolytic Clean:
   a. alkaline soak - 1.5 minutes
      8-12 oz. Oakite 90/gal water
   b. Metex soak (16 oz. Metex 629/ gal water)
      for 1 minute current application with
      one minute current reversal
5. Water rinse

6. Woods Nickel Strike - 2 minutes
   28-32 óz. nickel chloride/gal water,
   10-16 oz. HCL/gal water (distilled)
7. Water rinse

Enthone Ni-422 & Ni-426 Coatings

1. Degrease - 5 minutes
2. No Blasting performed
3. Water rinse - 5 minutes
4. Electrolytic Clean:

   Endox® 214,
   periodic current reversal
   removed anodically

5. Water rinse - 5 minutes
6. Acid activation - 30 sec
   40% HCL, 10% sulfuric
   acid & 0.5% Actane 32
7. Water rinse - 5 minutes

8. Sulfamate Nickel Strike:
   2-3 minutes, 32°C (90°F)

9. Water rinse

Plating

Electroless Nickel Plating:

NICKELMERSE SPL

Electroless Nickel Plating:

Ni-422 or Ni-426

Post Plating Procedures

1. Cold water rinse
2. Hot water rinse

3. Hydrogen Embrittlement Relief and Hardness HT
   Bake at 274°C (525°F) for one hour

1. Hot water rinse
2. Forced air dried

3. Embrittlement Relief
   Bake at 191°C (375°F)
   for 4 hours

Tensile Test Data - Stress versus Strain Curves

**Custom 450® Stainless Steel
Aged 4 Hours at 550°C, Specimen #1**

U.T.S. 1158 MPa
% Elongation 17.3%

0.2% offset yield is:
1110 MPa
161,000 psi
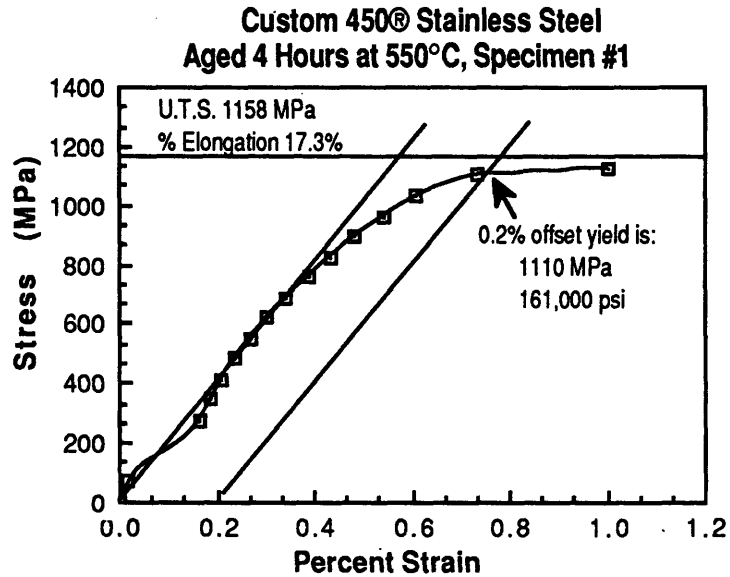
Figure D-1. Stress versus Strain for Tensile Specimen #1.

**Young's Modulus
Determined from Slope**

$y = -50.064 + 2212.3x \quad R^2 = 0.986$

Young's Modulus is:
221.2 x E03 MPa
32.08 x E06 psi
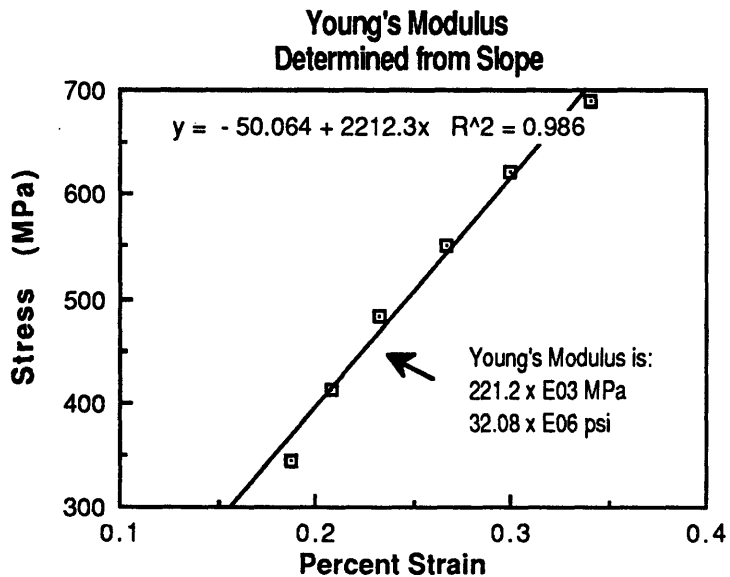
Figure D-2. Curve Fit for Stress vs Strain Curve, Specimen #1.
Young's Modulus (E) is the Slope of the Tangent Line.

Custom 450® Stainless Steel
Aged 4 Hours at 550°C, Specimen #2

U.T.S. 1161 MPa
% Elongation 21.3%

0.2% offset yield is:
1089 MPa
158,000 psi

Percent Strain
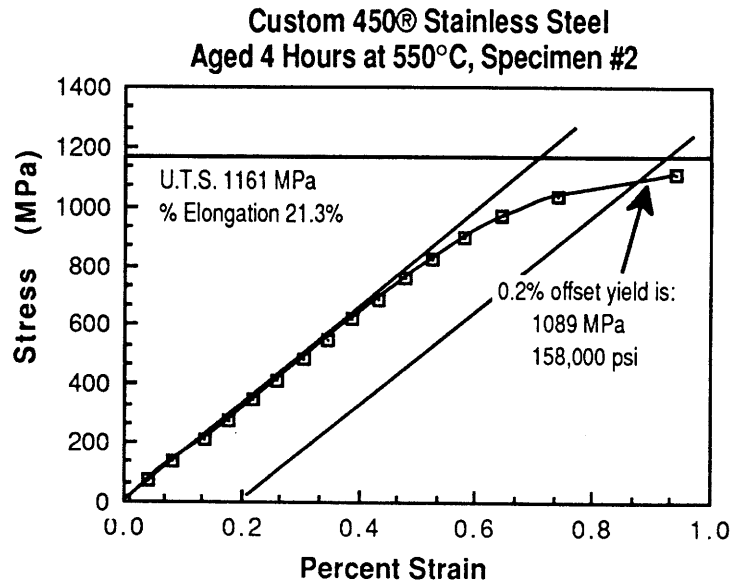
Figure D-3. Stress versus Strain for Tensile Specimen #2.

Young's Modulus
Determined from Slope

$y = -0.81021 + 1593.6x \quad R^2 = 0.999$

Young's Modulus is:
159.4 x E03 MPa
23.12 x E06 psi

Percent Strain
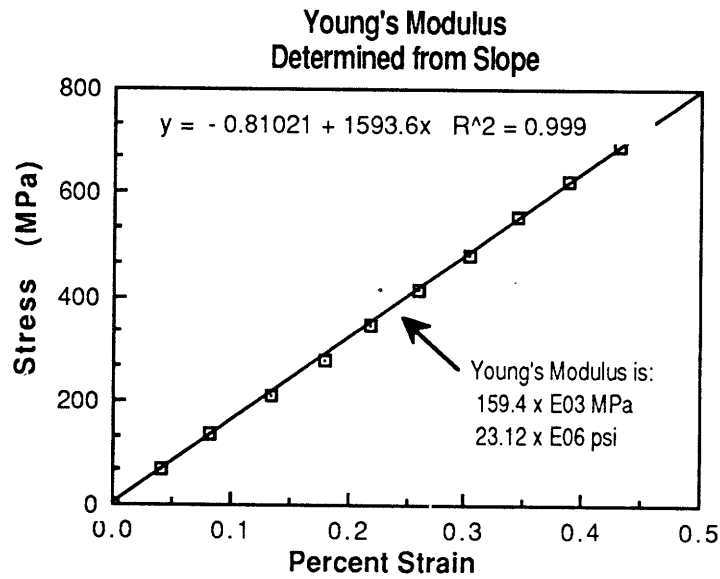
Figure D-4. Curve Fit for Stress vs Strain Curve, Specimen #2.
Young's Modulus (E) is the Slope of the Tangent Line.

Custom 450® Stainless Steel
Aged 6 Hours at 570°C, Specimen #3

U.T.S. 1092 MPa
% Elongation 18.8%

0.2% offset yield is:
997 MPa
145,000 psi
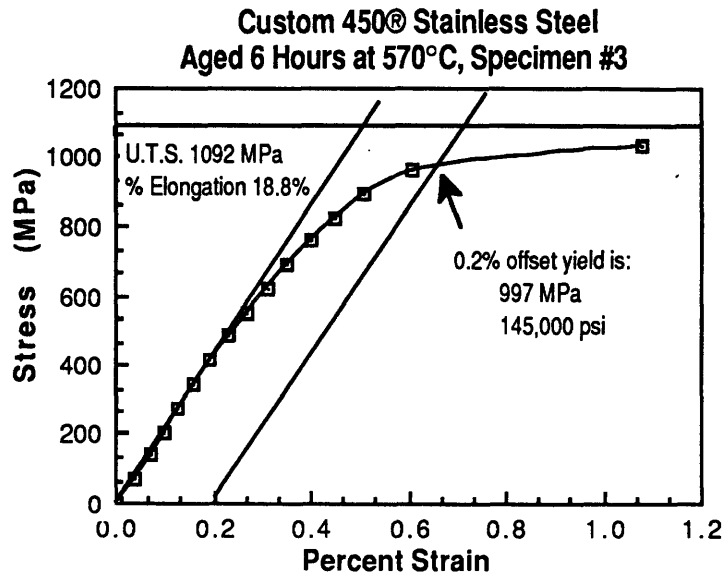
Figure D-5. Stress versus Strain for Tensile Specimen #3.

Young's Modulus
Determined from Slope

$y = -7.3767 + 2161.7x$ $R^2 = 0.998$

Young's Modulus is:
216.2 x E03 MPa
31.36 x E06 psi
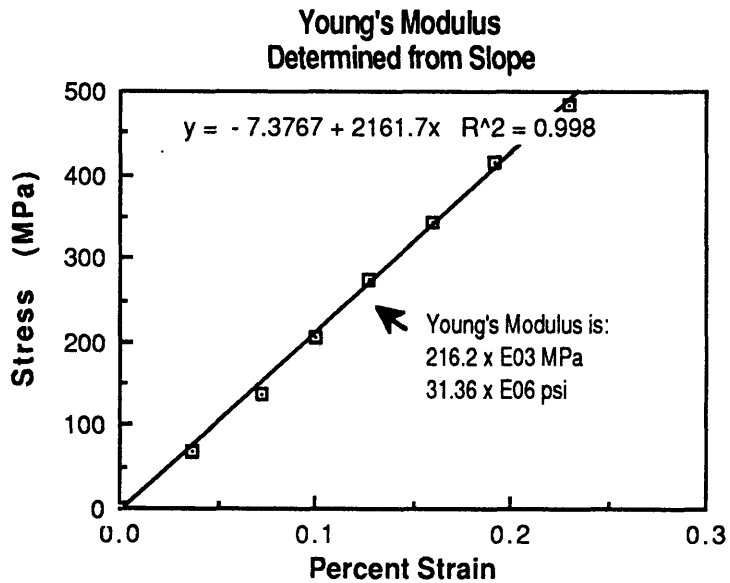
Figure D-6. Curve Fit for Stress vs Strain Curve, Specimen #3.
Young's Modulus (E) is the Slope of the Tangent Line.

Custom 450® Stainless Steel
Aged 4 Hours at 570°C, Specimen #4

U.T.S. 1090 MPa
% Elongation 17.7%

0.2% offset yield is:
1014 MPa
147,000 psi
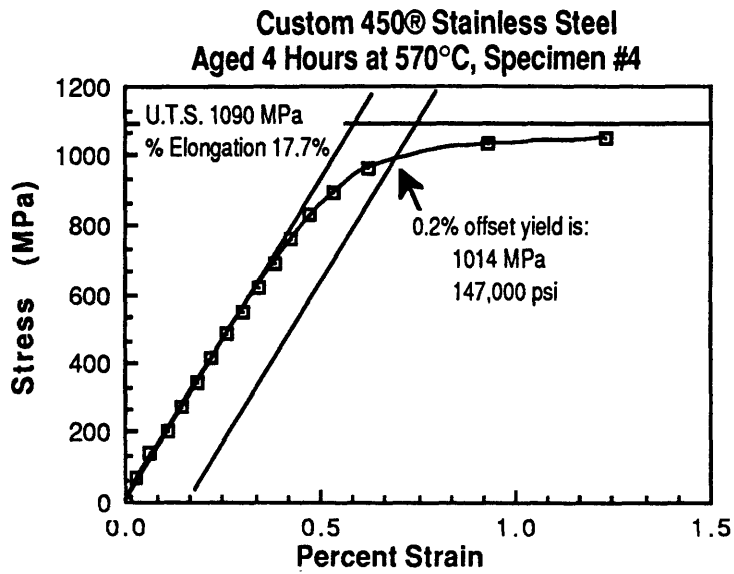
Figure D-7. Stress versus Strain for Tensile Specimen #4.

Young's Modulus
Determined from Slope

$y = 8.6446 + 1840.6x$ $R^2 = 0.998$

Young's Modulus is:
184.1 x E03 MPa
26.70 x E06 psi
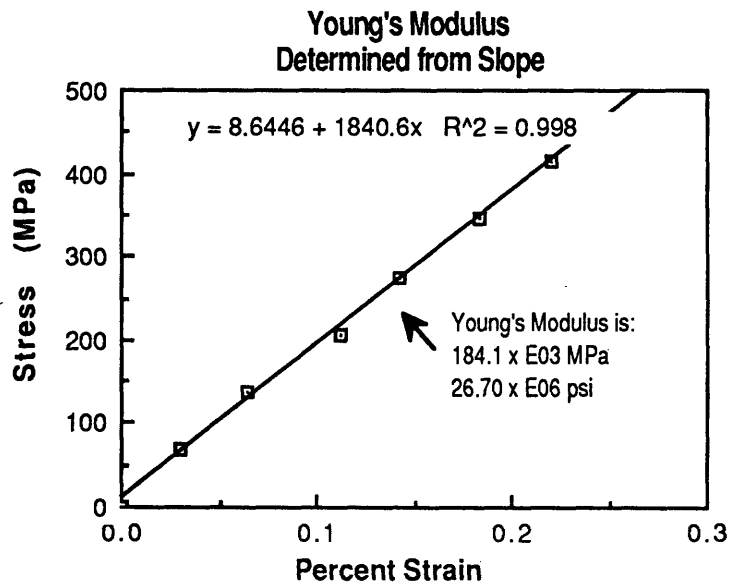
Figure D-8. Curve Fit for Stress vs Strain Curve, Specimen #4.
Young's Modulus (E) is the Slope of the Tangent Line.

Custom 450® Stainless Steel
Aged 4 Hours at 500°C, Specimen #5

U.T.S. 1154 MPa
% Elongation 14.1%

0.2% offset yield is:
1069 MPa
155,000 psi

(Stress (MPa) vs Percent Strain)
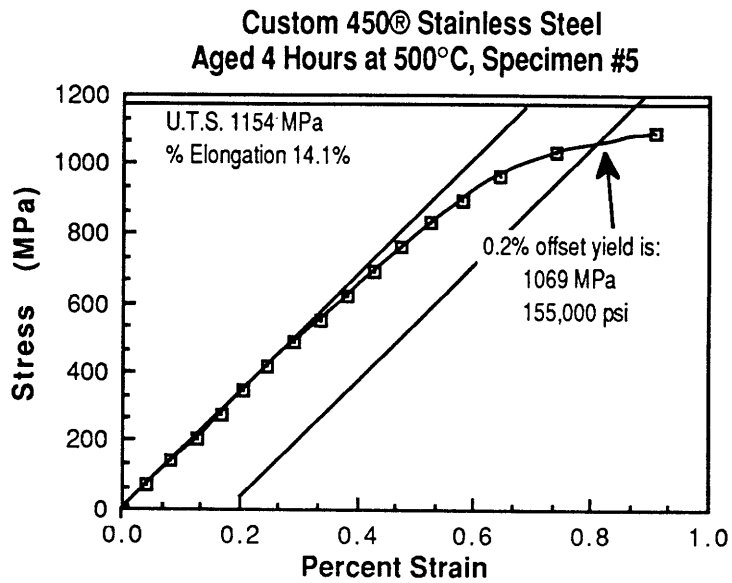
Figure D-9. Stress versus Strain for Tensile Specimen #5.

Young's Modulus
Determined from Slope

$y = -7.6953e\text{-}2 + 1670.1x$ $R^2 = 0.999$

Young's Modulus is:
167.0 x E03 MPa
24.22 x E06 psi

(Stress (MPa) vs Percent Strain)
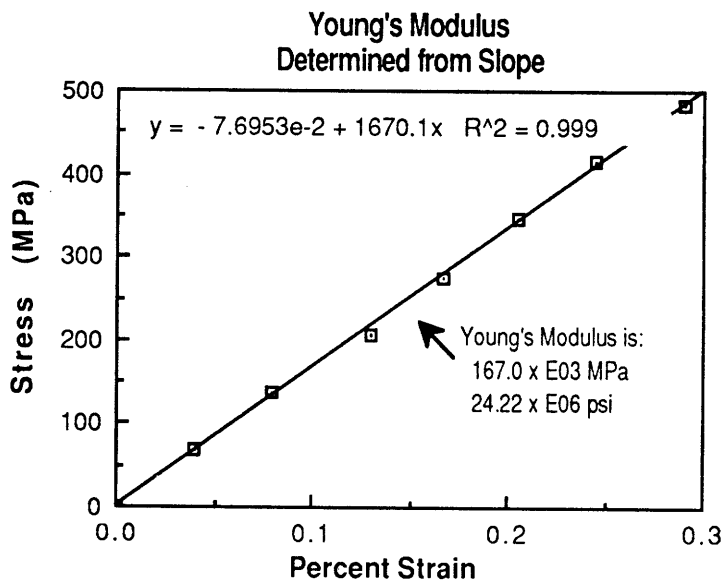
Figure D-10. Curve Fit for Stress vs Strain Curve, Specimen #5.
Young's Modulus (E) is the Slope of the Tangent Line.

104

Strain Gage Data - Stress versus Strain Curves

**Custom 450® Stainless Steel
Aged 4 Hours at 500°C, Specimen #6**
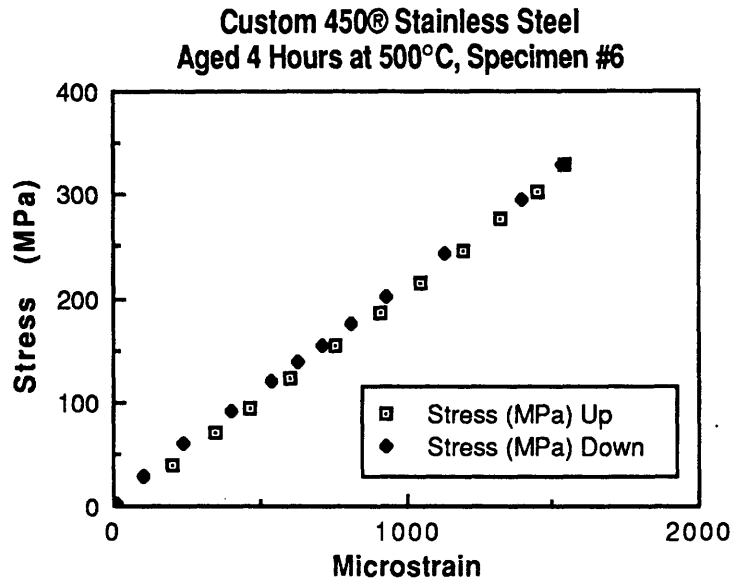
Figure E-1. Stress versus Strain for Tensile Specimen #6.

**Young's Modulus
Determined from Slope**

$y = 6.9758 + 0.20855x$ $R^2 = 0.999$

Young's Modulus;
208.5 x E03 MPa
30.24 x E06 psi
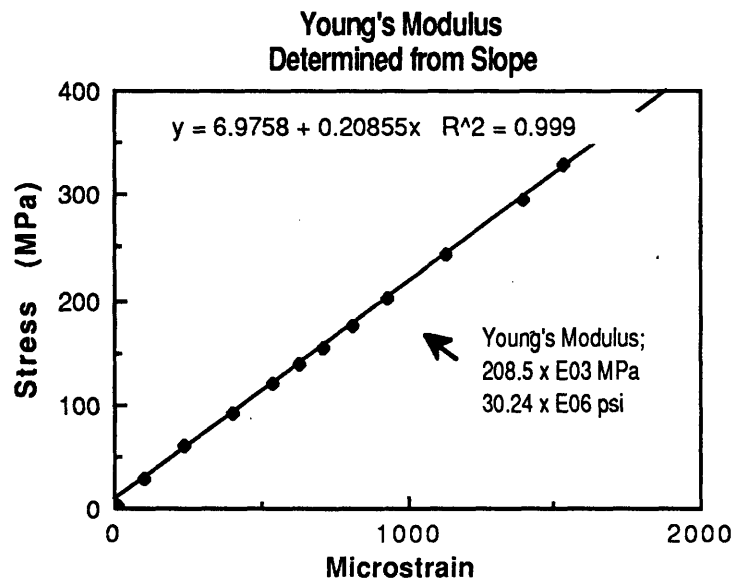
Figure E-2. Curve Fit for Stress vs Strain Curve, Specimen #6.
Young's Modulus (E) is the Slope of the Tangent Line.

**Custom 450® Stainless Steel
Aged 5 Hours at 570°C, Specimen #7**

□ Stress (MPa) UP
● Stress (MPa) Down
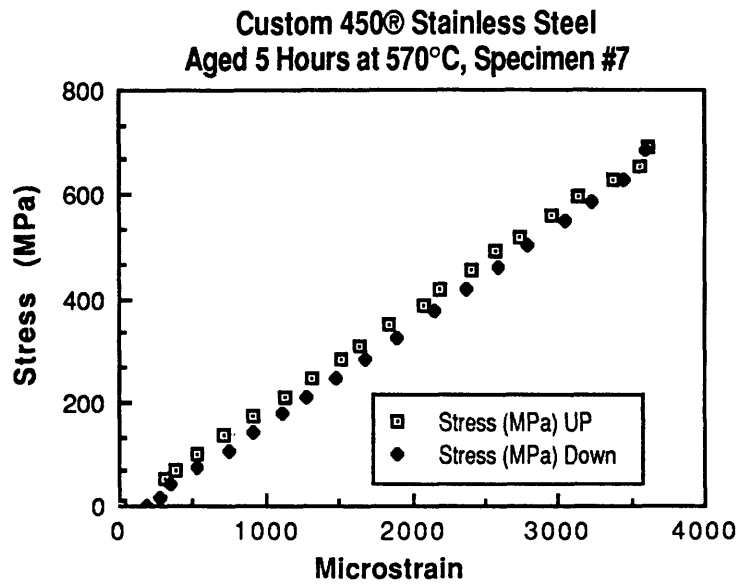
Figure E-3. Stress versus Strain for Tensile Specimen #7.

**Young's Modulus
Determined from Slope**

$y = -37.419 + 0.19338x$ $R^2 = 0.999$

Young's Modulus ;
193.4 x E03 MPa
28.05 x E06 psi
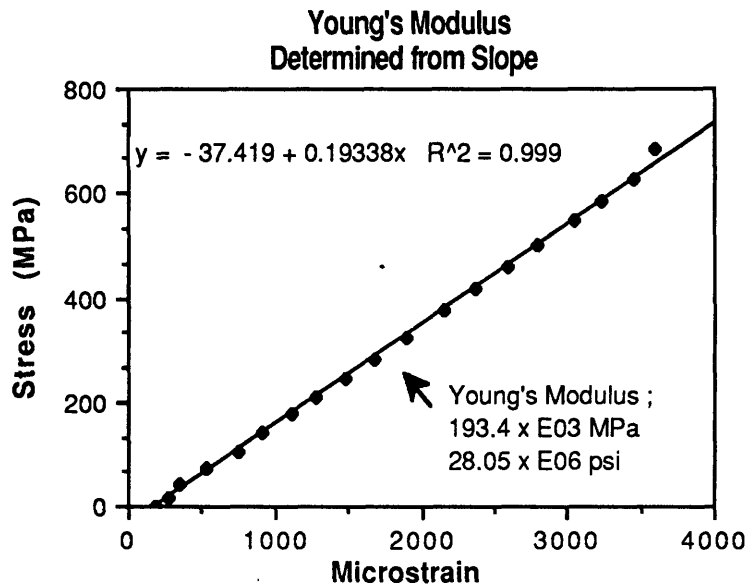
Figure E-4.. Curve Fit for Stress vs Strain Curve, Specimen #7.
Young's Modulus (E) is the Slope of the Tangent Line.

Scanning Electron Microscope (SEM) Photographs
Tensile Test Specimen Photographs
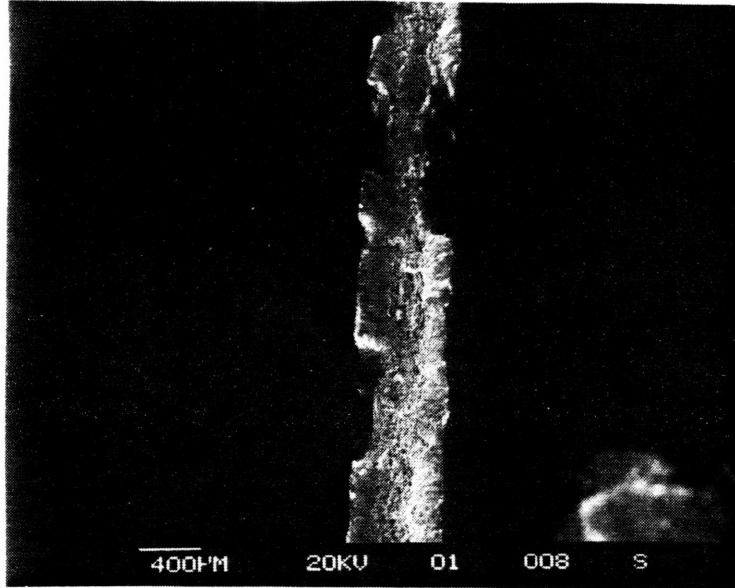
Figure F-1. Longitudinal Cross-Section of Tensile Specimen #3, Custom 450® Stainless Steel (photo 008). Heat Treatment: 6 hours at 570°C. General surface features are visible; shear lips on the outside edges with fast-fracture (ductile) region in center.
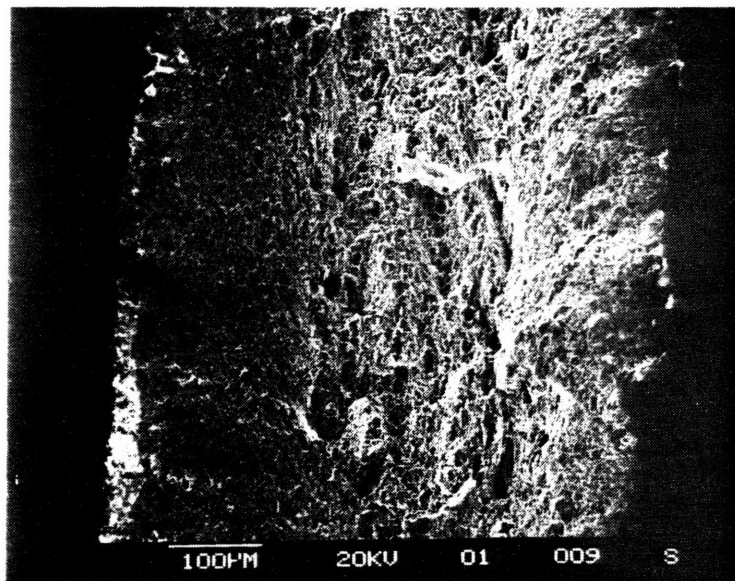
Figure F-2. Longitudinal Cross-Section of Tensile Specimen #3, Custom 450® Stainless Steel (photo 009). Heat Treatment: 6 hours at 570°C. Enlargement of center (ductile) region of **figure F-1**. The cup-cone features typical of ductile fracture are more clearly evident as are the shear lips.
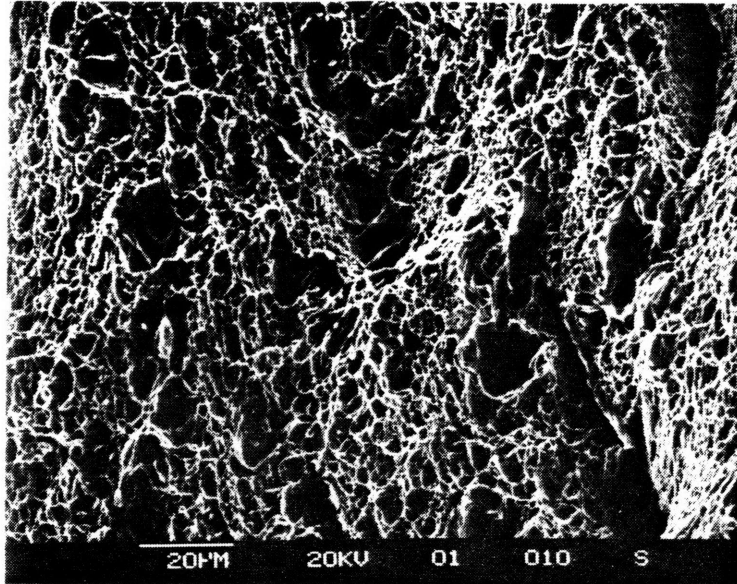
Figure F-3. Longitudinal Cross-Section of Tensile Specimen #3, Custom 450® Stainless Steel (photo 010). Heat Treatment: 6 hours at 570°C. Enlargement of center (ductile) region of **figure F-2**. Note in particular the sharp crack in the bottom right corner.
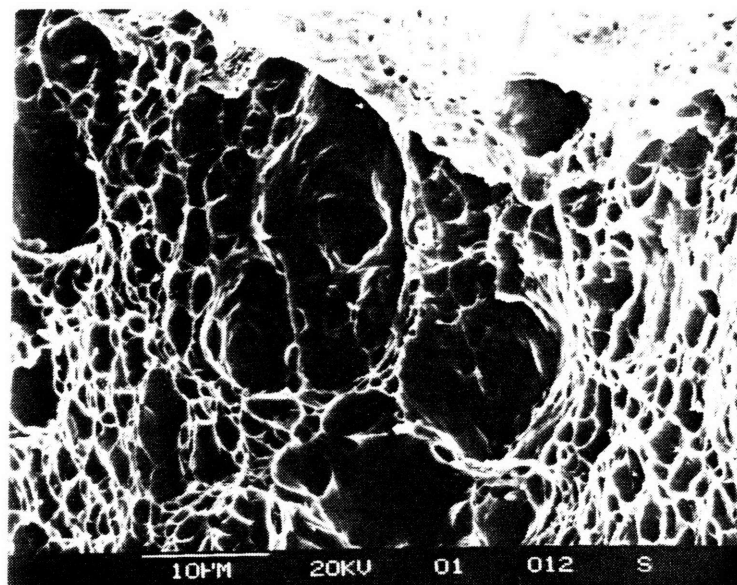
Figure F-4. Longitudinal Cross-Section of Tensile Specimen #3, Custom 450® Stainless Steel (photo 012). Heat Treatment: 6 hours at 570°C. Enlargement of **figure F-3**. Details of microvoids are visible. Note coalescing of microvoids in the center of the photo.

Coated Fatigue Test Specimen Photographs
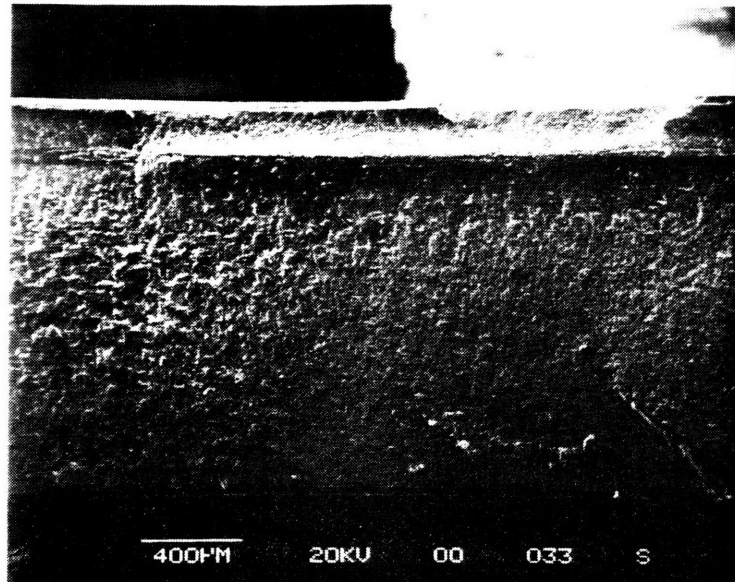
Figure F-5. Longitudinal Cross-Section of Fatigue Specimen #51 after Failure at 374,000 cycles at Room Temperature, R=0 (photo 033). Specimen coated with 30 microns of NICKELMERSE SPL electroless nickel. Observe fracture line 200 μm below top (compression) surface. Generally smooth surface features along bottom (tension) surface, indicative of brittle fatigue failure. Note large crack emanating from the coating into substrate. Shear lips along the coating (top) are visible.
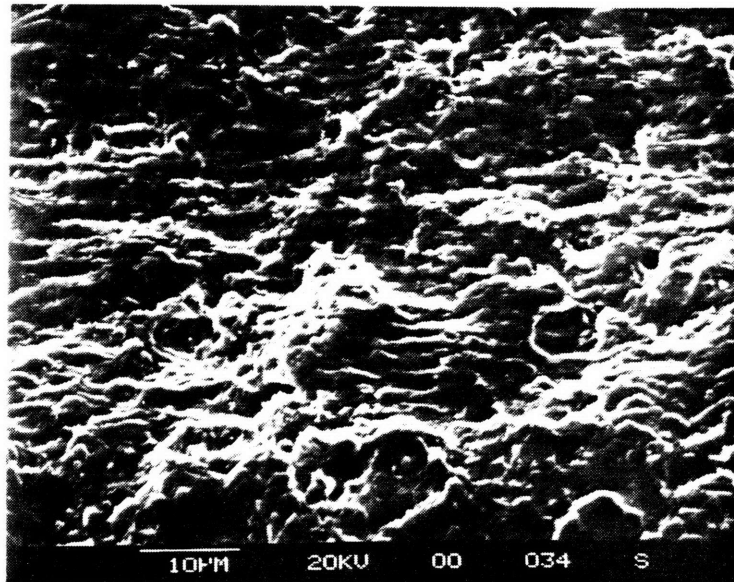
Figure F-6. Longitudinal Cross-Section of Fatigue Specimen #51 after Failure at 374,000 cycles at Room Temperature, R=0 (photo 034). Specimen coated with 30 microns of NICKELMERSE SPL electroless nickel. Close-up of fatigue specimen #51 (upper-right corner of **figure F-5**). Striations are visible. Crack front is moving from top to bottom of photo. Cracking is a stress relief mechanism.
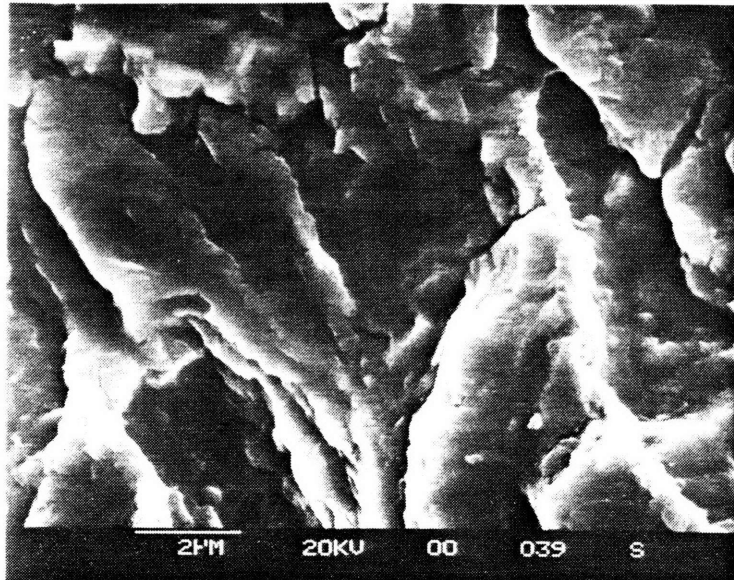
Figure F-7. Longitudinal Cross-Section of Fatigue Specimen #51 after Failure at 374,000 cycles at Room Temperature, R=0 (photo 039). Specimen coated with 30 microns of NICKELMERSE SPL electroless nickel. Enlargement of center of fatigue specimen #51 (figure F-5), approximately 500 μm below fracture line. Cleavage, evidence of brittle fracture, is visible.

Coated Fatigue Specimen Surface Photographs
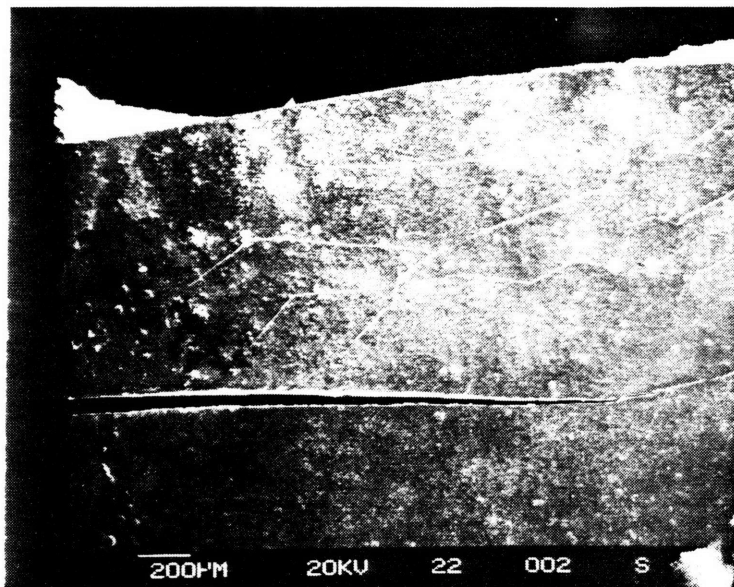
Figure F-8. Tension Surface of Fatigue Specimen #60 (36X) after Failure at 244,700 cycles at Room Temperature, R=0 (photo 002). Specimen coated with 25 microns of Enthone Ni-422 electroless nickel. Close-up of the coating. Note large crack in the coating below fracture. Note cracking, in particular bifurcation (branching) of secondary cracks. There is an absence of cracking below major crack.

110
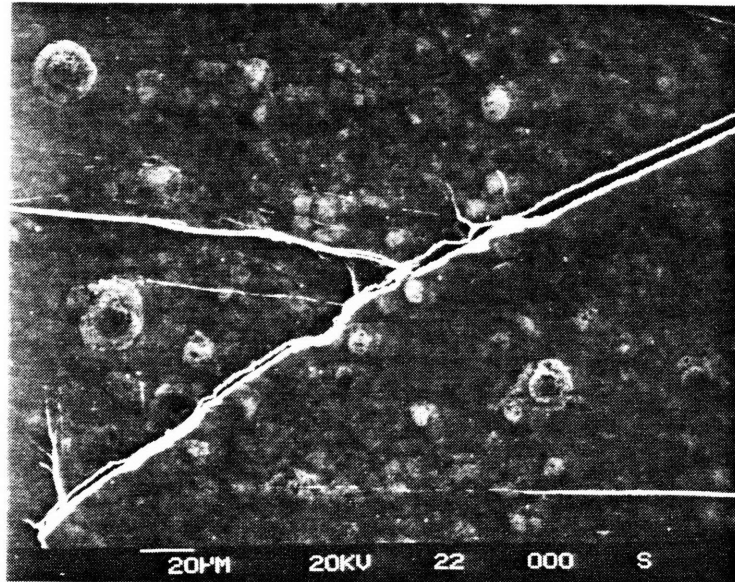
Figure F-9. Tension Surface of Fatigue Specimen #60 (360X) after Failure at 244,700 cycles at Room Temperature, R=0 (photo 000). Specimen coated with 25 microns of Enthone Ni-422 electroless nickel. Close-up of **figure-F-8**, center of crack region between fatigue fracture surface and major crack. Note bifurcation of secondary cracks, a tell-tale feature of <u>brittle</u> materials.
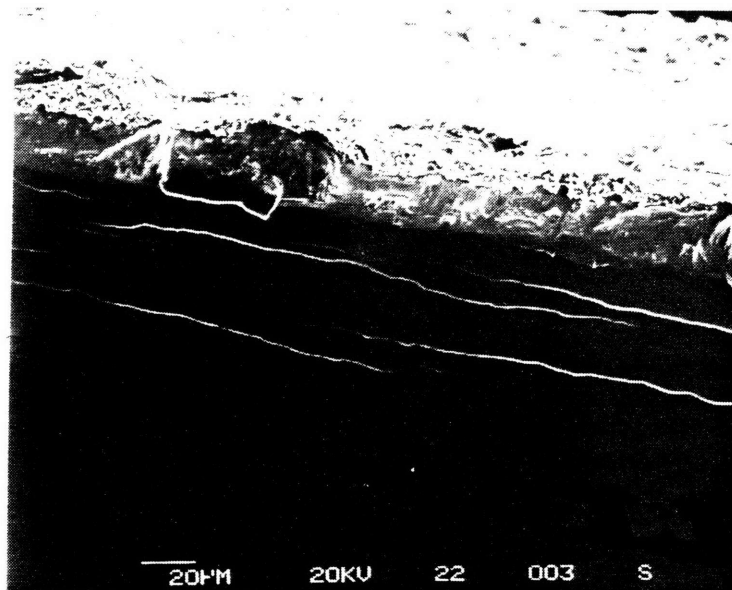
Figure F-10. Compression Surface of Fatigue Specimen #60 (360X) after Failure at 244,700 cycles at Room Temperature, R=0 (photo 003). Specimen coated with 25 microns of Enthone Ni-422 electroless nickel. Cracks are only visible in the region immediately below the fracture surface. Cracks are parallel to the fatigue fracture surface and do <u>not</u> bifurcate.

Appendix G

Graphical Surface Roughness Measurements

The data presented in this section was obtained using a TENCOR INSTRUMENTS Alpha-Step 200 Surface Profilometer as described in **section 3.7**. Fatigue specimen pretreatment, plating and post-treatment processes are given in **Appendix C**.
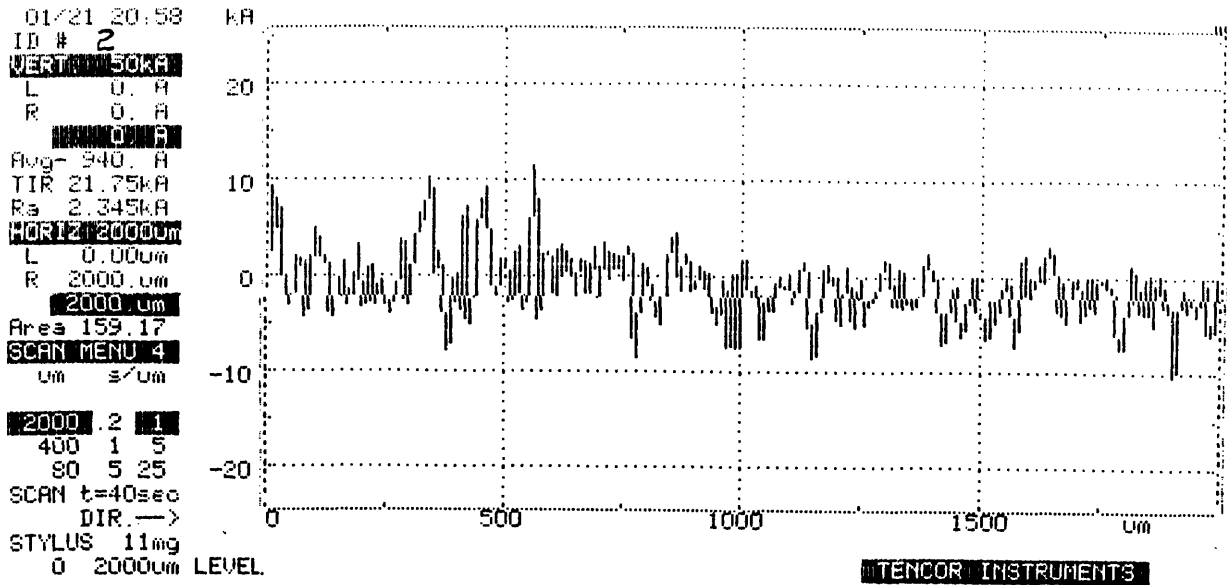
Figure G-1. Surface Profile Measurements of Fatigue Specimen #2, Location A, **Before** Teledyne Neosho Pretreatment and NICKELMERSE SPL Plating.
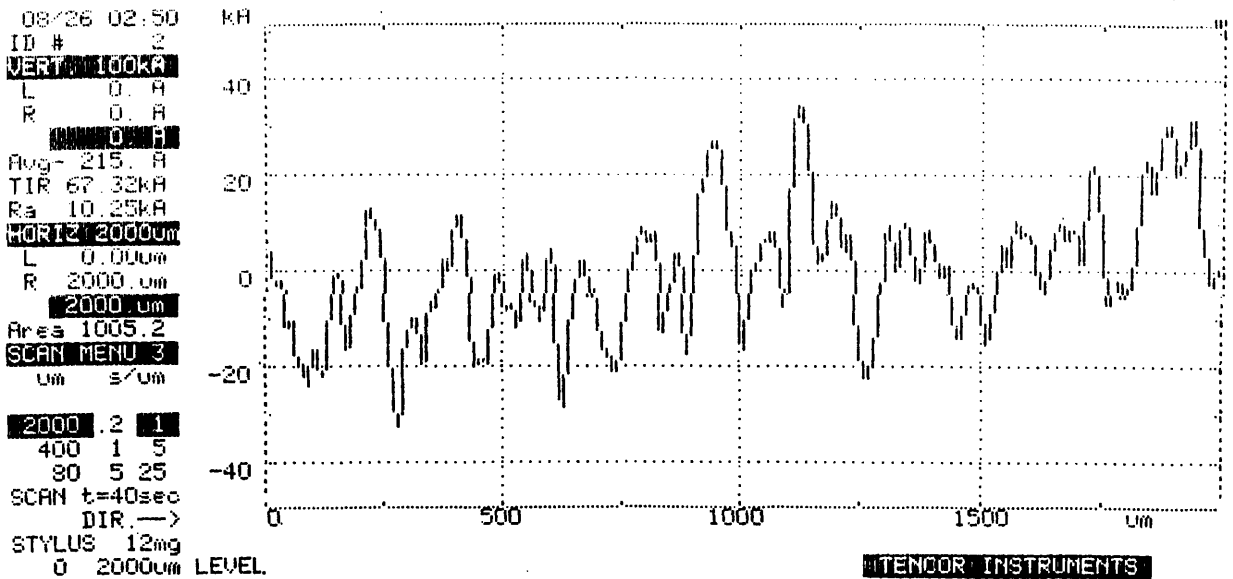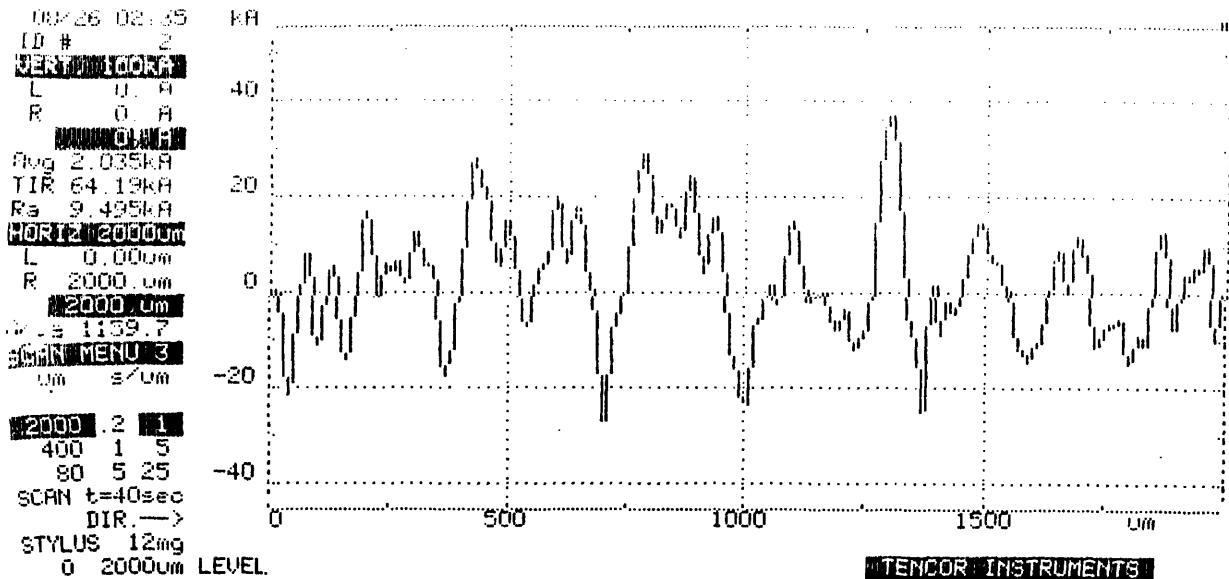

Figure G-2. Surface Profile Measurements of Fatigue Specimen #2, Location A, **After** Teledyne Neosho Plating Treatments.
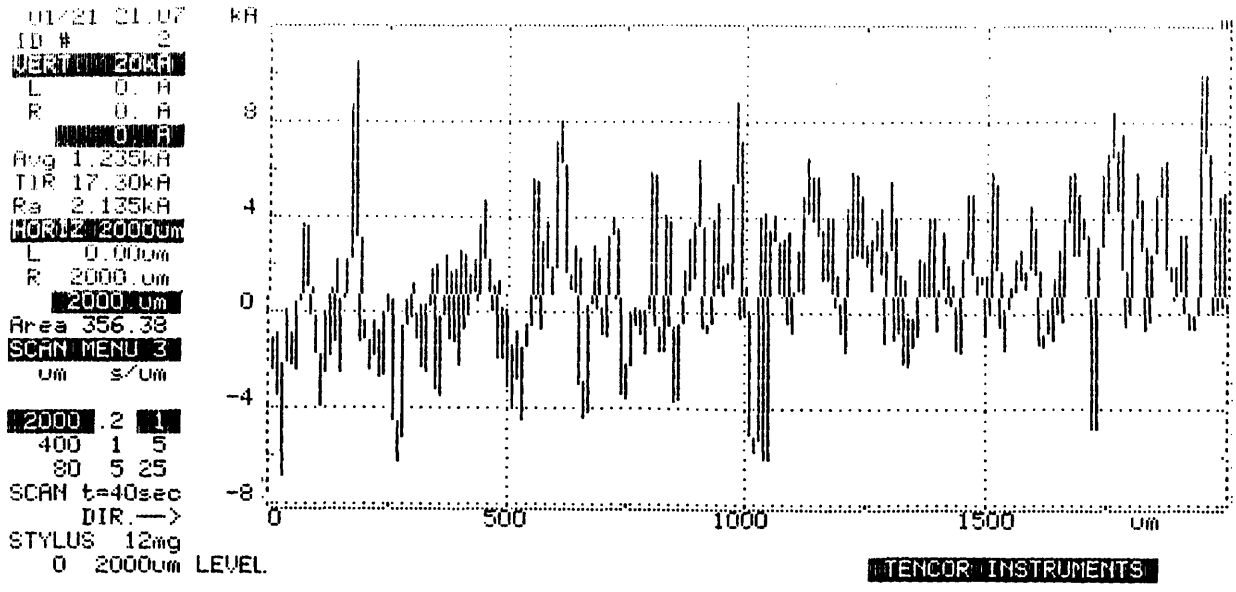
Figure G-3. Surface Profile Measurements of Fatigue Specimen #2, Location B, **Before** Teledyne Neosho Pretreatment and NICKELMERSE SPL Plating.
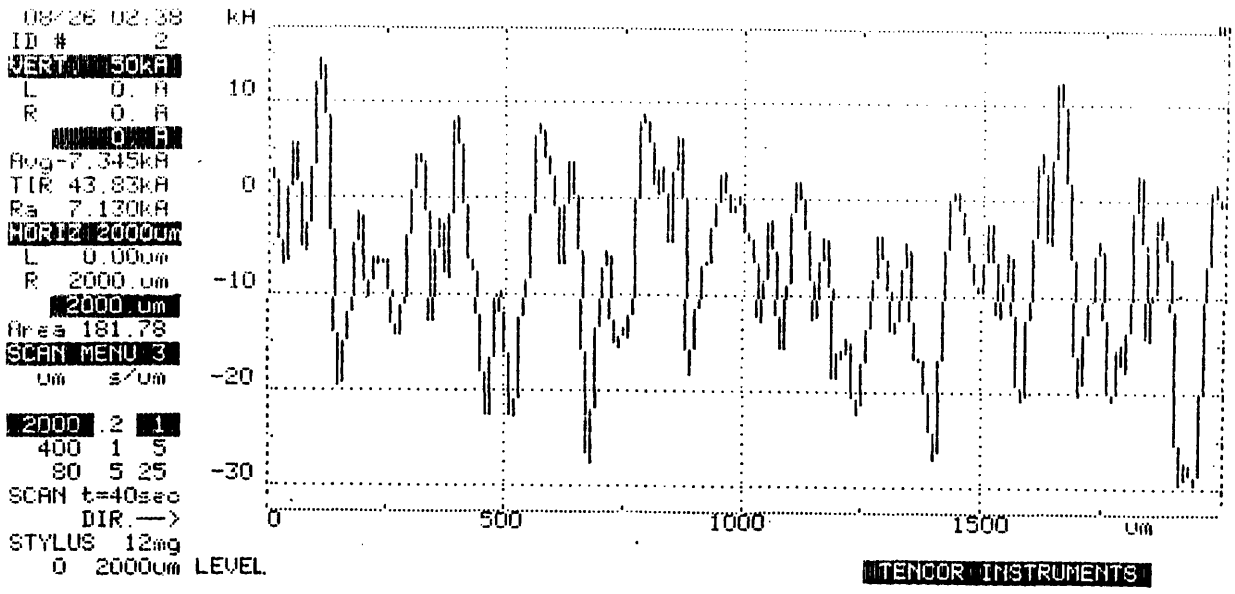
Figure G-4. Surface Profile Measurements of Fatigue Specimen #2, Location B, **After** Teledyne Neosho Plating Treatments.
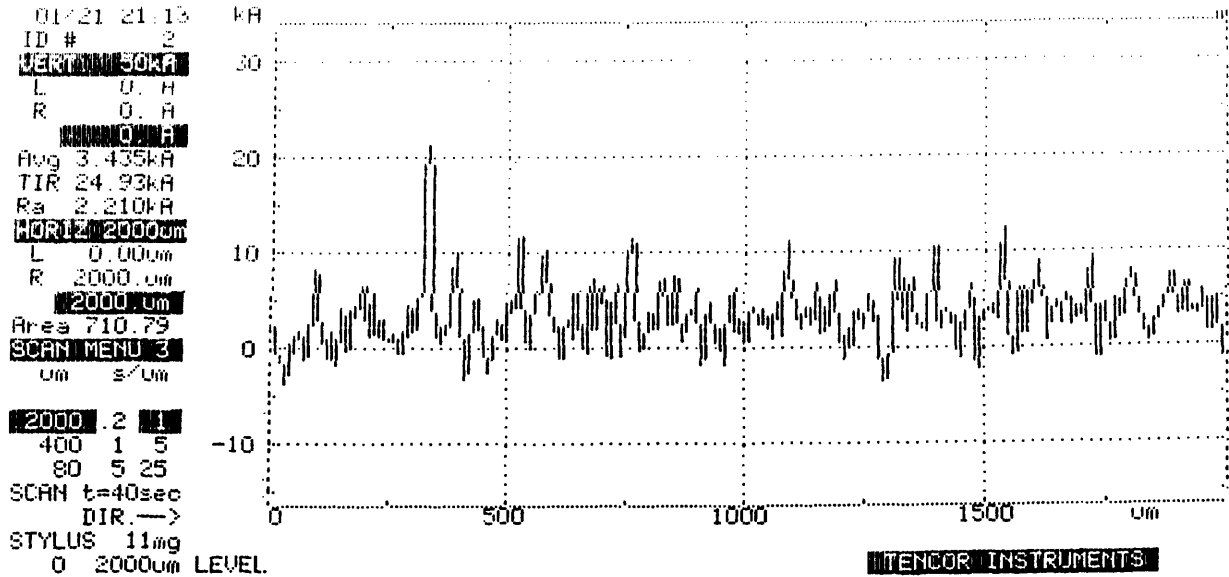
Figure G-5. Surface Profile Measurements of Fatigue Specimen #2, Location C, **Before** Teledyne Neosho Pretreatment and NICKELMERSE SPL Plating.

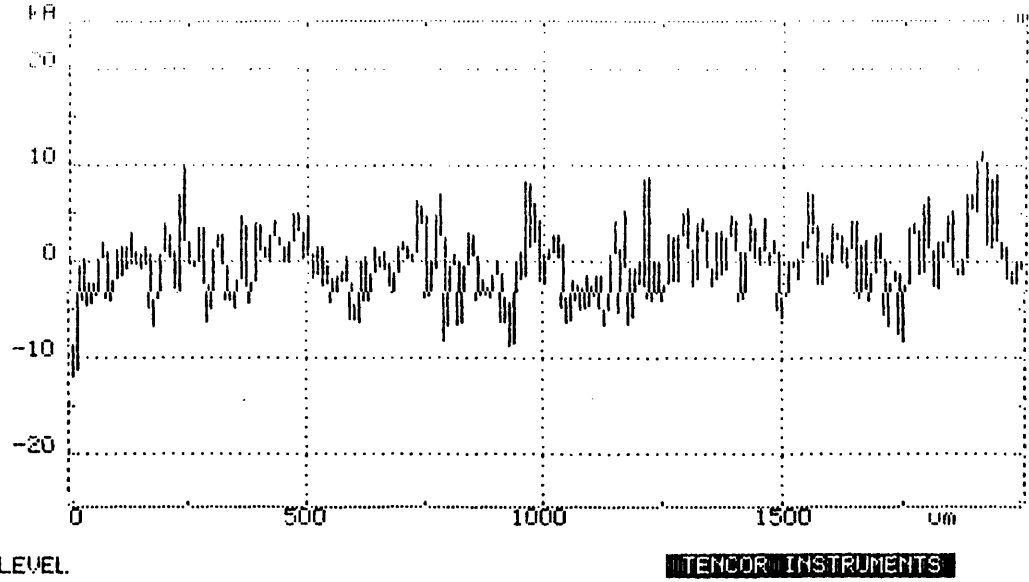**Figure G-6**. Surface Profile Measurements of Fatigue Specimen #2, Location C, **After** Teledyne Neosho Plating Treatments.

Figure G-7. Surface Profile Measurements of Fatigue Specimen #5, Location A, **Before** Enthone Ni-426 Plating Treatments.

Figure G-8. Surface Profile Measurements of Fatigue Specimen #5, Location A, **After** Enthone Ni-426 Plating Treatments.

Figure G-9. Surface Profile Measurements of Fatigue Specimen #5, Location B, **Before** Enthone Ni-426 Plating Treatments.
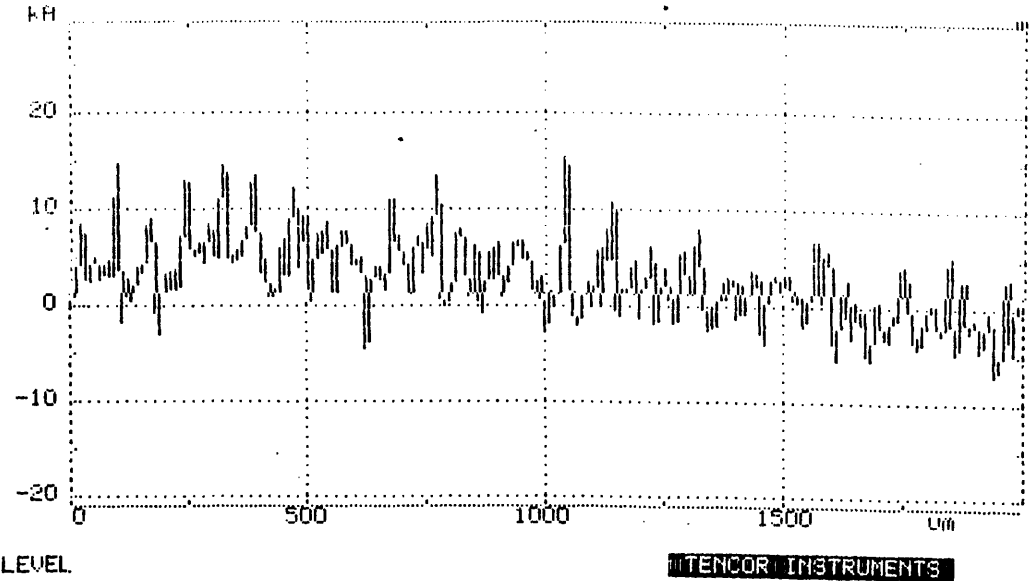

Figure G-10. Surface Profile Measurements of Fatigue Specimen #5, Location B, **After** Enthone Ni-426 Plating Treatments.
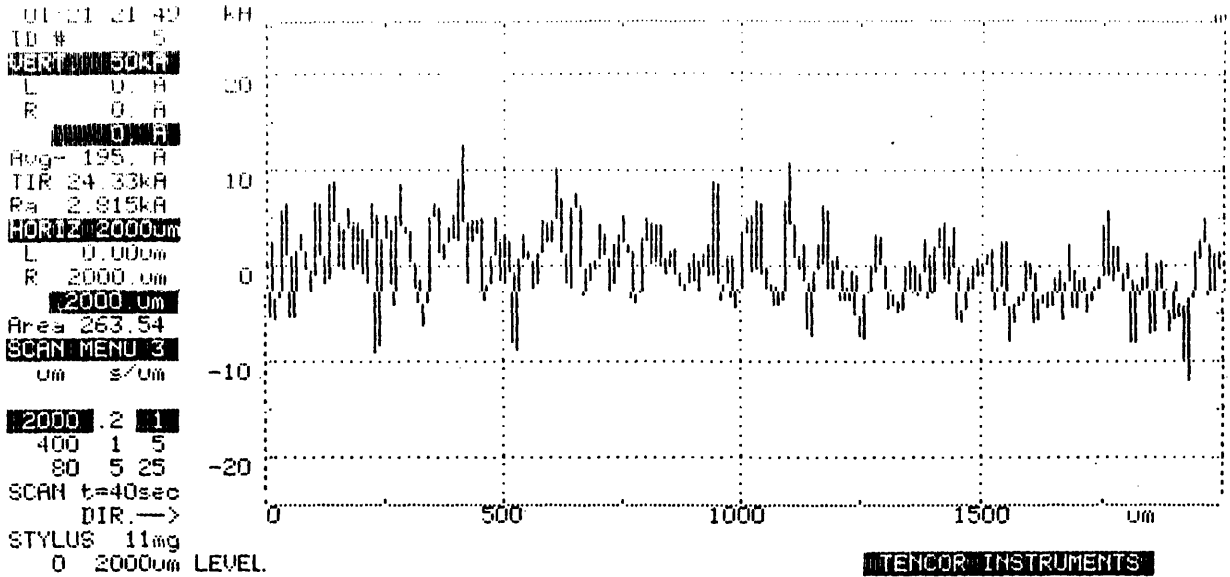
Figure G-11. Surface Profile Measurements of Fatigue Specimen #5, Location C, **Before** Enthone Ni-426 Plating Treatments.
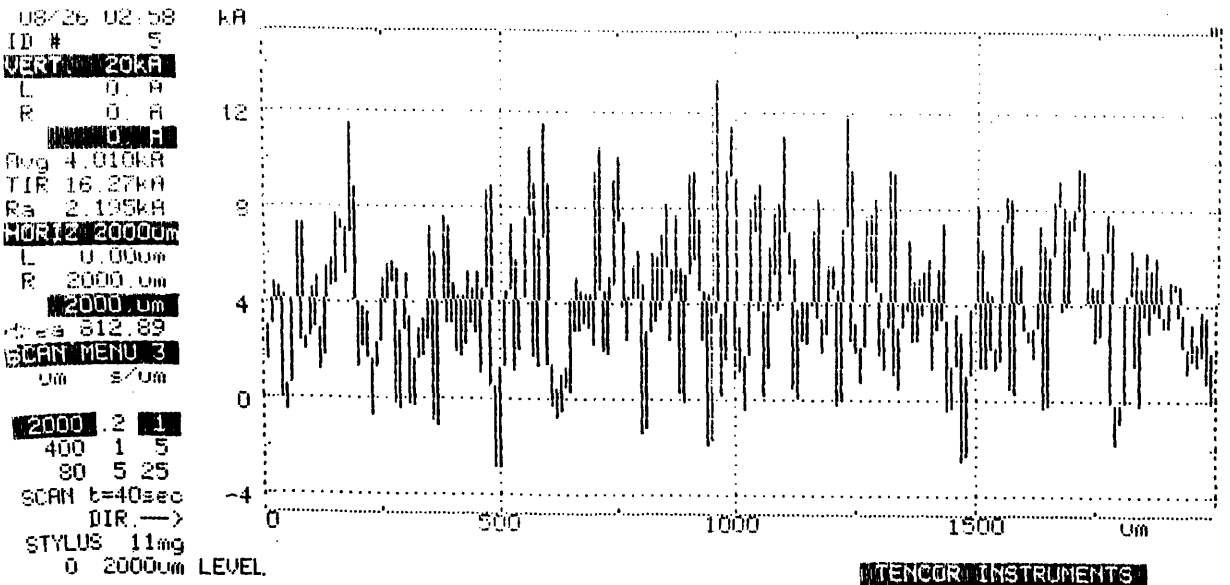

Figure G-12. Surface Profile Measurements of Fatigue Specimen #5, Location C, **After** Enthone Ni-426 Plating Treatments.
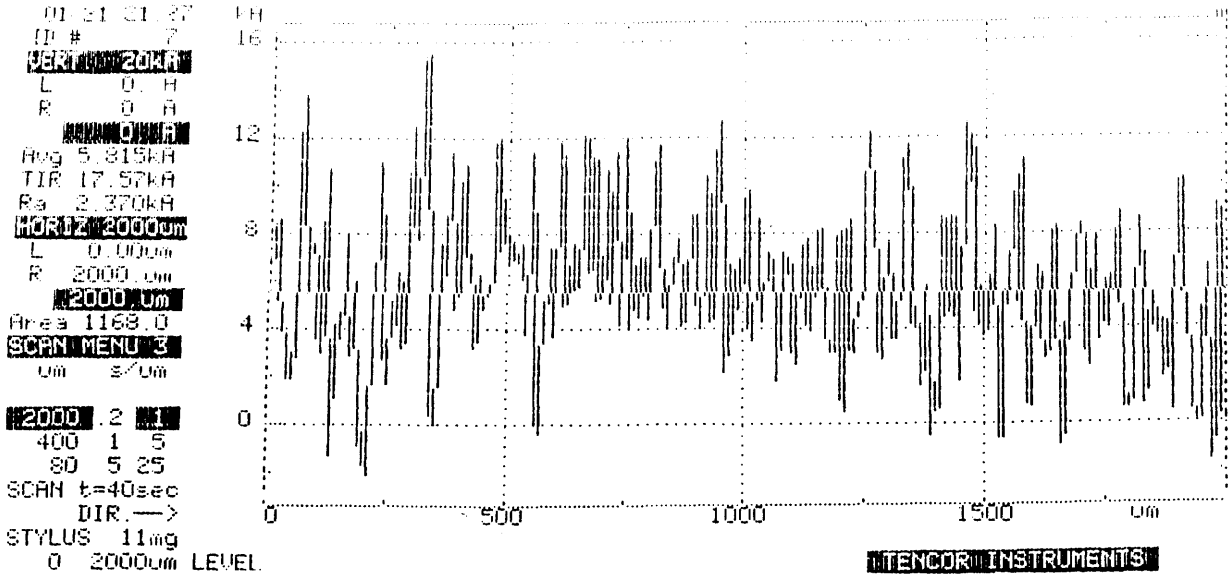
Figure G-13. Surface Profile Measurements of Fatigue Specimen #7, Location A, **Before** Enthone Ni-426 Plating Treatments.
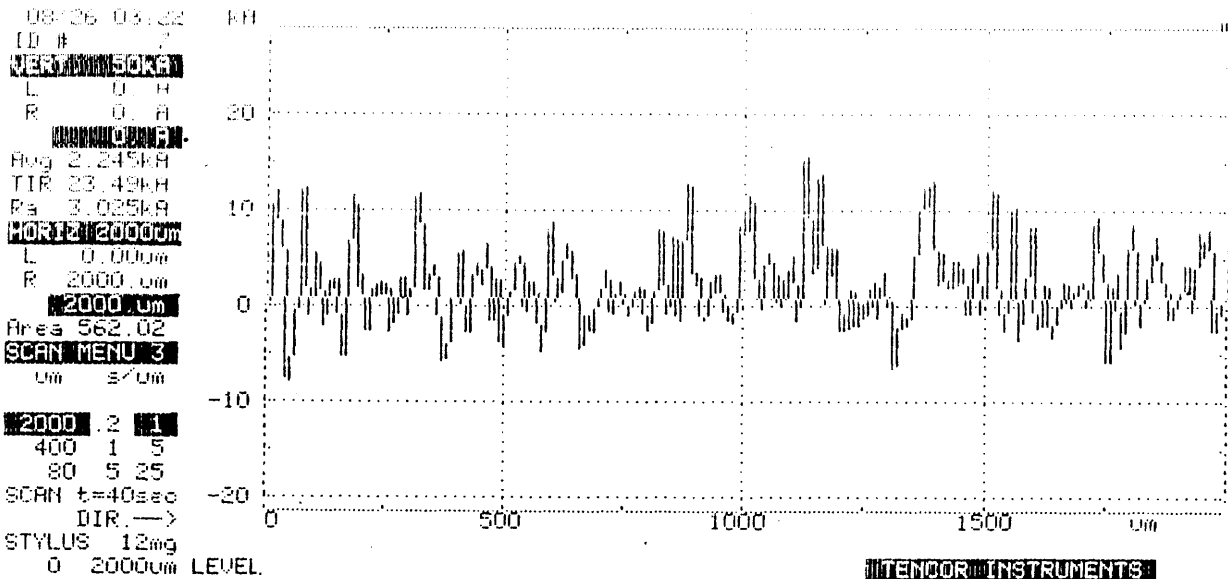

Figure G-14. Surface Profile Measurements of Fatigue Specimen #7, Location A, **After** Enthone Ni-426 Plating Treatments.

01/21 21:33
ID #   7
VERT 20kA
L   0. A
R   0. A
       0. A
Avg- 625. A
TIR 18.36kA
Ra 2.175kA
HORIZ 2000um
L   0.00um
R   2000.um
   2000. um
Area 163.09
SCAN MENU 3
 um   s/um

2000 .2 1
 400 1 5
  80 5 25
SCAN t=40sec
    DIR.—>
STYLUS 11mg
  0 2000um LEVEL.

kA
8
4
0
-4
-8
0   500   1000   1500   um

TENCOR INSTRUMENTS

Figure G-15. Surface Profile Measurements of Fatigue Specimen #7, Location B, **Before** Enthone Ni-426 Plating Treatments.

03/26 03:16
ID #   7
VERT 50kA
L   0. A
R   0. A
       0. A
Avg 3.275kA
TIR 23.91kA
Ra 2.830kA
HORIZ 2000um
L   0.00um
R   2000.um
   2000. um
Area 717.17
SCAN MENU 3
 um   s/um

2000 .2 1
 400 1 5
  80 5 25
SCAN t=40sec
    DIR.—>
STYLUS 12mg
  0 2000um LEVEL.

kA
20
10
0
-10
-20
0   500   1000   1500   um

TENCOR INSTRUMENTS

Figure G-16. Surface Profile Measurements of Fatigue Specimen #7, Location B, **After** Enthone Ni-426 Plating Treatments.

119

Figure G-17. Surface Profile Measurements of Fatigue Specimen #7, Location C, Before Enthone Ni-426 Plating Treatments.

Figure G-18. Surface Profile Measurements of Fatigue Specimen #7, Location C, After Enthone Ni-426 Plating Treatments.
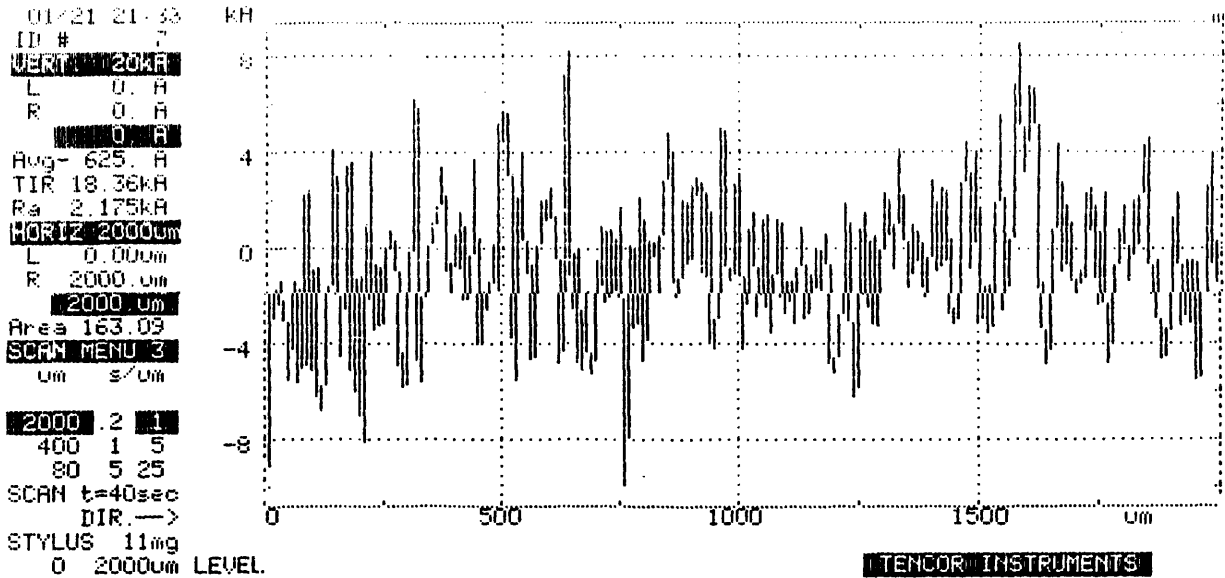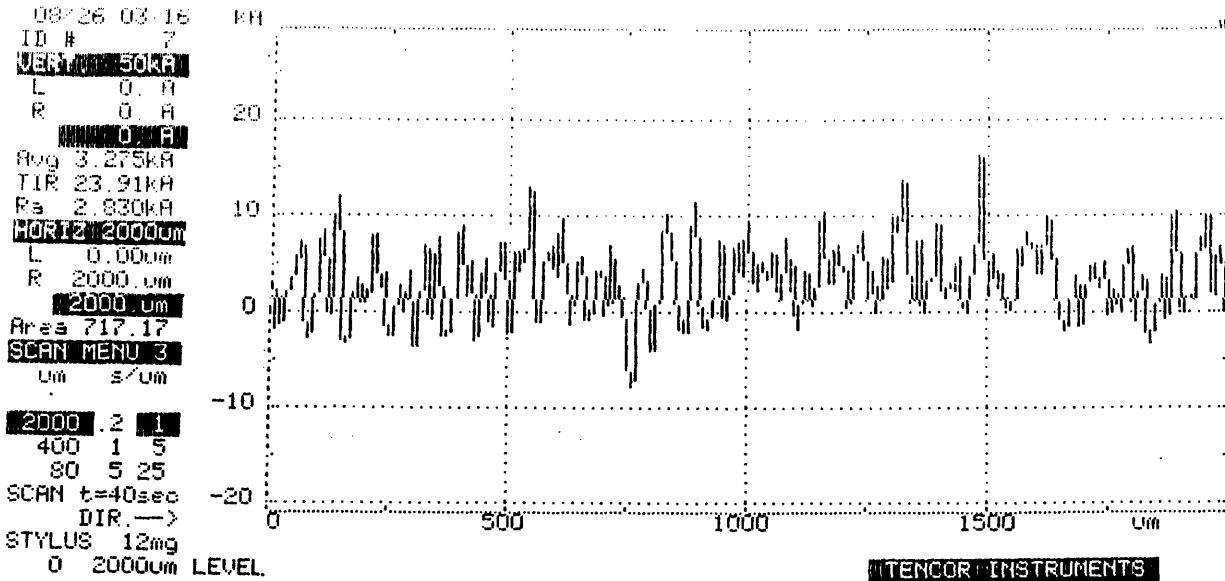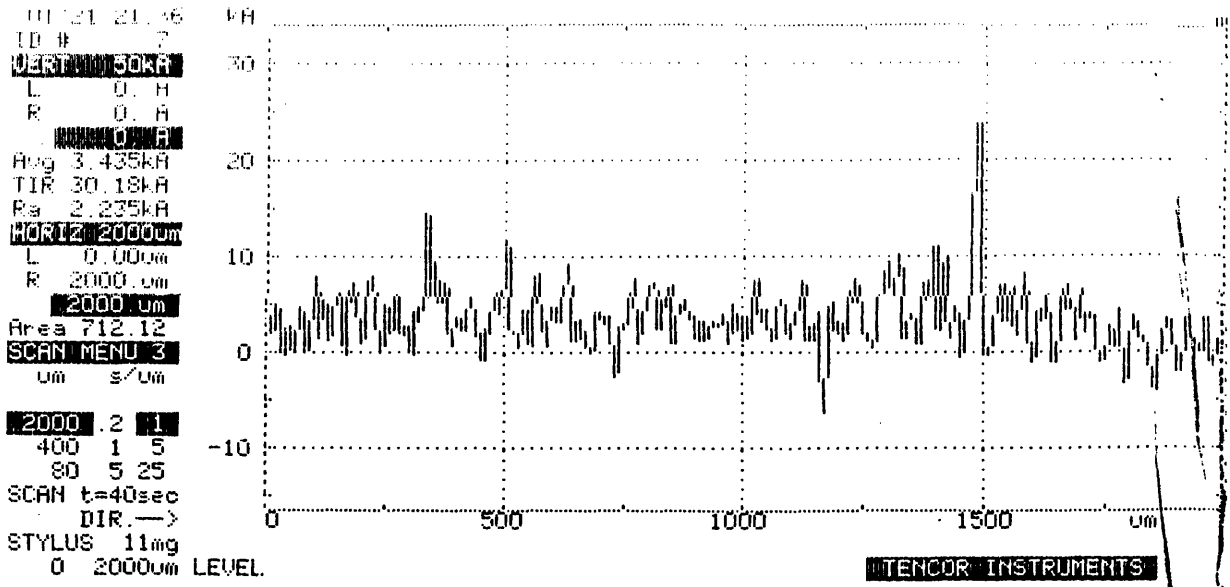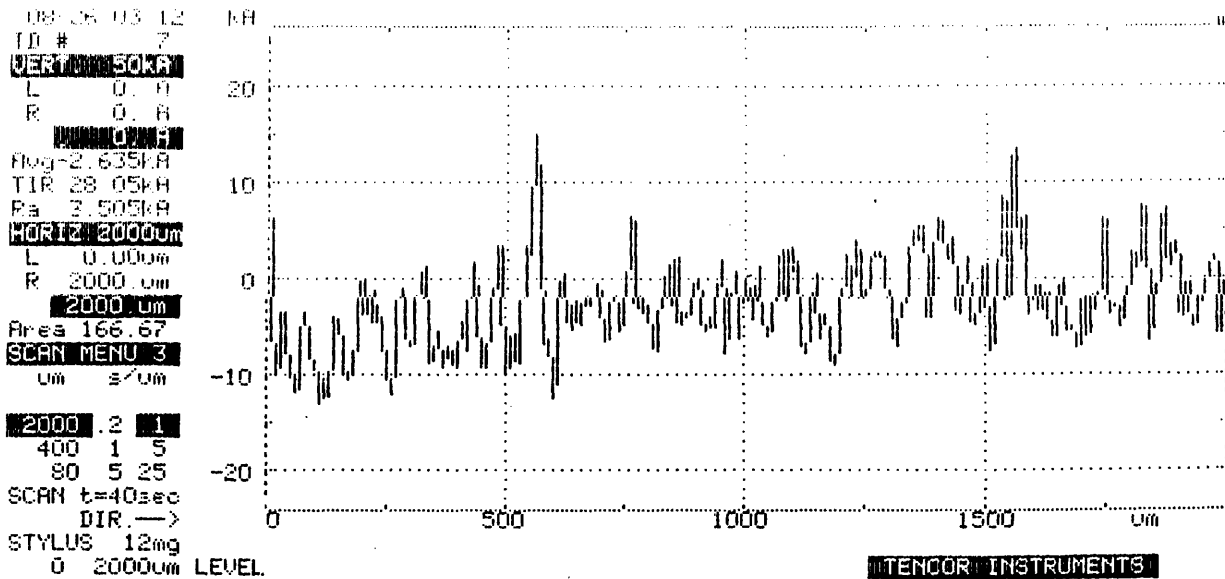
Figure G-19. Surface Profile Measurements of Fatigue Specimen #8, Location A, **Before** Enthone Ni-422 Plating Treatments.

Figure G-20. Surface Profile Measurements of Fatigue Specimen #8, Location A, **After** Enthone Ni-422 Plating Treatments.
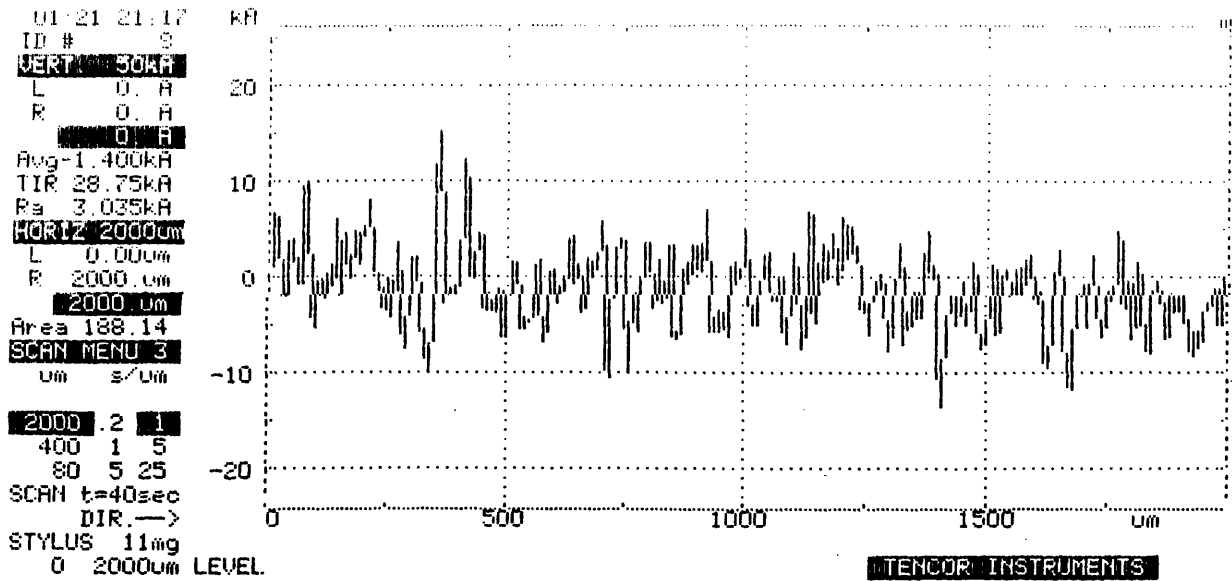
Figure G-21. Surface Profile Measurements of Fatigue Specimen #8, Location B, **Before** Enthone Ni-422 Plating Treatments.

Figure G-22. Surface Profile Measurements of Fatigue Specimen #8, Location B, **After** Enthone Ni-422 Plating Treatments.

Figure G-23. Surface Profile Measurements of Fatigue Specimen #8, Location C, **Before** Enthone Ni-422 Plating Treatments.
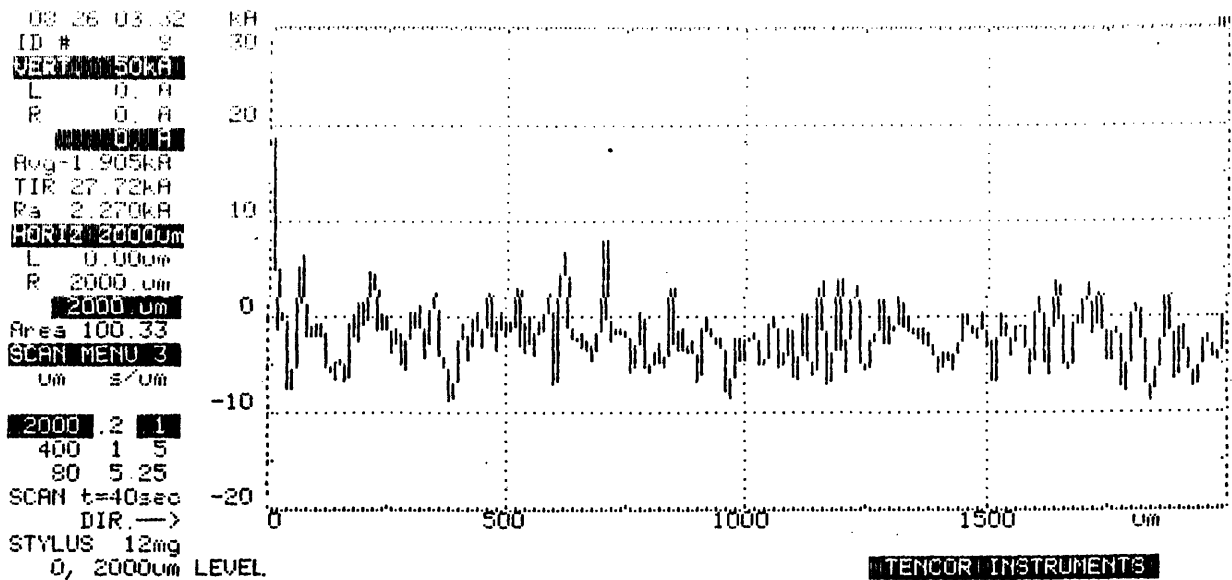

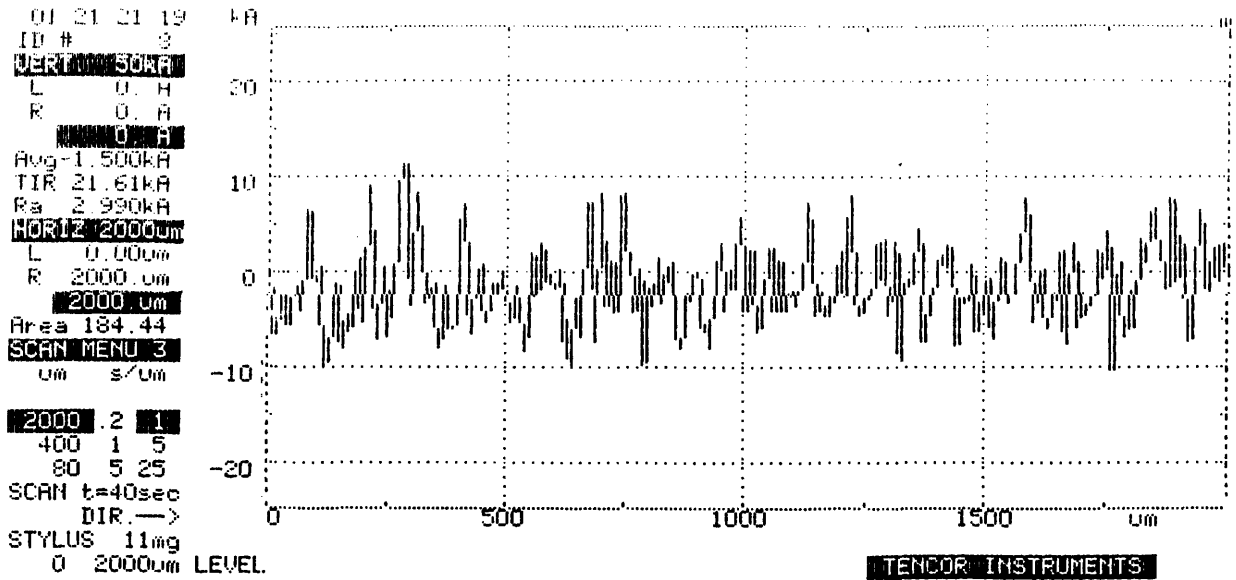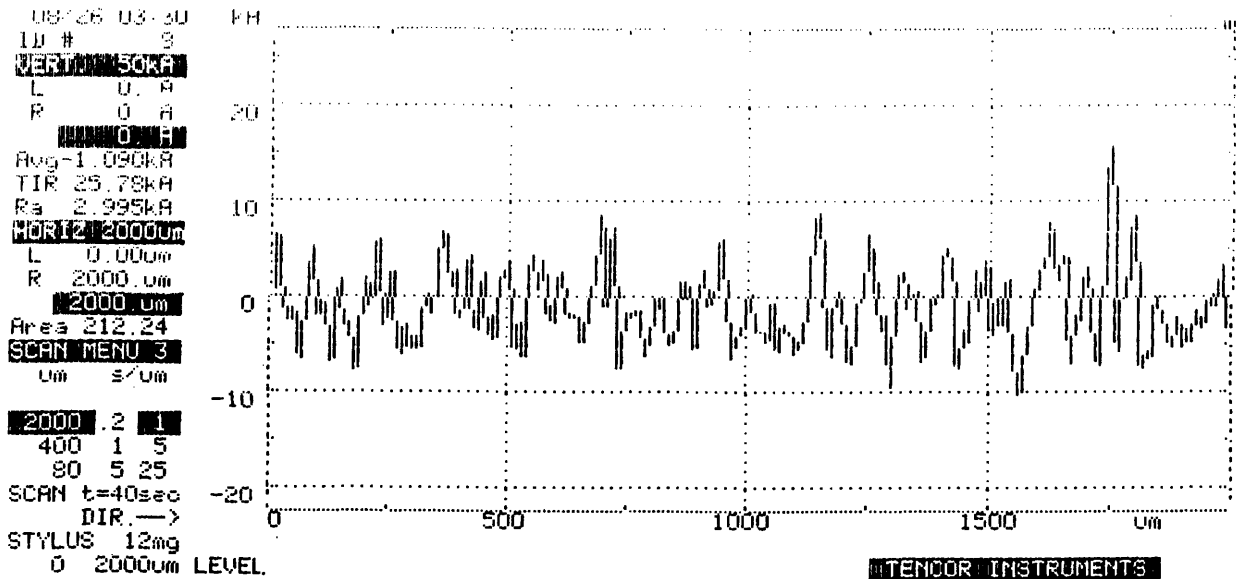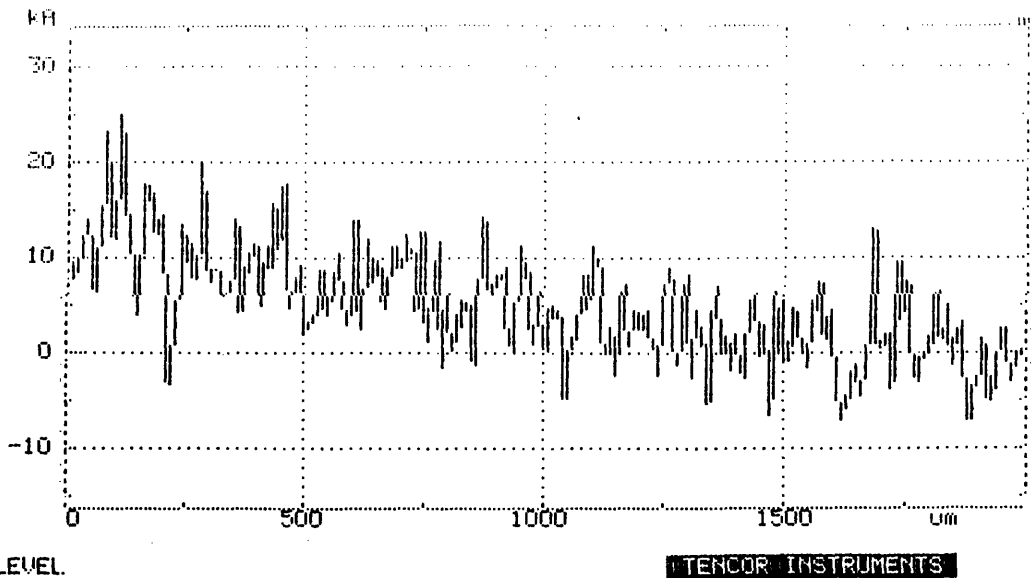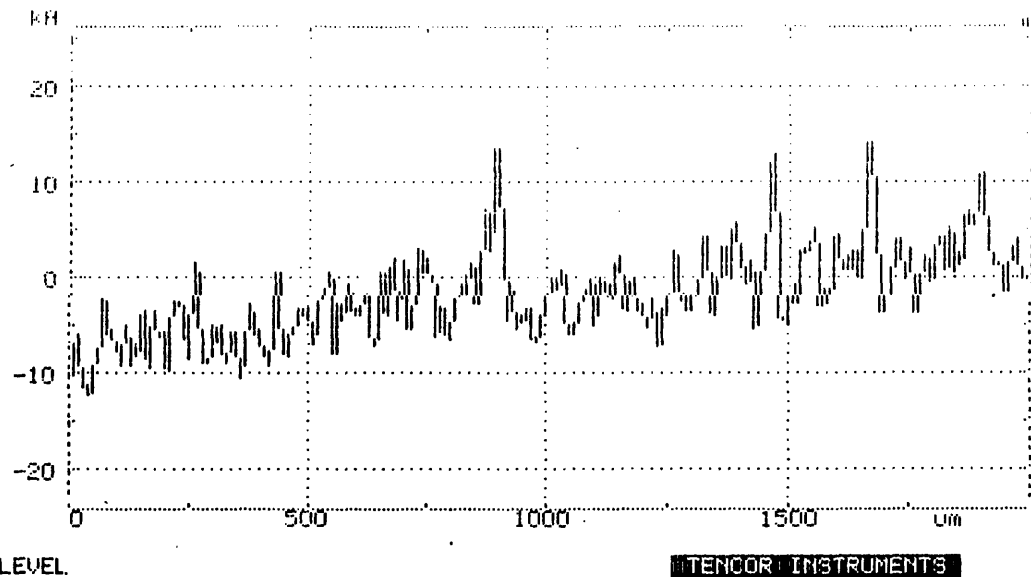**Figure G-24.** Surface Profile Measurements of Fatigue Specimen #8, Location C, **After** Enthone Ni-422 Plating Treatments.

REFERENCES

[1] *HH-65A Flight Manual*, United States Coast Guard Technical Order 1H-65A-1, p. 1-3.

[2] Idem., p. 1-4.

[3] Idem., p. 1-5.

[4] Kerrebrock, J.L. Structure of Engine Turbomachinery. In, *Aircraft Engines and Gas Turbines*, MIT Press, Cambridge, Mass., 1987, pp. 189-195.

[5] Kerrebrock, J.L., *Aircraft Engines*, p.192.

[6] *Alloy Data, Custom 450® Stainless Steel*, promotional publication from Carpenter Technology Corporation, Carpenter Steel Division, Reading, PA, p.24.

[7] Idem., p. 27.

[8] Idem., p. 27.

[9] LeGrange, J., Electroless Nickel Application at a Jet Engine Overhaul Plating Facility, *Electroless Nickel Conference*, (1982), 2-4.

[10] Reinhardt, G., Electroless Nickel Applications in Aircraft Maintenance, *Electroless Nickel Conference*, 820609, 27-28.

[11] Strafford, K.N., Data, P.K. and O'Donnell, A.K., Electroless Nickel Coatings: Their Application, Evaluation & Production Techniques, *Materials & Design, vol. 3*, (1982), 611.

[12] Fields, W.D., R.N. Duncan, J.R. Zickgraf and ASM Committee on Electroless Nickel Plating. Electroless Nickel Plating. In W.G. Wood (Ed.), *Metals Handbook*, American Society for Metals, Metals Park, Ohio, 1982, vol. 5, p.219.

[13] Gawrilov, G.G., *Chemical (Electroless) Nickel Plating*, Redhill, England, Portcullis Press, (1979).

[14] Fields, W.D., *Metals Handbook*, vol. 5, p.220.

[15] Fields, W.D., p.220.

[16] Mallory, G.O., The Electroless Nickel Plating Bath, *Electroless Nickel Conference*, (1982), 1.

[17] Mallory, G.O., *Electroless Nickel Conference*, 4-5.

[18] Fields, p.220.

[19] Mallory, G.O., 4-5.

[20] Mallory, 5.

[21] Mallory, 12.

[22] Mallory, 13.

[23] Fields, p.220.

[24] Mallory, 13.

[25] Bunshah, R.F., et al., Deposition from Aqueous Solutions: An Overview. In *Deposition Technologies for Films and Coatings*, Noyes Publications, Park Ridge, NJ, 1982, p.413.

[26] Metzger, Jr., W.H.. Characteristics of Deposits. In ASTM Special Technical Publication No.265, *Symposium on Electroless Nickel Plating*, American Society for Testing Materials, Philadelphia, PA, 1959, p.13.

[27] Pai, S.T. and J.P. Marton. *Journal of the Electrochemical Society, 120* (1973), 1280.

[28] Fields, p.223.

[29] Fields, p.226.

[30] Graham, A.H., R.W. Lindsay and H.J.Read. The Structure and Mechanical Properties of Electroless Nickel. *Journal of the Electrochemical Society, 112-4* (1965), 401.

[31] Fields, p.227.

[32] Baldwin, C. and T.E. Such. The Plating Rates and Physical Properties of Electroless Nickel/Phosphorus Alloy Deposits. *Transactions of the Institute of Metal Finishing, 46-2* (1968), 73.

[33] Gutzeit, G. and E.T. Mapp. Kanigen® Chemical Nickel Plating. *Corrosion Technology, 3-10* (1956), 331.

[34] Fields, p.226.

[35] Randin, J.P. and H.E. Hintermann. Electroless Nickel Deposited at Controlled pH; Mechanical Properties as a Function of Phosphorus Content. *Plating, 54-5-(1967)*, 523.

[36] Gawrilov, G.G., *Chemical (Electroless) Nickel Plating.*

[37] Duncan, R.N. Properties and Applications of Electroless Nickel Deposits. *Finisher's Management, 26-3* (1981), 5.

[38] Duncan, R.N. *Finisher's Management,* 5.

[39] Nemoto, K., et al. The Study on Hardness of Non-Electrolytically Plated Ni-P Deposits at High Temperatures and Effects Given by Heat Treatments. *Journal of the Metal Finishing Society of Japan, 16-3,* 106.

[40] Domnikov, L. Chromium and Electroless Nickel Deposits, Hardness at High Temperatures. *Metal Finishing, 60-1* (1962), 67.

[41] Parker, K. Hardness and Wear Resistance Tests of Electroless Nickel Deposits. *Plating, 61-9* (1974), 834.

[42] *Industrial Nickel Plating and Coating,* International Nickel Company, New York, 1976.

[43] Klein, H.G., et al. *Metalloberfläche Angewandte Elektrochemie, 25-9* (1971), *26-1* (1972).

[44] Klein, H.G., *Metalloberfläche, 25-9* (1971), *26-1* (1972).

[45] *Industrial Nickel Plating and Coating,* 1976.

[46] Parker, K. *Plating, 61-9,* 834.

[47] Stallman, K. and H. Speckhardt. Deposition and Properties of Nickel-Boron Coatings. *Metalloberfläche Angewandte Elektrochemie, 35-10* (1981), 979.

[48] Randin, J.P. *Plating, 54-5-(1967)*, 523.

[49] Justice, B. Electroless Nickel for Wear Resistance. *Products Finishing, Jan.* (1984), 56.

[50] Gawrilov, G.G.

[51] Parker, K., 834.

[52] Randin, J.P., 523.

[53] Duncan, R.N. Performance of Electroless Nickel Coatings in Oil Field Environments. *Corrosion, 82 Conference, National Association of Corrosion Engineers, Houston* (1982).

[54] Jarrett, G.D.R. Electroless Nickel Plating. *Industrial Finishing (London), 18-218* (1966), 41.

[55] Parker, K. Effects of Heat Treatment on the Properties of Electroless Nickel Deposits. *Plating and Surface Finishing, 68-12* (1981), 75.

[56] Dieter, G.E. Fatigue of Metals. In B.J. Clark (Ed.), *Mechanical Metallurgy,* McGraw-Hill, New York, 1961, p. 403.

[57] Priemon, R.A. (Ed.). Standard Definition of Terms Relating to Fatigue Testing and the Statistical Analysis of Fatigue Data. ASTM Designation E206-72. In, *1984 Annual Book of ASTM Standards,* ASTM, Philadelphia, PA, 1984, vol. 03.01, p. 341.

[58] Fuchs, H.O. and R.I. Stephens. Macro/Micro Aspects of Fatigue of Metals. In, *Metal Fatigue In Engineering,* John Wiley & Sons, New York, 1980, p. 14.

[59] Dieter, G.E. *Mechanical Metallurgy,* p. 404.

[60] Wood, W.A. Recent Observations on Fatigue Fracture in Metals. In, *ASTM STP 237,* American Society for Testing and Materials, Philadelphia, PA, 1958, pp.110-121.

[61] Broek, D. Mechanisms of Fracture and Crack Growth. In, *Elementary Engineering Fracture Mechanics,* Martinus Nijhoff, Dordrecht, The Netherlands, 1986, p. 59.

[62] Dieter, G.E., p. 414.

[63] Meyers, M.A. and K.K. Chawla. Fracture and Fracture Toughness. In B. Kurtz (Ed.), Mechanical Metallurgy, Prentice-Hall, Englewood Cliffs, NJ, 1984, pp. 141-142, p. 708.

[64] Broek, D. *lEementary Engineering Fracture Mechanics,* pp.61-62.

[65] Pelloux, R.M.N. Mechanisms of Formation of Ductile Striations. *ASM Transactions, 62* (1969), 281-285.

[66] Broek, D., p. 60.

[67] Broek, D., pp. 59-62.

[68] Dieter, G.E., p.418.

[69] Broek, D., p. 61.

[70] Meyn, D.A. The Nature of Fatigue-Crack Propagation in Air and Vacuum for 2024 Aluminum. *ASM Transactions Quarterly, 61-1* (1968), 52-61.

[71] Pelloux, R.M.N. *ASM Transactions*, 281-285.

[72] McClintock, F.A. and R.M.N. Pelloux. Technical Report D1-82-0708, Boeing Scientific Research Laboratories, 1968.

[73] Pelloux, R.M.N., 281-285.

[74] Pelloux, 281-285.

[75] Fuchs, H.O. and R.I. Stephens. *The Fatigue of Engineering Materials*, John Wiley & Sons, 1980.

[76] Colangelo, V.J. and F.A. Heiser. *Analysis of Metallurgical Failures*, John Wiley & Sons, 1987.

[77] Dieter, G.E., pp. 404-406.

[78] Dieter, p. 407.

[79] Fuchs, H.O. and R.I. Stephens. Constant Amplitude Fatigue Tests and Data. In, *Metal Fatigue In Engineering*, John Wiley & Sons, New York, 1980, p. 64.

[80] Fuchs, H.O. and R.I. Stephens. *Metal Fatigue In Engineering*, pp. 95-96.

[81] Sinclair, G.M. and T.J. Dolan. Effect of stress Amplitude on Statistical Variability in Fatigue Life of 75S-T6 Aluminum Alloy. *Transactions of the ASME, 75* (1953), 867.

[82] Dieter, p. 427.

[83] Siebel, E. and M Gaier. *Engineer's Digest, 18* (1957), 109-112.

[84] Dieter, pp. 428-430.

[85] Duncan, R.N.

[86] Fields, p.224.

[87] Storer, R.A. (Ed.). Standard Method for Measurement of Internal Stress of Plated Metallic Coatings with the Spiral Contractometer. ASTM Designation B 636-84. In, *1988 Annual Book of ASTM Standards*, ASTM, Philadelphia, PA, 1984, vol. 02.05, p. 415-417.

[88] Walker, G.A. and C.C. Goldsmith. A Structural Comparison of Electroless and Electroplated Nickel. *Thin Solid Films, 53* (1978), 217-222.

[89] Parker, K. and H. Shah. Residual Stresses in Electroless Nickel Plating. Plating, 58-3 (1971), 230-236.

[90] Fields, p.224.

[91] Gawrilov, G.G.

[92] Duncan, R.N.

[93] Fields, p. 231.

[94] Gazez'yan, L.N. and E,N. Romanova. Chemical Nickel Plating on Steel Parts. *Aviatsionnaya Promyshlennost, 7* (1956), 44.

[95] Gorbunova, K.M. and A.A. Nikiforova. Properties of the Coating. In, *Physicochemical Principles of Nickel Plating*, Sivan Press, Jerusalem, Israel, 1963, p. 78.

[96] Antskaitis, V.A. Chemical Nickel Plating. *Filial Vsesoyuznogo Instituta Nauchnoi i Tekhnicheskoi Infomatsii AN SSSR, topic 13, no. M-58-368/39*, (1958).

[97] Gorbunova, K.M. and A.A. Nikiforova. *Physicochemical Principles of Nickel Plating*, p. 79.

[98] Borisov, V.S. and S.A. Vishenkov. Chemical Nickel Plating. *Moskovskii dom nauchno-teckhnicheskoi propagandy im. F.E. Dzerzhinskogo, 2* (1958), 37.

[99] Gorbunova, K.M. and A.A. Nikiforova. *Physicochemical Principles of Nickel Plating,* p. 79.

[100] Gorbunova, K.M. and A.A. Nikiforova. p. 80.

[101] Fields, p. 231.

[102] Slagle, W.P. *Effect of an Electroless Nickel Plating on the Fatigue Strength of Steel. Final Report for MEN 414, April 28, 1977,* Department of Mechanical Engineering, University of Miami, Miami, Florida.

[103] Reinhardt, G. Potential Applications of Electroless Nickel in Airline Maintenance Operations. *Electroless Nickel Conference, 580683,* 5.

[104] Izumi, H., H. Sunada and Y. Kondo. The Fatigue Strength of Electroless Nickel Plating Steel. *The 18th Japan Congress on Materials Research - Metallic Materials,* (1975), 47-51.

[105] Kondo, Y., H Sunada and H. Izumi. Effect of Electroless Nickel Plating on the Fatigue Strength of Notched Steel. *The 21st Japan Congress on Materials Research - Metallic Materials,* (1978), 80-83.

[106] Parker, K. *Plating and Surface Finishing, 68-12* (1981), 76.

[107] *Alloy Data, Custom 450® Stainless Steel,* promotional publication from Carpenter Technology Corporation, Carpenter Steel Division, Reading, PA, p. 28.

[108] Private communication between LCDR Evans from the Aircraft Repair and Supply Center, Elizabeth City, NC and LT Napert (author).

[109] Surface Preparation for Strain Gage Bonding. *Micro-Measurements Division M-Line Accessories Instruction Bulletin B-129-5,* Measurements Group, Inc., Raleigh, NC,1976, pp. 1-8.

[110] Strain Gage Installations with M-Bond 200 Adhesive. *Micro-Measurements Division M-Line Accessories Instruction Bulletin B-127-9,* Measurements Group, Inc., Raleigh, NC, 1979, pp. 1-4.

[111] Plate, Sheet, and Column Testing Machines. *Krouse Testing Machine Inc. Bulletin 53B,* Krouse Testing Machine Inc., Columbus, Ohio, (undated).

[112] Vander Voort, G.F. Quantitative Microscopy. In A. Murphy (Ed.), *METALLOGRAPHY Principles and Practice,* McGraw-Hill, Taipei, Taiwan, 1984, pp. 447-451.

[113] *Alloy Data, Custom 450® Stainless Steel,* promotional publication from Carpenter Technology Corporation, Carpenter Steel Division, Reading, PA, pp. 27-30.

[114] *Alloy Data, Custom 450® Stainless Steel,* p. 31.

[115] *TENCOR INSTRUMENTS ALPHA-STEP 200 User's Manual.* TENCOR INSTRUMENTS (undated), p. 35.

9.   Biographical Note

The author was born on January 23, 1956 in the small New England town of Berlin, New Hampshire. His family, including an older brother and two younger sisters, moved to Portsmouth, New Hampshire during his early childhood and then to North Stonington, Connecticut at the age of nine. He graduated with high honors from Wheeler High School in North Stonington, CT. His high school years were spent studying for personal achievement, playing baseball and running cross-country, and working for a college education. Gary began dating his future wife, Deborah Purcell of North Stonington, CT during their sophomore year. In his senior year of high school, he applied and received appointments to both the United States Coast Guard Academy and the United States Air Force Academy.

Immediately after High School, he reported to the U.S. Coast Guard Academy, New London, CT to pursue a career as a U.S. Coast Guard Officer, with high hopes of becoming a naval aviator. On May 24, 1978, he graduated with high honors receiving a B.S in Mathematical Sciences and a commission as an Ensign in the United States Coast Guard. Gary and Deborah were married three days later! His first assignment was as a Deck Watch Officer aboard the USCGC Vigorous stationed at the USCG Academy.

Aboard Vigorous during the period July 1978 to July 1979, he served as the Combat Information Center Officer, Weapons Officer, Commissary Officer, Public Affairs Officer and Ship's Exchange Officer. He also received the qualifications of Officer of the Deck (OOD), Landing Signal Officer (LSO) and Boarding Officer. Gary was selected for Naval Flight Training in the Spring of 1979.

Gary and Deborah left the familiar surroundings of southeastern Connecticut together, for the first time. Deborah was forced to abandon her successful career as an Assistant Bank Manager, but looked forward to the adventure of traveling to Pensacola, Florida. Gary received his WINGS on August 1, 1980, after completing the multi-engine aircraft training program in Corpus Christi, Texas. Their first son, Gary Joseph, was born on July 11, 1980. Gary received orders for a C-130 flight duty assignment at U.S. Coast Guard Air Station Elizabeth City, North Carolina. The assignment required two months of initial copilot training in the C-130 transport airplane at Little Rock AFB, Arkansas. On the move again, Gary moved his family to Elizabeth City, NC, where they lived for four years. Shortly after reporting to Air Station Elizabeth City, Gary became interested in the USCG Aeronautical Engineering Program and requested the duties of the Aviation Material Officer (AMO). Their second son, Brian William, was born on September 15, 1983. In 1984, Gary completed the USCG Maintenance Officer Training Program and upgraded his C-130 qualification to Aircraft Commander. Then, he received transfer orders for the assignment of Assistant Engineering Officer (AEO) Barbers Point, Hawaii.

Gary spent a very rewarding tour of duty in Hawaii. He flew many Search and Rescue, logistics, and law enforcement missions to accumulate more than 2400 flight hours. Along with his Pilot duties, his AEO responsibilities included the management of 110 engineering personnel in support of three C-130 airplanes and three H-52 helicopters. Gary was selected for the USCG Postgraduate School Program and applied to M.I.T. and Purdue for admission. He was accepted by both schools and decide to attend M.I.T.. In 1987, the Napert family moved to Wilmington, MA.

At M.I.T., Gary took several undergraduate courses in mechanical engineering, aeronautics and astronautics, and materials science to develop a sound background for graduate studies. The family sacrifice and demands during the two years at M.I.T. were, at times, overwhelming. His perseverance was rewarded. Gary received a M.S. in Aeronautics and Astronautics in September 1989. Gary, now LT Napert, received transfer orders for an assignment as an Aeronautical Engineer at the USCG Aircraft Repair and Supply Center, Elizabeth City, NC.